Abstract of thesis entitled

"Cluster structure of neutron-rich Beryllium isotopes investigated via $(p, p\alpha)$ reaction in inverse kinematics at 150 MeV/u"

Submitted by

Pengjie Li

for the degree of Doctor of Philosophy
at The University of Hong Kong
in Feburary 2021

Alpha clustering structure in nuclei, which is beyond the description of modern shell models, challenges the understanding of fundamental interactions and reveals new aspects of nuclear forces. The ^{8}Be ($N = 4$, $Z = 4$) nucleus is famous for its developed α-α structure. Neutron-rich Beryllium isotopes ^{10,12,14}Be predicted as di-cluster structure with valence neutrons surrounding α-α core are the very appealing candidates of clustering studies.

We aim at directly and quantitatively probing the cluster structure in the ground state of ^{10,12,14}Be isotopes via quasifree $(p, p\alpha)$ reaction in inverse kinematics. The experiment was performed at RIKEN with the world's highest intensity of neutron-rich ^{10,12,14}Be beams at 150 MeV/u. The reactions of interest were induced by beams of exotic Be isotopes impinging on a pure solid hydrogen target. The SAMURAI spectrometer was employed to achieve large acceptance and high resolution characteristics. Combined with charge-particle detection systems surrounding the target, exclusive measurements were achieved for the physics goals.

The triple differential cross-sections (TDX) for the $(p, p\alpha)$ reactions are extracted at quasifree angle pairs (θ_p,θ_α) and compared to the distorted-wave impulse approximation (DWIA) reaction calculation with Tohsaki-Horiuchi-Schuck-Röpke (THSR) structure model. The extracted TDXs in ^{10}Be$(p, p\alpha)^{6}$He(g.s.) and ^{12}Be$(p, p\alpha)^{8}$He(g.s.) reactions are very close to each other. For the former reaction, both the shape and the magnitude of the TDX are very well reproduced by the DWIA calculation. This result clearly validates the molecular cluster structure $2\alpha + 2n(\pi)$ in the ground state of ^{10}Be nucleus described by the THSR wave-function. For the later reaction, the shape of the experimental result is in moderate agreement with

the DWIA calculation, while the magnitude of the experimental results is greatly overestimated, suggesting a more compact structure in the ground state of ^{12}Be. Further improvement in the cluster wave function is needed.

The populations of the ground state in He residues are comparable between ^{10}Be$(p, p\alpha)$ and ^{12}Be$(p, p\alpha)$ while the populations of the excited states are radically different. The excited-state transition is as important as the ground-state transition for the former, whereas the ground-state transition strongly dominates over the other excited-state transitions for the latter. Cross-sections for the population of 2^+ excited state in He residues have been extracted and compared to the result of the ground-state transition. The ratio of the 2^+ state transition to the ground-state transition for ^{10}Be$(p, p\alpha)$ reaction is nearly a half at proton scattering angle 65°; while the ratio for ^{12}Be$(p, p\alpha)$ reaction is less than 1%. Such a significant difference of 2^+ state component in He-core excited states unambiguously indicates completely different cluster structures in the ground state of ^{10}Be and ^{12}Be.

(413 words)

Cluster structure of neutron-rich Beryllium isotopes investigated via $(p, p\alpha)$ reaction in inverse kinematics at 150 MeV/u

by

Pengjie Li

B.Sc. *UESTC*; M.A. *PKU*

A thesis submitted in full fulfilment of the requirements for
the Degree of Doctor of Philosophy
at The University of Hong Kong.

Feburary 2021

To my loved ones.

Declaration

I declare that this thesis represents my own work, except where due acknowledgement is made, and that it has not been previously included in a thesis, dissertation or report submitted to this University or to any other institution for a degree, diploma or other qualifications.

Signed . . . . . .

Pengjie Li

Acknowledgements

The research work in this thesis is conducted in the Experimental Nuclear Physics Group at the Department of Physics, The University of Hong Kong. I would like to express my sincere gratitudes to many people.

I would like to thank my supervisor, Dr. Jenny Hiu Ching Lee for giving me the opportunity to conduct research in the field of nuclear physics. Thank her for the encouragement and continuous support during my Ph.D study. I learned a lot from her, such as how to to handle data analysis for experiments; how to organize presentation in seminars or workshops; how to prepare an academic CV and plan a research career. I believe that I will continue to benefit from valuable experience she shared with me in my future career.

I want to thank my co-supervisor Dr. Didier Beaumel from IJC lab in France. Many thanks to him for providing patient guidance and sharing his knowledge in experimental and theoretical physics. I'm thankful for his guidance and invaluable help in every way, and for his brilliant ideas and encouragement he gives during the data analysis. This thesis would not have been possible without millions of fruitful discussions with him.

Special thanks goes to Prof. Kazuyuki Ogata for the generous support of the theoretical calculations. The discussions with him taught me a lot of theoretical knowledge and gave me a deeper understand of reaction model. I would like to thank both Dr. Serge Franchoo and Dr. Sidong Chen for their tremendous help in data analysis. They helped me to get familar with the experimental setup and provided very useful analysis code that saved me countless hours.

I also want to send my gratitudes to Dr. Xu Xinxing for sharing millions of experience of the on-site work, testing the GET electronics. My sincere thanks also goes to Dr. Sylvain Leblond for his instruction of data analysis and continuous help during my research. I would like to thank Prof. Li Zhihuan of Peking University, who is my master's supervisor. I cannot forget that he granted any request for help. I also want to send my gratitudes to all the other members of Nuclear Physics Group, Dr. Jiajian Liu, Dr. Lokotko Taras, Dr. Pengfei Liang, Mr. Wenduo Xian. Thank

you all very much for the help and encouragement in my study and daily life. I am honored to work with these excellent researchers in the same office.

I would like to express my gratitudes to the SAMURAI12 collaborators from different institutes. I don't have enough space to individually describe the connection with them, but I want their names to be written down to record the irreplaceable help they have provided: Achouri, L. (LPC Caen); Assié, M. (IJClab); Baba, H. (RIKEN); Cardella, G. (INFN); Ceruti, S. (INFN Milano); Chilug, A. (NIPNE); Corsi, A. (CEA Saclay); Frotscher, A.(TU Darmstadt); Gibelin, J. (LPC Caen); Gillibert, A. (CEA Saclay); Hammache, F. (IJClab); Harada, T. (RIKEN); Inaba, K. (Kyoto U); Isobe, T. (RIKEN); Kawabata, T. (Osaka U.); Kitamura, N. (RIKEN); Kobayashi, T. (Tohoku Univ); Kondo, Y. (Titech); Kubota, Y. (RIKEN); Kurihara, A. (Titech); Liu, H.N. (TU Darmstadt); Marqués, M. (LPC Caen); Matsuda , Y. (Tohoku Univ); Miki, H. (Titech); Otsu, H. (RIKEN); Obertelli, A. (TU Darmstadt); Orr, N. (Lpc-Caen / In2p3-Cnrs); Panin,V. (Cea Saclay); Rindel, E. (IJClab); Sakaguchi, S. (Kyushu University); Sasano, M. (RIKEN); Shimada , T. (Titech); Stuhl, L. (Center For Nuclear Study, University Of Tokyo); Sun, Y.L. (TU Darmstadt); Suzuki, D. (RIKEN); Tanaka, J. (TU Darmstadt); Togano, Y. (Rikkyo University); Tomai, T. (Titech); Trache, L. (NIPNE); TUdor, D. (NIPNE); Uesaka, T. (RIKEN); Wang, H. (RIKEN); Yang, Z.H. (Rcnp Osaka Univ); Yamada, H. (Titech); Yasuda, M. (Titech); Zenihiro, J. (RIKEN).

Last but not least, I would like to thank my father, mother, and future wife Dr. Xiaohui Sun for their constant love, infinite support and encouragement. It is your priceless love that drives me through the long journey of pursuing my Ph.D degree. I will continue to be the best version of myself and love you even more.

Contents

List of Figures

List of Tables

Chapter 1

Introduction

This thesis presents an analysis of data taken by the SAMURAI12 collaboration at the Radioactive Isotope Beam Factory (RIBF) in RIKEN Nishina Center, in 2018. The analysis focuses on the study of alpha clustering in the ground state of neutron-rich Be isotopes via alpha particle knockout reactions at beam energy of 150 MeV/u in inverse kinematics. This chapter gives an introduction to the present study.

1.1 Clustering

The nucleus composed of proton and neutrons is a complex N-body quantum system, mainly governed by 3 basic forces: strong, weak, and electromagnetic forces. Protons and neutrons are also called nucleons viewed as two nucleonic states. Given the complexity of N-body interactions in the nuclear system, even with very few nucleons in the nucleus, many phenomena still lack a theoretical explanation. On the other hand, the study of clustering that protons and neutrons tend to form small groups inside nucleus turns the N-body problem into a two-body problem.

The hypothesis about the existence of clusters such as alpha-particles in a nucleus has been brought up since the earliest days of nuclear physics. However, the studies of alpha cluster model were suppressed due to the popularity of the shell model. In the 1950s, some experimental results [1] show that a large overabundance of alphas emitted from the target nuclei in proton-induced reactions with incident energies from 40-600 MeV was consistently found in the forward direction, indicating there may exist direct collisions between incident proton and alpha clusters inside nucleus. However, the shell model failed to predict the coexistence of clusters in nuclei with strong independent-particle properties in the early stage.

α clustering has dominated in the subject of cluster structure studies for the past few decades, due to the large binding energy and stability of alpha particle. Figure 1 shows the binding energy per nucleon of light nuclei and the excitation energy of the first excited state versus binding energy for nuclei up to $A = 20$; The alpha-conjugate

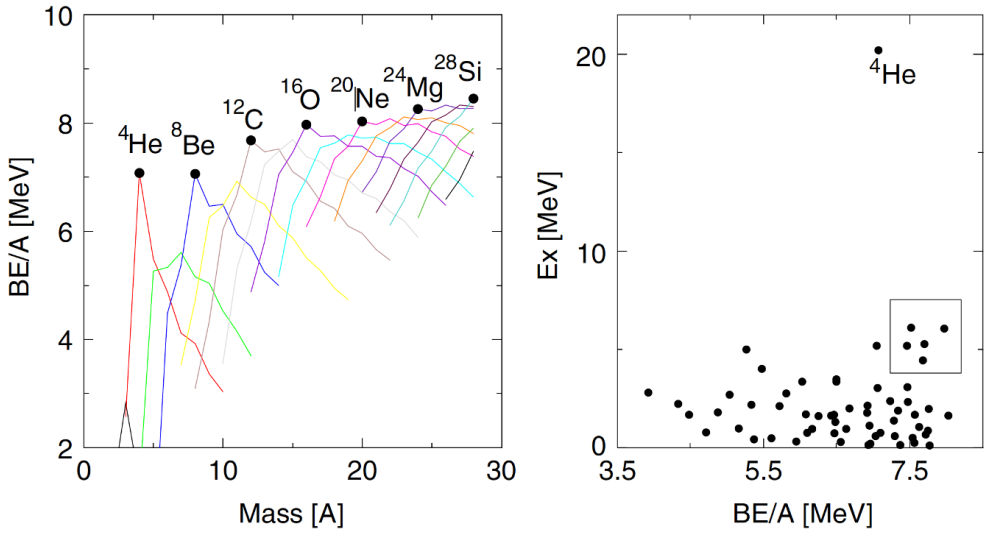

Figure 1 (Left) Binding energy per nucleon versus mass number A of light nuclei; (Right) Excitation energy of first excited states versus binding energy per nucleon for nuclei up to $A = 20$ [2].

nuclei are addressed by filled circles. The color lines indicate the isotope chain of each element. The binding energy of alpha particles is over 7 MeV/nucleon which is the highest compared with other nuclei. In addition, the energy of first excitation state is also extraordinarily high, indicating its stability. These features make α-conjugate nuclei energetically favorable for forming cluster structures inside nucleus.

Hafstad and Teller [3] introduced an influential model for clustering in alpha-conjugate nuclei ($N = Z$ and $A = 4n$, $n = 2,3,4$ ...) with bonds connecting α clusters. The binding energy of $n-\alpha$ systems can be calculated from the number of bonds for alpha-particles in the crystalline structures. Figure 2 shows the various crystalline structures of alpha-conjugate nuclei. The binding energy of "nα systems" is proportional to the number of bonds calculated by drawing the crystal structures that α particles can occupy. The binding energy predicted by this model shows good agreement with experimental results, except for the unbound ^{8}Be, which was predicted to have a binding energy of approximately 2.5 MeV. The alpha model developed by Hafstad and Teller indicates clustering might appear in the ground state of such nuclei.

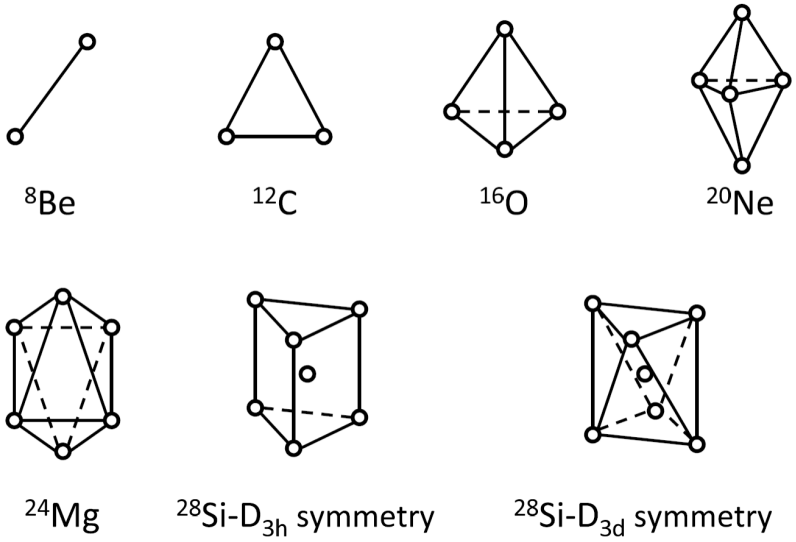

Figure 2 α-particle crystalline structures and possible bonds predicted in the model developed by Hafstad and Teller [3]

1.1.1 Molecular orbit model

The shell model failed to predict the appearance of α-cluster states in nuclei with strong independent-particle properties [2, 4]. Such states which can be described as several α-clusters and valence nucleons is similar to the covalent bonds in atomic systems, leading to the name “nuclear molecules" [5]. The valence nucleons can be seen as occupying molecular orbits in a multi-center system.

An attractive system for the cluster structure studies is the neutron-rich nuclei Be isotopes with two α cluster cores. The valence neutrons surrounding the two α cores can be occupy the molecule-like orbits, π and σ orbits, associated to the p and sd orbits in the shell model, respectively. Figure 3 shows a schematic figures of π-orbit (a) and σ-orbit (b) surrounding 2α clusters [6].

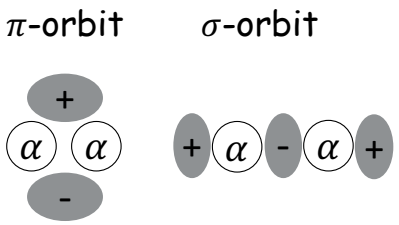

Figure 3 Schematic figures of the molecular orbits π-orbit (a) and σ-orbit (b) surrounding 2α clusters, adapted from [6].

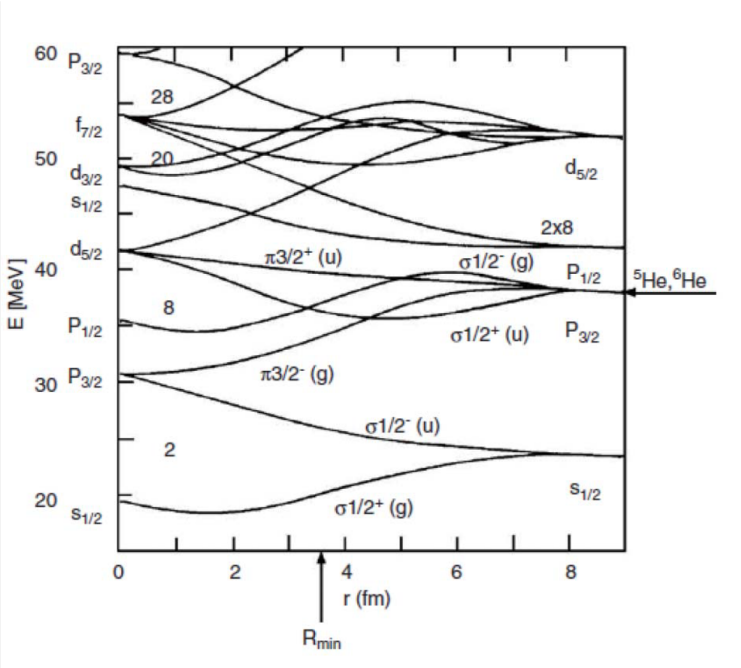

Figure 4 Single-particle energies of two-center shell model with 2α core [7]

Figure 4 gives the single nucleon energies as function of separation distance between two centers corresponding to the centers of identical core clusters. Filling the α-α core to the lowest two molecular orbits($\sigma_{1/2^+}$ and $\sigma_{1/2^-}$) from the $0s_{1/2}$ and $0p_{3/2}$ level forms the basic structure of neutron-rich Be isotopes, and the intrinsic structures are mostly obtained by putting excess neutrons into the following three molecular orbits: $\pi^-_{3/2}(g)$, $\sigma^-_{1/2}(g)$, $\sigma^+_{1/2}(u)$. The structures of intrinsic ground and excited states in Be isotopes can be well explained with particle-hole configurations of molecular orbit model. The ground state of nucleus ^{8}Be configured only with two α centers is unbound. The addition of a valence neutron in ^{9}Be mainly occupy the π-orbit, forming a bound nucleus [5].

1.1.2 Clustering in neutron-rich Nuclei

In 1968, Ikeda [8] found that α-clustering mainly occur close to α-decay thresholds in the alpha conjugate nuclei and these results were schematically organized with the so-called Ikeda diagrams, shown in Figure 5. The different columns in the x-axis represents cluster forms for a given isotope. As the excitation energy increases, the level of clustering in the nucleus becomes higher and higher. For example, a ^{28}Si nucleus tends to form a ^{24}Mg and an α-particle at the excitation energy below 9.78 MeV; The Ikeda diagram schematically illustrates that α particles tends to be a tightly

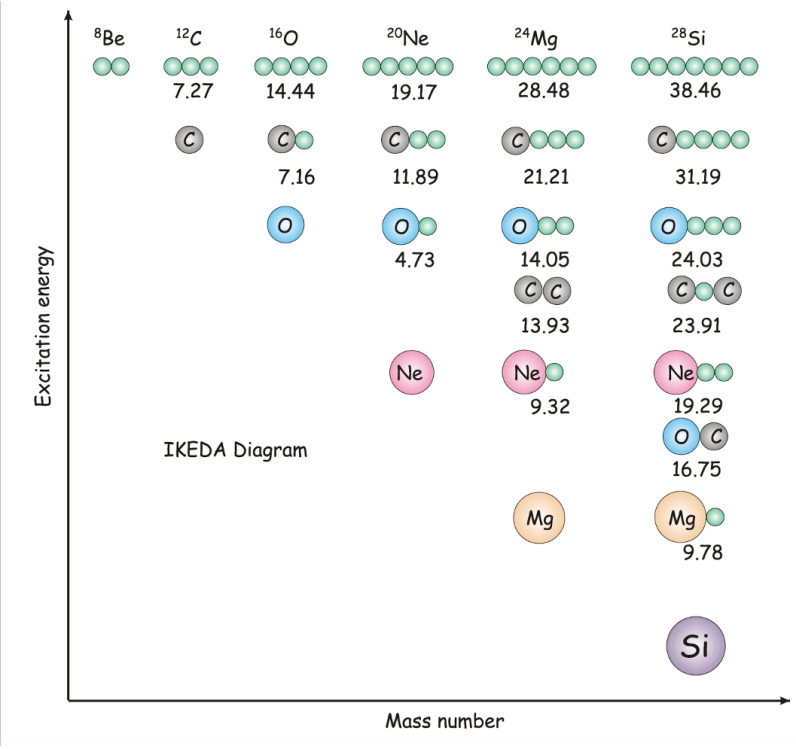

Figure 5 Ikeda diagram [8], figure from [2].

bound subunit of four nucleons in nuclear system. The prediction has been proven experimentally in the alpha conjugate nuclei.

Figure 6 gives a diagram of the cluster structure in the ground state of neutron-rich nuclei, compared to stable nuclei. The nuclear structure of stable nuclei in the ground state are quiet compact and it makes the alpha decay threshold relatively high to the ground state. According to the Ikeda diagram, the deformed cluster structure is expected to be in the excited state below the threshold. For the neutron-rich isotopes, the alpha decay thresholds are overall lowered due to the excess neutrons, as shown in Figure 6. It provide the opportunities to study the cluster structures even in the ground state of neutron-rich nuclei. Many theoretical calculations also support this idea.

Antisymmetrized molecular dynamics (AMD) calculation predicts that clustering may be an important structural mode for nuclei at the drip-line. Such model does not require assumptions about the pre-existence of clusters and their relative coordinate [5], thus having the ability to treat cluster and shell model type systems in a single framework. Figure 7 shows the calculated proton and neutron density distributions of Boron isotopes. The evolution from a spherical stable ^{11}B up to the dripline ^{19}B

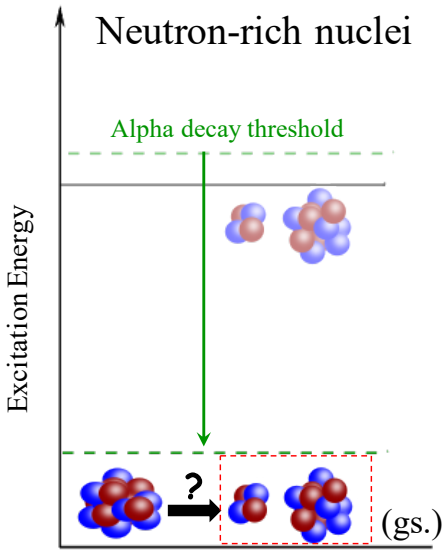

Figure 6 Diagram of the clustering in the ground state of neutron-rich nuclei

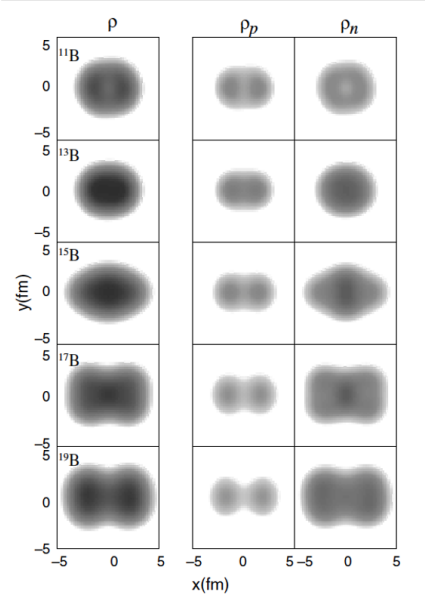

Figure 7 Density distributions of boron isotopes, $^{11-19}$B from [5].

raises question about the role of excess neutrons as enhancing factor of clustering is raised.

For nuclei far from the valley of stability, the weak binding of neutrons in neutron-rich nuclei lower the decay thresholds and gives rise to new nuclear phenomena [2]. Neutrons within the core occupied orbitals and thus the valence neutrons must occupy higher energy orbits which are energetically unfavoured [4]. However, the binding energies may be enhanced by forming clusters for maximising the surface area of the nucleus, which maximize the interaction overlap between valence neutrons and the protons residing within the cores. The development of radioactive ion beams made it possible to investigate the new type of cluster structure in the neutron-rich nuclei.

1.1.3 Clustering in Be isotopes

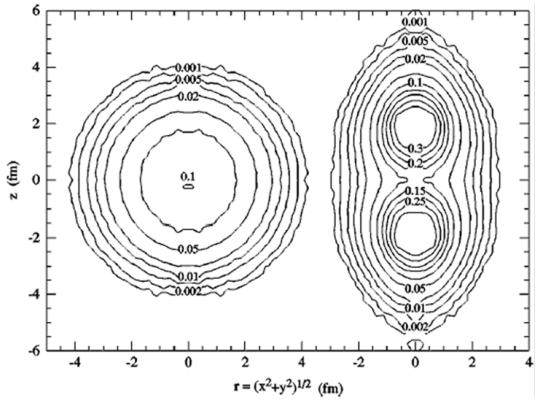

Figure 8 The ab initio calculation of the density of ^{8}Be(g.s.). The left and right images are the densities corresponding to the laboratory and intrinsic frames, respectively [9].

Beryllium isotopes as di-cluster structure with the valence neutrons surrounding α-α core are of special interest in relation with cluster studies. The ^{8}Be nucleus is famous for its developed α-α structure, well reproduced by ab initio variational Monte-Carlo calculations [9], shown in Figure 8. These calculations do not require assumptions about the pre-existence of clusters and predict the structure of nuclei based only on realistic nucleon-nucleon interactions. The ground state of ^{8}Be is clearly clustered with intercluster distance about 4 fm. ^{9}Be is the only stable Be nucleus with a dumbbell shape modeled by the additional neutron occupying $\pi_{3/2^-}$ orbit and forming a covalent bond between the two clusters, similar to an electron being shared between two protons in a covalent bond forming a H_2^+ ion [5]. In the case of ^{12}Be nuclei, the magic number $N = 8$ is broken due to the antisymmetry of

protons and neutrons. This can also be seen as a result of α cluster formation[10, 11, 12].

In recent years, microscopic theories have been successfully used to describe the clustering states ranging from the molecular-like states in ^{9,10}Be [13]. Physical observables, such as energies and radii, are well reproduced by theoretical calculations for the corresponding experimental values. These results are strong evidence for the α-clustering picture in these states. However, it is also to study physical observable related more directly to the cluster degrees of freedom.

It is possible to probe the nature of the cluster structure of these nuclei via reactions. In 2004, Ashwood and Freer's team [14, 15] performed a series measurements of the cluster breakup cross sections of the neutron rich Be isotopes $^{10-14}$Be. The breakup process can be used to probe the cluster structure in the ground state via the overlap of the ground state and excited state above helium decay threshold. The experimental results indicate that the degree of clusterization in the ground state remains high and consistent from ^{10}Be up to the dripline ^{14}Be. An enhancement of the cluster breakup cross sections in ^{14}Be by comparison with its isobar nuclei ^{14}B [15], supports a larger structural overlap of the ground state and states above the breakup thresholds, indicating that ^{14}Be has a well developed cluster structure in the ground state which is in line with the idea of clustering development at the drip line.

With the development of the RI beam with intense beam rate in recent years, this has made it possible to access structural properties of the Be isotopes by cluster quasifree(QFS) reactions. The present QFS study of neutron-rich Be isotopes ^{10,12,14}Be$(p, p\alpha)$ reaction will provide a direct and quantitative measurement of the clustering in these nuclei.

1.2 Cluster quasi-free reaction - a probe for α clustering

Cluster QFS, also named cluster knockout reactions induced by protons have been extensively used from the 80's to probe the cluster structure of nuclei. In this section, the characteristics of the reaction will be described. Then we will briefly present the Distorted Wave Impulse Approximation(DWIA) reaction model used to analyze the measured cross-section, and introduce the recent progress that will allow deeper insight into the cluster structure of nuclei.

1.2.1 Cluster QFS reactions

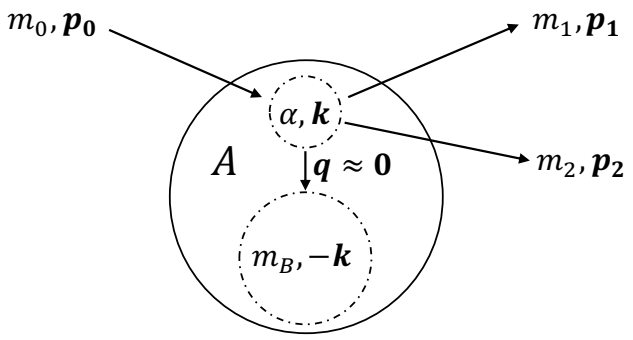

Figure 9 Schematic view of the quasi-free scattering reaction A($p, p\alpha$)B in the rest frame of the nucleus A

Figure 9 shows a schematic view of the quasi-free scattering reaction A($p, p\alpha$)B in the rest frame of nucleus A, where particle 0 is the incoming proton, particle 1 and 2 are the outgoing proton and α clusters, and B the residual nucleus. The incident proton knocks out a bound cluster from a specific orbital in A, resulting in three particles in the final state, namely the residual nucleus B, and two outgoing particles proton and alpha.

Quasi free scattering proceeds in an analogous way to free scattering between the incident projectile and cluster bound inside nucleus. At high incident energy region (Typically 100 - 1000 MeV/u), the interaction between projectile and target nucleus is strongly localized with surroundings nucleons, since the de Broglie wavelength of the projectile is comparable with the average internucleon distance and the influence of spectator nucleons can be neglected. The QFS process involves a probe particle which interacts directly with the alpha cluster inside the nucleus without transferring any momentum to the nucleus B ($\mathbf{q} \approx 0$), During the actual process, B can be left in an excited state, which energy can be determined applying the energy conservation law, The binding energy B_N of the state can be calculated as follows:

$$B_N = S_N + E_B^* = T_0 - (T_1 + T_2 + T_B) S_N = (M_A - M_B - m_2)c^2 \qquad (1)$$

where S_N is the separation energy of bond clusters, M_A, M_B and m_2 are the masses of the mother, residual and the cluster, respectively. T denotes kinetic energies of particles.

1.2.2 The DWIA for cluster QFS reactions

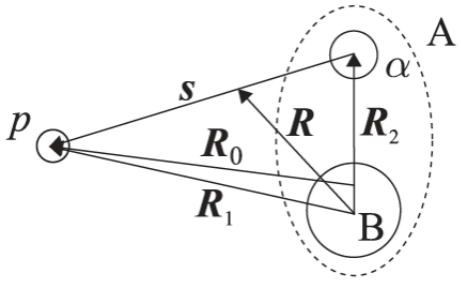

Figure 10 Coordinates of A$(p, p\alpha)$B reaction [16]

The proton induced knockout reaction $(p, p\alpha)$ is an single-step direct reaction. The α particles can not be knocked out from the interior of the nucleus, due to the strong absorption effect. Therefore, only α cluster on the nuclear surface can be selectively probed by this reaction. This is a great advantage of using the $(p, p\alpha)$ reaction to study the cluster structure, since the cross section is highly sensitive to the structures on the nuclear surface.

The Distorted-Wave Impulse Approximation(DWIA) reaction model is an standard framework to calculate the cross sections. It has successfully been applied for quasifree knockout reactions to reproduce experimental data[17]. Following notation of [13, 16, 18], the transition amplitude for A$(p, p\alpha)$B reaction within the DWIA framework is given by

$$T_{\boldsymbol{P_0 P_1 P_2}} = \left\langle \chi^{(-)}_{1,\boldsymbol{P_1}}\left(\boldsymbol{R}_1\right) \chi^{(-)}_{2,\boldsymbol{P_2}}\left(\boldsymbol{R}_2\right) \left| t_{p\alpha}(\boldsymbol{s}) \right| \chi^{(+)}_{0,\boldsymbol{P}_0}\left(\boldsymbol{R}_0\right) \varphi_\alpha\left(\boldsymbol{R}_2\right) \right\rangle \tag{2}$$

Figure 10 shows the coordinates of A$(p, p\alpha)$B reaction. In Eq. 2 the proton in target, the outgoing proton, and the knockout α are labeled by 0, 1, and 2, respectively. The momentum $\boldsymbol{P}$ and the distorted waves χ are specified with these numbers in subscripts. χ_0, χ_1, and χ_2 are the distorted wave functions of the p-A, p-B, and α-B systems, respectively. The superscripts $(+)$ and $(-)$ on χ indicate that the outgoing- and incoming-wave boundary conditions are adopted, respectively. φ_α is the α-cluster wave function. The transition interaction $t_{p\alpha}$ for free p-α scattering can be obtained by a folding model calculation [16].

With transition amplitude in Eq. 2, the triple differential cross-section (TDX) of

the $(p, p\alpha)$ reaction is given by

$$\frac{d^3\sigma}{dE_1^L d\Omega_1^L d\Omega_2^L} = F_{\text{kin}} C_0 \frac{d\sigma_{p\alpha}}{d\Omega_{p\alpha}}\left(\theta_{p\alpha}, E_{p\alpha}\right)\left|\bar{T}_{\boldsymbol{P_0 P_1 P_2}}\right|^2 \tag{3}$$

Here $\theta_{p\alpha}$ is the scattering angle of the p-α binary collision and $E_{p\alpha}$ is its scattering energy defined by

$$E_{p\alpha} = \frac{\hbar^2 \kappa'^2}{2\mu_{p\alpha}} \tag{4}$$

where $\mu_{p\alpha}$ is the reduced mass of the p-α system and $\kappa\prime$ is the relative momentum between the emitted p and α cluster in the final channel. F_{kin} in Eq. 3 is the kinematical factor defined as

$$F_{\text{kin}} = J_L \frac{P_1 P_2 E_1 E_2}{\hbar^4 c^4}\left[1 + \frac{E_2}{E_B} + \frac{E_2\left(\boldsymbol{P}_1 \cdot \boldsymbol{P}_2\right)}{E_B P_2^2}\right]^{-1} \tag{5}$$

where J_L is the Jacobian from the center-of-mass frame to the laboratory frame. C_0 in Eq. (4) is a coefficient given by

$$C_0 = \frac{E_0}{(\hbar c)^2 K_0}\frac{\hbar^4}{(2\pi)^3 \mu_{p\alpha}^2} \tag{6}$$

In most DWIA calculations performed to date to analyse cluster QFS experiments, the alpha-cluster wave-function φ_α was determined by simply solving the Schrödinger equation for an alpha particle moving in a Woods-Saxon potential which depth was adjusted to reproduce the binding energy of the alpha-particle in nucleus A. That is [19]:

$$\left[-\frac{\hbar^2}{2\mu_\alpha}\nabla_R^2 + V_{\alpha\text{B}}(R)\right]\varphi_\alpha^{nlm}(\boldsymbol{R}) = \varepsilon_\alpha \varphi_\alpha^{nlm}(\boldsymbol{R}) \tag{7}$$

where $\mu_\alpha, V_{\alpha\text{B}},$ and ε_α are the reduced mass, the binding potential, and the binding energy of the $\alpha - B$ system, respectively. $\varphi_\alpha^{nlm}(\boldsymbol{R})$ is the α cluster wave function, nlm are the three quantum numbers describing shell, orbital angular momenta, and spins, respectively

The TDX can then be expressed as

$$\frac{d^3\sigma}{dE_1^L d\Omega_1^L d\Omega_2^L} = S_\alpha F_{\text{kin}} C_0 \frac{d\sigma_{p\alpha}}{d\Omega_{p\alpha}}\left(\theta_{p\alpha}, E_{p\alpha}\right)\sum_m \left|\bar{T}_{\boldsymbol{P}_i}^{nlm}\right|^2 \tag{8}$$

where $\bar{T}_{\boldsymbol{P}_i}^{nlm}$ is the transition amplitude and S_α is the alpha spectroscopic factors. It is

often considered as a measure of the degree of clusterization of the populated state. Experimentally, it is obtained by normalizing the calculated cross-section to the data.

$$\frac{d^3\sigma^{exp}}{dT_1 d\Omega_1 d\Omega_2} = S_\alpha \frac{d^3\sigma^{calc}}{dT_1 d\Omega_1 d\Omega_2} \tag{9}$$

Recently, it was proposed to use microscopic cluster wave functions instead of the above phenomenological wave function. In particular, reaction calculations using an extended version of the Tohsaki-Horiuchi-Schuck-Röpke (THSR) [20] function to calculate the cluster wave-function were performed for the ^{10}Be$(p, p\alpha)$ [13] and ^{12}Be$(p, p\alpha)$ [18] reaction. The THSR function provide a microscopic description of the wave-functions of the initial nucleus A and residue B. The work reported in [13, 18] show that the $(p, p\alpha)$ reaction provides a stringent test of the wave-functions of ^{10}Be and ^{12}Be used in the reaction modelling. The present work aims to check the validity of the above description of the neutron-rich ^{10}Be and ^{12}Be by measuring the relevant observables. This implies the measurement of the $(p, p\alpha)$ reaction in inverse kinematics using RIB of ^{10}Be and ^{12}Be.

1.2.3 $(p, p\alpha)$ experiments in forward kinematics and inverse kinematics

A lot of $(p, p\alpha)$ reaction studies have been performed since the 80's using proton beams with incident energy larger than 100 MeV and stable target in so-called forward or direct kinematics[17, 21, 1, 22, 23]. Figure 11 shows an example of results obtained in such measurement using the ^{9}Be$(p, p\alpha)$ reaction at a bombarding energy of 200 MeV[23]. It represents the TDX as a function of scattered proton energy, for a given angle pair $(\theta_p, \theta_\alpha)$. In the experiment, angle pairs are chosen so that the quasifree condition ($\mathbf{p_B} \approx 0$) is fulfilled. The TDX spectrum shows a prominent quasifree-knockout contribution well reproduced by theoretical DWIA predictions. For a transferred momentum L = 0 in the reaction, the TDX distribution is peaked at the proton energy T_p corresponding to $\mathbf{p_B} = 0$ (QF or recoilless condition). The contribution of L = 2 component is also shown. The alpha Spectroscopic factor(SF) was extracted by normalization of the calculated DWIA TDX to the data and compared to shell model calculation. These results confirms that DWIA provides a satisfactory description of $(p, p\alpha)$ at the QFS energy region.

To study the $(p, p\alpha)$ reaction on neutron-rich unstable nuclei, it is needed to realize the experiment in so-called inverse kinematics in which the interaction takes place

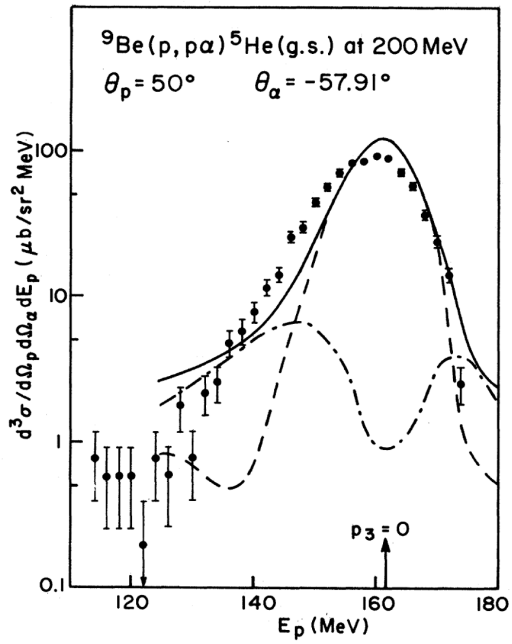

Figure 11 TDX spectrum for the ^{9}Be$(p, p\alpha)^5$He reaction at angle pair 50°/ -57.91°. The curves represent DWIA calculations for L = 0 (dashed), L = 2 (dot-dashed), and their incoherent sum (solid) from literature[23]

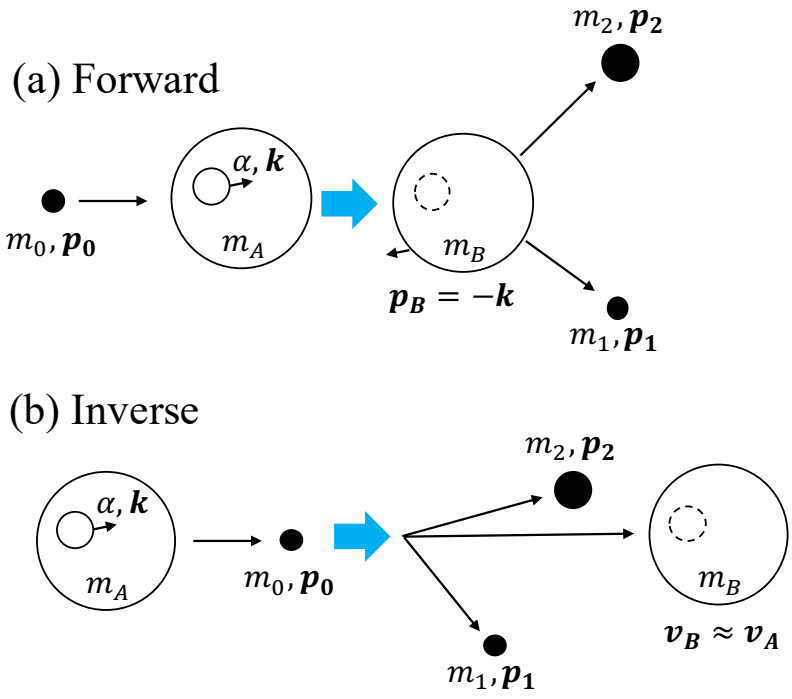

Figure 12 Forward and inverse kinematics of cluster QFS reaction

between the beam ion and a proton target. Figure 12 shows a scheme comparing forward and inverse kinematics measurement of cluster QFS reaction.

In forward kinematics, both proton and α-cluster are measured at large angle. The residue B with momentum $\mathbf{q} \approx 0$ is stopped in the target. In inverse kinematics, the residues after reaction continue to travel at a projectile-like velocity. This feature enables the identification of residual nuclei after the reaction. For the study of $(p, p\alpha)$ reaction in this thesis, we have to use inverse kinematics with neutron-rich beams of Be isotopes produced at 150 MeV/u with high intensity at the RIBF facility. The kinematic quantities are completely determined from the measurement of proton and α cluster with the help of conservation laws of energy and momentum.

1.2.4 Some kinematical characteristics of cluster QFS experiments in inverse kinematics

The kinematics of cluster QFS experiments show different features than forward kinematics ones. This is illustrated in Figure 13 which displays the kinetic energy correlation of T_p vs T_α for a fixed angle pair(θ_p,θ_α) in ^{10}Be$(p, p\alpha)$ reaction. where the incident beam energy $T_{beam} = 150$ MeV/u is assumed in both kinematics. The selected angle pairs (65°, 7.7°) in inverse kinematics and (32.8°, 66.4°) in forward kinematics are corresponding to the same scattering angle in the center of mass frame. The kinematical formula are reported in Appendix I.

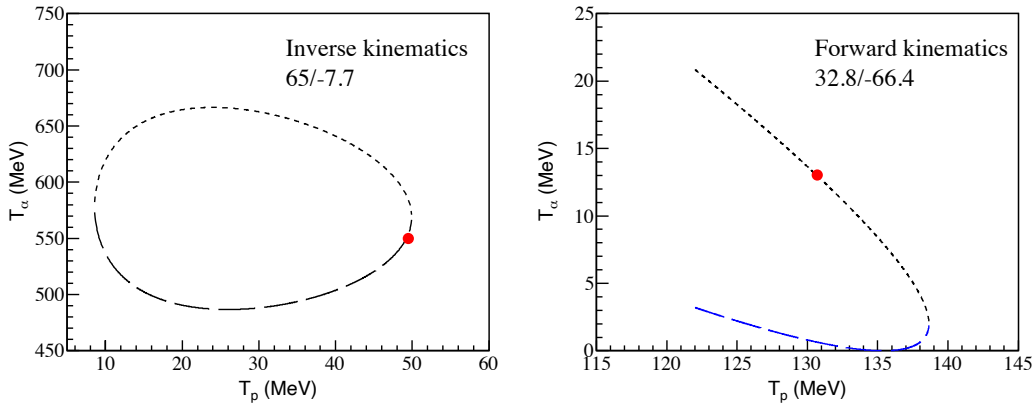

Figure 13 T_α vs T_p correlation for a single angle pair(θ_p,θ_α) for ^{10}Be$(p, p\alpha)$ reaction. (a) angle pair (65, 7.7) in inverse kinematics; (b) angle pair (32.8, 66.4) in forward kinematics

In Figure 13, the T_p and T_α correlation in the inverse kinematics case is a closed loop, In the case of forward kinematics, alpha energies are rather small so that

thin targets have to be used in experiments. Red dot is the QFS condition points corresponding to $p_B = 0$.

1.2.5 Previous $(p, p\alpha)$ reaction experiments in inverse kinematics

To date, a few cluster QFS studies have been performed in inverse kinematics for investigations of the cluster structure of neutron-rich nuclei.

Chulkov *etal*. investigated the $(p, p\alpha)$ reaction with radioactive ^{6}He and ^{8}He beams at 717 and 671 MeV/u, respectively, impinging on a liquid-hydrogen target [24]. The dominance of the QFS reaction mechanism has been proven for the neutron-rich nuclei by the kinematical correlations between the detected particles in their polar and azimuthal angles. Spectroscopic factors of different cluster configurations were deduced from the experimental data as well as the internal momentum distributions of the clusters inside ^{6}He and ^{8}He for the first time. The dominant contribution of the ^{6}He+2n configurations in the ^{8}He nucleus has been observed from the experimental results of $(p, p^{6}\mathrm{He})$ channel.

Another similar knockout experimental study conducted in 2012 [25] using an ^{8}He beam at 82.5 MeV/u produced at the RIPS separator at RIKEN. The recoil protons were measured in coincidence with the forward ^{6}He core fragments and neutrons. The absolute differential cross sections could be deduced based on the quasi-free scattering mechanism for ^{6}He core fragment. The SF of of ^{6}He cluster in ^{8}He was found to be close to 1.0 and a shrinking of the ^{6}He core cluster inside a ^{8}He nucleus was also suggested with comparison to elastic scattering data.

1.3 Present $(p, p\alpha)$ study for neutron-rich Be isotopes

The present thesis work is dedicated to the first experimental study of the $(p, p\alpha)$ reaction on neutron-rich Be isotopes in inverse kinematics, using radioactive beam of ^{10,12,14}Be provided by the RIBF facility impinging on a solid hydrogen target. The goal of the experiment is to directly and quantitatively study the degree of clustering existing in the ground state of Be isotopes below the α threshold. The measurement of incident beam particles and outgoing reaction residues were achieved by using SAMURAI spectrometer and its standard detectors. The experimental setup is detailed in Chapter 2 and the calibrations of detectors are presented in Chapter 3. In Chapter 4, excitation energy spectra of the residual nucleus extracted by missing mass

Table 1 Kinematical conditions

kinematics	^{10}Be$(p,p\alpha)$	^{12}Be$(p,p\alpha)$	^{14}Be$(p,p\alpha)$
θ_{CM}	40°-70°	40°-70°	40°-70°
θ_p	50°-70°	50°-70°	50°-70°
θ_α	4°-12°	4°-12°	4°-12°
E_p	30-100 MeV	30-100 MeV	30-100 MeV
E_α	400-650 MeV	400-650 MeV	400-650 MeV
Residue	^{6}He	^{8}He	^{8}He
$B\rho$(residue)	5.1 -5.5 Tm	6.9-7.4 Tm	6.9-7.4 Tm

method and cross-sections are extracted from the yields of knocked-out α-cluster detected in coincidence with the protons.

In the measurements of $(p,p\alpha)$ reaction with proton beams on stable targets, it has been argued that absolute alpha spectroscopic factors (SF) can be extracted with good accuracy in the incident energy domain around 100-200 MeV/u using distorted-wave impulse approximation (DWIA) calculations. A reasonable energy of beam 150 MeV/u have to be selected to reduce the distortion effect and be able to separate sequential decay processes from direct quasi free knockout reaction. The knocked-out cluster is measured in coincidence with the projectile, and the recoil proton. The kinematical conditions of the QFS measurement for the ground state transition are reported in Table 1. The corresponding scattering angle in center of mass for the free p+α elastic scattering is in range of 40°-70°.

TDX for the ^{10}Be$(p,p\alpha)$ and ^{12}Be$(p,p\alpha)$ reactions to the ground-state of ^{6}He and ^{8}He, respectively are extracted and compared with up-to-date DWIA cross-sections calculated with alpha-cluster wave function deduced from extended version of the THSR function [26]. Experimental cross-sections for the population of the 2^+ state in ^{6}He and ^{8}He residues are also obtained. These latter quantities provide a direct measurement of the contribution of ^{6}He and ^{8}He core excited states to the ground-state wave-function of ^{10}Be and ^{12}Be, respectively.

Chapter 2

Experimental Setup

This chapter describes the setup of the experiment, performed at the Radioactive Isotope Beam Factory (RIBF) at RIKEN Nishina Center [27]. The goal of this experiment was to study the cluster structure of neutron-rich Beryllium isotopes using quasi-free $(p, p\alpha)$ reaction in inverse kinematics. Section 2.1 gives an overview of the experimental setup. Section 2.2 briefly explains the radioactive isotope(RI) beam production and transportation. The following Section 2.3, 2.4, 2.8, 2.9 describe the SAMURAI spectrometer and its detectors for the detection of the incoming beam and outgoing reaction products. Section 2.5 introduces the details of the secondary target. In addition to the standard detectors, there were two other sets of detectors specifically integrated for this experiment. Section 2.6 introduces the ESPRI setup for the recoil proton detection. Section 2.7 describes the ensemble telescopes employed in the detection of the knocked-out clusters. Finally, Section 2.10 presents the trigger conditions and the run summary of the experiment.

2.1 Overview of setup

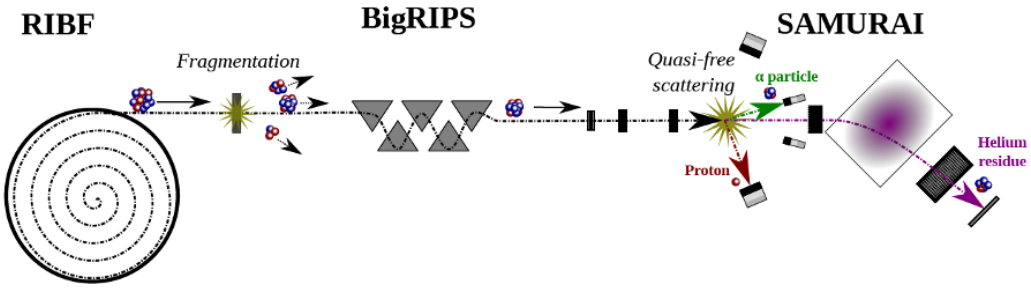

Figure 14 Overview of experimental setup.

The SAMURAI12 experiment was performed at the Radioactive Isotope Beam Factory (RIBF) in RIKEN. Figure 14 shows an overview diagram of the experimental setup. The ^{10,12,14}Be secondary beams at approximately 150 MeV/u were produced and separated by the BigRIPS separator [28], using the fragmentation of an ^{18}O

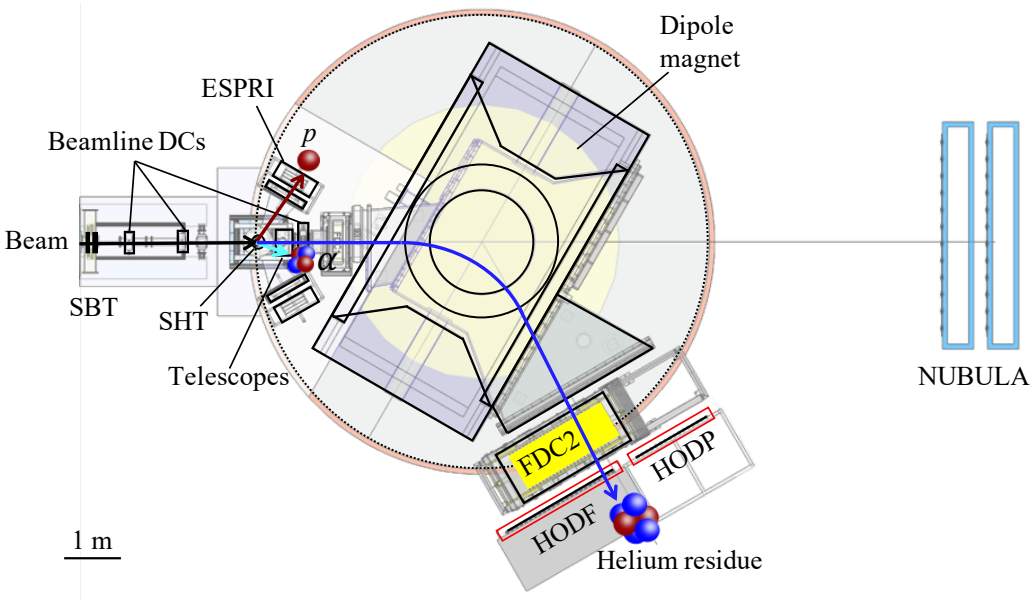

Figure 15 Scheme layout of experimental setup around SAMURAI area.

primary beam at 230 MeV/u impinging on a thick Be target. The $(p, p\alpha)$ reactions of interest were studied using the SAMURAI large acceptance spectrometer [29]. A detailed scheme layout of the SAMURAI area is shown in Figure 15. The incident ^{10,12,14}Be secondary beam entered the setup from the left-hand side and impinged on the solid hydrogen target (SHT). The fragments from the reaction were measured with various detectors indicated in the figure.

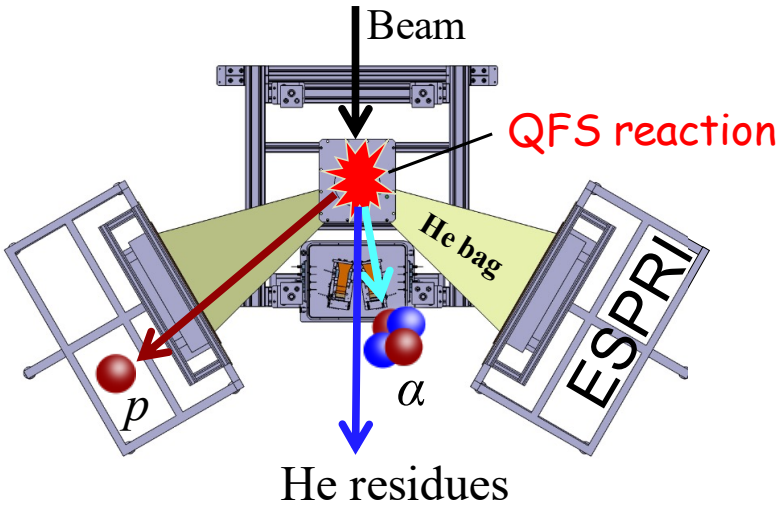

Figure 16 Schematic view of $(p, p\alpha)$ reaction setup around the target system

Figure 16 shows a schematic view of $(p, p\alpha)$ reaction setup around the SHT system. This combination of detectors allows the determination of the excitation energy of the

populated states in the reaction residues. The trajectories of the incident beam were reconstructed by two identical beam drift chambers (BDC1, BDC2) separated by 1m distance and placed upstream of the target. The reaction target was a 2 mm thick SHT [30] with a standard diameter of 30 mm. The ESPRI Recoil Proton Spectrometer (RPS) system was implemented in a two-arm configuration for the recoil proton detection. It is composed of 3 stages: first a multi-wire drift chamber (MWDC) for scattering angle determination, followed by a large area plastic detector, and finally an array of NaI rods. The two arms were placed at approximately 1m from the SHT, covering an angular range of $50° - 70°$ in the lab system, corresponding to about $40° - 70°$ in center of mass (CM) for the free α+p elastic scattering. Velocity-like knocked out clusters were measured by two telescopes composed of double-sided strip Silicon detector (DSSD) and CsI(Tl) detectors placed at forward angles to cover the angular range $4° - 12°$. The second stage was composed of CsI(Tl) crystals 6 cm and 5 cm long. A dedicated calibration run with alpha beam was used in order to achieve precise energy calibration of these telescopes needed to deduce the missing mass spectra.

The detection of ^{4,6,8}He residues near zero degrees produced in the ^{10,12,14}Be$(p, p\alpha)$ reactions was performed by using the SAMURAI spectrometer and its standard detectors, shown in Figure 15. The Forward Drift Chamber (FDC0) placed around 1.2 m upstream of SAMURAI entrance was implemented for measuring the scattering angle of the He residues. After the residues reached the large gap (80 cm) vacuum chamber of the magnet, they deflected differently as function of their mass, charge, and momentum by the magnetic field and subsequently passed through the exit window of SAMURAI. Particle identification and rigidity measurement of the residues were achieved using FDC0 and FDC2 drift chambers placed before and after the magnet, and the HODP and HODF walls of plastic detectors composed of 16 and 24 slats of BC408 scintillators placed vertically. The undeflected neutrons passing through the SAMURAI magnet gap were detected by two walls of plastic scintillators of the NEBULA array [29] for complementary invariant mass studies.

2.2 Beam production

RIBF facility called in full name "**R**adioactive **I**sotope **B**eam **F**actory" in RIKEN [27] is capable of providing RI beams of all elements, energies and intensities of several hundreds MeV/nucleon. A primary ^{18}O beam was accelerated up to 230 MeV/u by AVF+RRC injection mode and bombarded a ^{9}Be production target installed at the F0 focal plane of BigRIPS in-flight fragment separator [28]. Fragmentation process

generates a large variety of nuclei with lower mass and charge than the primary isotope.

2.2.1 Primary beam: RIBF accelerators

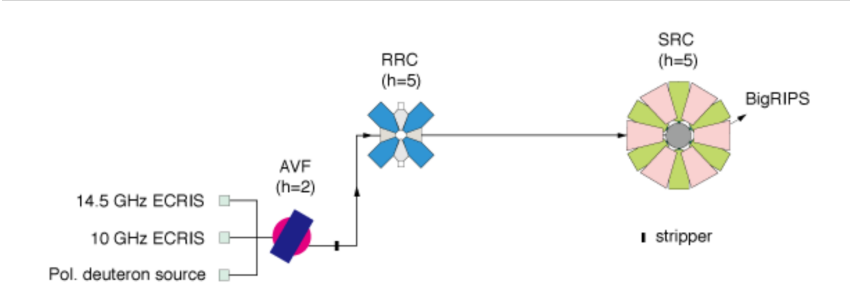

Figure 17 AVF+RRC+SRC acceleration mode

The RIBF heavy-ion accelerator system has different kinds of cyclotrons and injectors: RILAC, RRC, AVF, fRC, IRC and SRC [27] with multiple operational modes depending on the mass and charge and energy region of interest for the accelerated particle. AVF+RRC+SRC injection mode, as Figure 17 shown, was applied to the particular case of the acceleration of ^{18}O primary beam for this experiment, The Oxygen ions were extracted by an ECR ion source and then accelerated up to 230 MeV/nucleon using cascade accelerators: AVF, RRC and finally SRC. Stripper was placed between the AVF and RRC to make the isotope fully stripped at the entrance of RRC.

2.2.2 Secondary beam: BigRIPS

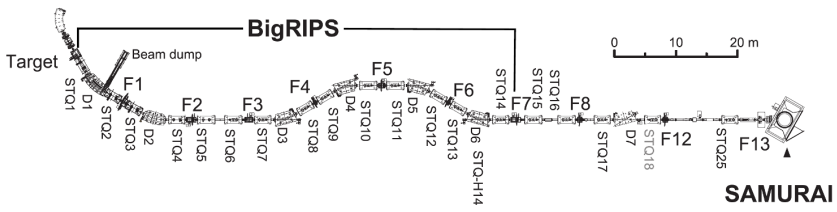

Figure 18 Schematic overview of beamline from BigRIPS separator to the SAMURAI spectrometer

BigRIPS [28] is an in-flight RI beam separator with large acceptances due to the usage of superconducting quadrupoles with large apertures. Production of intense

RI beams has been realized for a wide range of masses and isospin. BigRIPS separator is designed to be a two stage RI beam separator. The first stage (F0-F2) of BigRIPS separator serves to produce and separate RI beams; while the second stage (F3-F7) serves to identify RI-beam species in an event by event mode. Figure 18 give a schematic overview of beamline from BigRIPS separator to the SAMURAI spectrometer.

The first stage comprises two-bend achromatic spectrometer, consisting of 4 superconducting quadrupole triplets (STQ1 to STQ4) and two room-temperature dipoles (RTD) with a bending angle of 30° (D1 and D2). A wedge-shaped degrader is placed in the middle of focus F1 to make isotopic separation based on the momentum achromat technique. A high-power beam dump is placed at the first dipole D1 in order to stop primary heavy ion beams. About 10,000 tons of thick concrete blocks is built for shielding neutron radiation produced in 1st stage. Two STQs (STQ5 and STQ6) placed after the achromatic focus F2 form a telescopic system to transport separated RI beams to the second stage. The second stage from the F3 focus to the F7 focus consists of 8 STQs (STQ7 to STQ14) and 4 RTDs with a 30° (D3 to D6) bending angle, comprising a four-bend achromatic spectrometer. The intermediate focuses F4, F5 and F6 are momentum-dispersive, while the final focus F7 is doubly achromatic. Detailed parameters can be found in Table 2.

The tagged RI beams can be delivered to three different branches in RIBF facility: ZeroDegree, SHARAQ, and SAMURAI spectrometers, as shown in Figure 19. For this experiment, the SAMURAI spectrometer at F13 was connected to the delivery line of BigRIPS and the optics for the transport were tuned to focus the secondary beam on target spot.

2.3 SAMURAI spectrometer

SAMURAI (**S**uperconducting **A**nalyzer for **Mu**lti-particles from **Ra**dio **I**sotopes) is a large-acceptance spectrometer for RI-beam experiments [29]. The SAMURAI magnet is located downstream the straight section of the BigRIPS, as shown in Figure 18.

The SAMURAI spectrometer has been designed and constructed for kinematically complete measurements. The standard detectors of SAMURAI setup consists of a large amount of detectors that include beam line plastic scintillators, beam drift

Table 2 BigRIPS parameters

Type	Seperate sector
Separator config	Tandem
The first stage	TQ-D-TQ-TQ-D-TQ
The second stage	TQ-D-TQ-TQ-D-TQ-TQ-D-TQ-TQ-D-TQ
Degrader type	Wedge @F1, F5, F4, F6
Magnet type	Dipole : Normal conducting
	Quadrupole : Super conducting
Angular acceptance	Horizontal : 80 mrad
	Vertical : 100 mrad
Momentum acceptance	6 %
Maximum rigidity	9 Tm
Total path length	78 m (F0-F7)
Momentum Dispersion	First stage : -2.31 cm/%
	Second stage : 3.3 cm/%
Momentum Resolution	First stage : 1290
(dX=1mm)	Second stage : 3300
Focal plane	F1 : momentum dispersive
	F2,F3 : achromatic
	F4,F5,F6 : momentum dispersive
	F7 : doubly achromatic

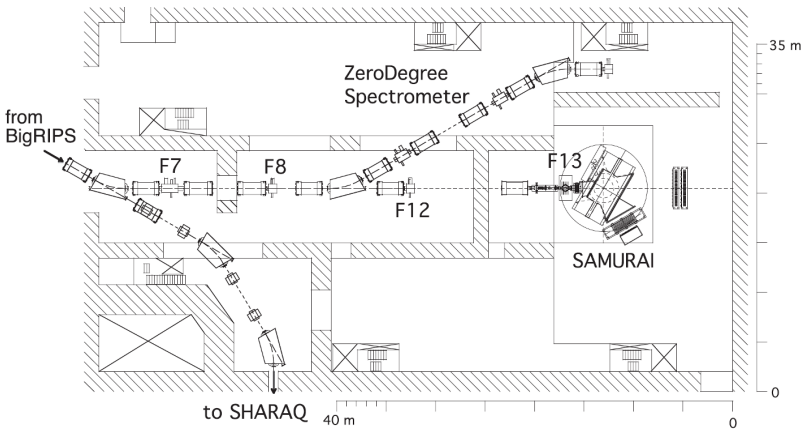

Figure 19 Continued schematic layout of BigRIPS beamline [29]

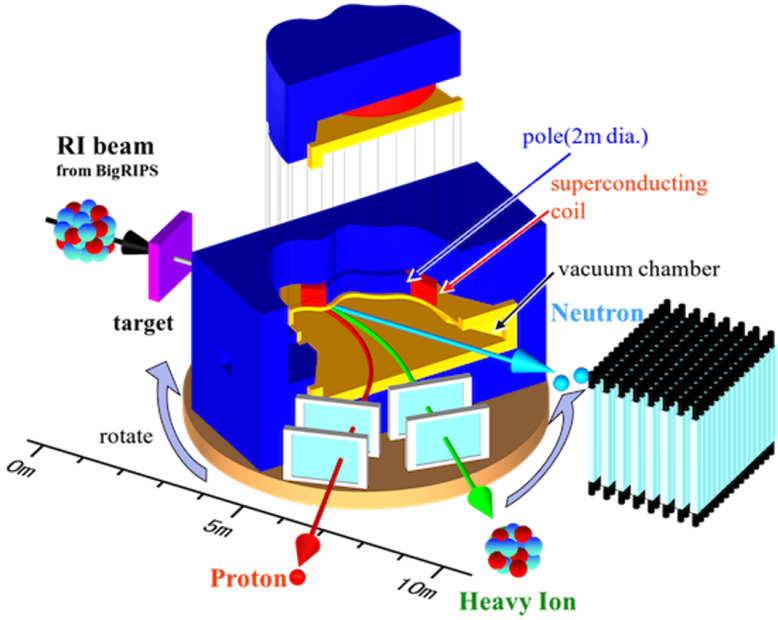

Figure 20 Scheme of SAMURAI spectrometer

detectors (BDC), forward drift chambers (FDC), charged fragments detector (Hodoscope), and neutron detector (NEBULA). Figure 20 shows a schematic view of the SAMURAI spectrometer. Additional detectors can be included depending on the requirements of the experiment.

2.3.1 SAMURAI Magnet

The SAMURAI magnet is the main component of the SAMURAI spectrometer system. Neutrons emitted from the reaction go straight into NEBULA while charged fragments are bent by the SAMURAI magnet depending on its physical properties, like mass, charge, and momentum. The function of the SAMURAI magnet is to separate reaction products, and ensure their rigidity measurement.

The SAMURAI magnet is a H-type dipole with a diameter of 2 m cylindrical pole. The opening area of the large pole gap is 294 cm horizontally and 80 cm vertically for both exit windows making the opening angle of $\pm 5°$ vertically and $\pm 10°$ horizontally. It allows large acceptances for the detection of multiple kinds of reaction products, such as projectile-rapidity neutrons, and flexibility for various types of measurements. The SAMURAI magnet is rotatable and was fixed at 30° during the experiment. The maximum bending power of the SAMURAI magnet is 7.05 Tm, as required for the requirements of experiments with RI beams. The key parameters of the SAMURAI

dipole magnet are listed in Table 3.

Table 3 Key parameters of SAMURAI Magnet [29].

Parameter	Value
Type	H-type
Pole	ϕ2 m, 0.88 m (gap)
Maximum field	3.1 Tm
Maximum field integral	7.1 Tm
Number of turns	3413 turns/coil
Maximum current	563 A
Magneto motive force	1.9 MAT/coil
Stored energy	27.4 MJ
Coil cross section	180 mm $\times$ 160 mm
Current density	67 A/mm^2
Total weight	600 ton

Table 4 Magnetic flux density applied for each beam setting

Beam	Magnetic field
^{10}Be	2.1T
^{12}Be	2.7T
^{14}Be	2.5T

Table 4 gives the magnetic flux density applied for each beam setting during the experiment. These values were carefully chosen based on trajectory calculations of the beam and residues of interest. Figure 21 shows the trajectories calculations for the Be isotopes and He residues at projectile-like velocity. FDC2 was turned off in case of ^{10,12}Be beams, while it was turned on in case of ^{14}Be for a precise rigidity measurement of alpha particles. Owing to the large momentum acceptance and focal-plane detectors coverage, the ^{4,6,8}He could be detected for each beam setting.

2.4 Beamline detectors

Beamline detectors consisting of plastic scintillators and drift chambers were installed upstream of target for the measurement of the beam particles. Plastic

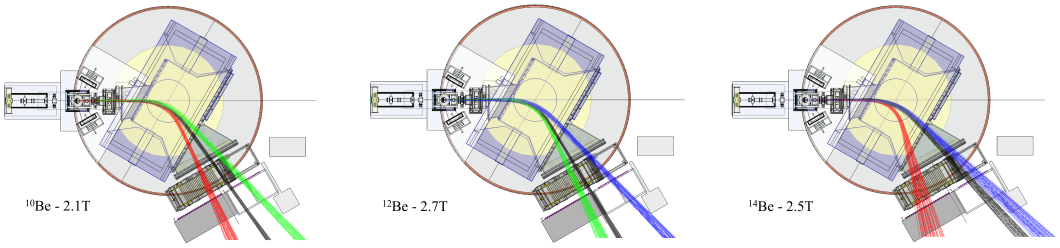

(a) $^{10}Be(p,p\alpha)$ (b) $^{12}Be(p,p\alpha)$ (c) $^{14}Be(p,p\alpha)$

Figure 21 Trajectory calculations for beam and residues of interest in the case of ^{10}Be,^{12} Be and ^{14}Be beams at 150 MeV/u. (Color code black:beam; red:^{4}He; green:^{6}He; blue:^{8}He)

scintillators with 1 mm thickness for all were installed at F3, F7, F13 focal planes. Energy loss and time signals from these detectors were used for particle identification and to determine the incident energy of the beam event by event. The incident beam particle trajectories can be reconstructed from the position information provided by the drift chambers at F13(BDC1, BDC2) and the beam profile on target be deduced. Hence, the four-momentum vector of the beam particle can be reconstructed by the beamline detectors.

2.4.1 Beam Plastics

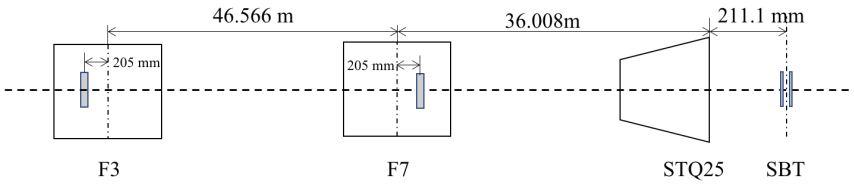

Figure 22 Relative distances between plastic scintillators at different focal planes

Figure 22 shows a scheme of relative positions between the plastic scintillators placed at F3, F7, and F13 focal planes along the BigRIPS beamline. These plastic scintillators are used for timing and energy loss information of incoming beam particles. Particle identification of the incoming beam is done by $\Delta E - TOF$ method. The mean energy of the slightly dispersive beam was determined from the Bρ value of D6 magnet. Two photo-multiplier tubes (PMTs) were coupled to both ends of the plastic scintillator and the timing of each scintillator was calculated by the average value of both time signals. SBT detectors of F13 located at downstream of STQ25

consists of two plastic scintillators SBT1 and SBT2. Signals from SBT1 and SBT2 were employed as the time start signal and for generating the beam trigger, see more details in section 2.10. The distance between F7 and F13 (the middle position of SBT1 and SBT2) was 36014.1 mm in our experiment.

2.4.2 Beam drift chamber: BDC1,BDC2

Table 5 BDC parameters

Drift length, pitch	2.5 mm, 5 mm
Anode, potential wire	ϕ20 rmum Au-W/Re, 80 μmϕ Au-Al
Cathode (gas window)	8 μm^t Al-Kapton $\times$ 9 (2)
Configuration	xx'yy'xx'yy' (8 planes)
Effective area	80 mm $\times$ 80 mm
Readout	128 ch/chamber
Operating gas	i-C4H10 at 100 (50) torr
Vacuum window	80(16) μm^t Kapton $\times$ 2
Thickness	L/Lr = 0.9 $\times$ 10^{-3}

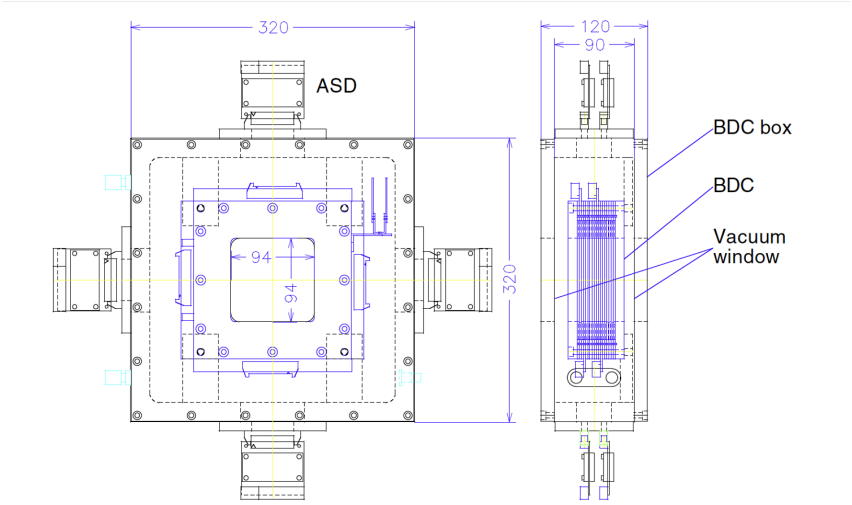

Figure 23 Schematic view of the BDC detector [29].

Two identical **B**eam **D**rift **C**hamber (BDC1 and BDC2) were mounted upstream of the target and placed at 1m distance from each other for beam tracking. The SHT was 1.4m downstream from the BDC2 detector. The trajectories of incoming beam were reconstructed event by event from the positions of BDCs with a position resolution of typically 150 μm in sigma [Kobayashi:2013] as will be shown below.

Figure 23 presents a schematic view of the BDC detector. The effective area of BDCs is 80×80 mm^2. It consists of 8 layers of wires with 4.8 mm spacing and the orientation of wires is configured as XX'YY'XX'YY'. Each layer has 16 wires with 5 mm pitches. Adjacent parallel planes in the same orientation are shifted by 2.5 mm, such as XX' pair, in order to improve spatial resolution. Detailed parameters can be found in Table 5. BDCs are operated at 50 Torr filling with isobutane (C4H10). When a beam particle passes through, the gas atoms in the chamber are ionized. Due to the electric field, the released ion-electron pairs drift towards the cathodes and anodes, respectively. Measuring drift time makes it possible to calculate the relative position to the wire. The trajectories of beam particles are calculated based on the positions in each layer. See Section 3.2 for details of the calibration and trajectory reconstruction with BDCs.

2.5 Solid Hydrogen Target(SHT)

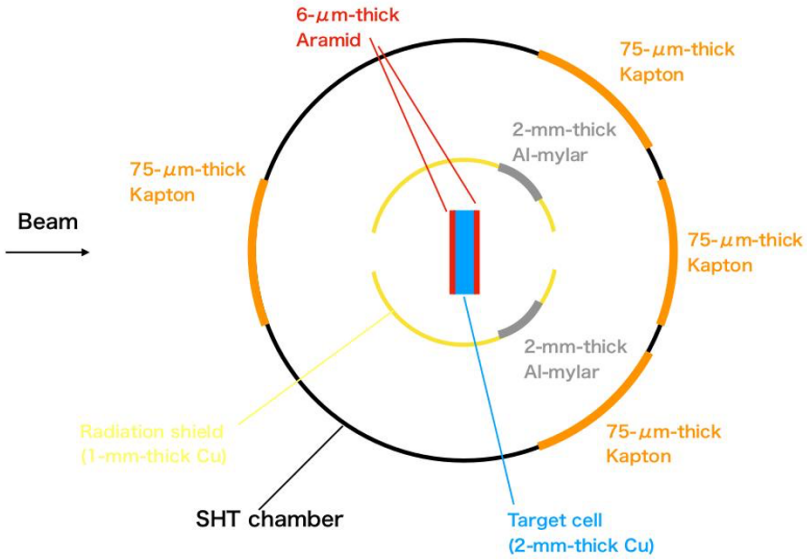

Figure 24 Window materials around the SHT

In direct kinematics experiments, proton induced reactions on stable nucleus target have shown great merit in nuclear structure studies. For reaction studies with the exotic beam in inverse kinematics, proton targets are needed. CH2 targets as an alternative have been commonly used. Polyethylene CH_2 is the most affordable material and easy to manufacture into any required form. However, the presence of carbon atoms in this material is a great source of parasitic reactions background. In contrast, solid hydrogen targets offer good purity for experiments that are highly

sensitive to background contamination. Moreover, a pure hydrogen target gives a much smaller angular straggling, compared to the same amount of protons in the CH_2 target [31].

A solid hydrogen target (SHT) [30] has been developed for the study of direct reactions in inverse kinematics. Initially designed for the study of elastic scattering, mechanical adaptations had to be performed for the present $(p, p\alpha)$ study. The reaction chamber was modified so as to allow detection of protons at around 60 degrees scattering angle. A new target frame allowed us to prepare a 2 mm thick and 30 mm in diameter target with a density of 0.086 g/cm^3(1.03×10^{22} /cm^2). Such a large area target has been made by using pure para-hydrogen (p-H2) and a mechanical press made of neodymium magnets to cope with thermal radiation from surroundings and swelling of the target during solidification.

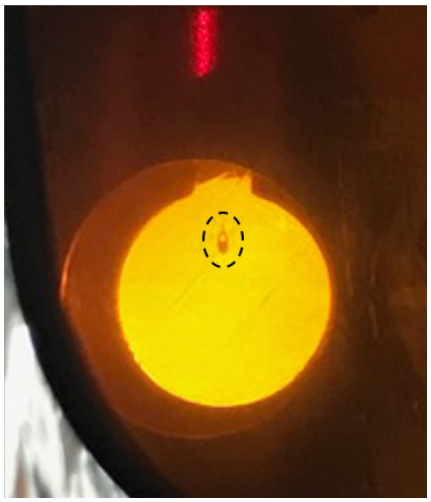

Figure 25 Photograph of SHT during the experiment, A hole is indicated by the dashed ellipse (see text).

Figure 24 shows the window materials and shielding around the SHT. The SHT was made inside of a target-size hole on a 2 mm thick copper plate covered by 2 layers of 6μm thick Aramid in the front and back side. In the SHT chamber, there are two windows for the entrance and exit of the beam and another two symmetrical exit windows at around 60° line for the recoil proton. Figure 25 shows a photograph of the SHT produced specifically for this experiment by Matsuda's team. One can observe a small hole indicated by the dashed ellipse on the top part of the target. The hole was present at the same position at the end of the experiment. As a consequence, an effective area needs to be defined for data analysis.

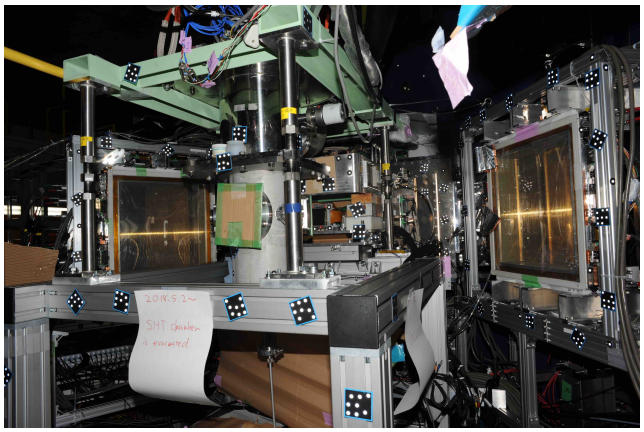

(a) Target area from the view of beam direction

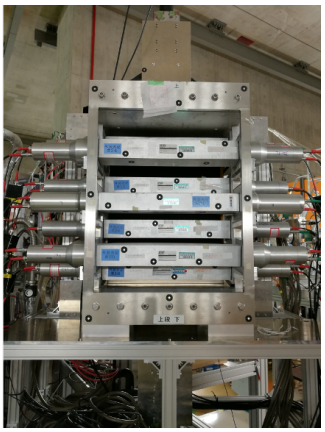

(b) NaI(Tl) array

Figure 26 Pictures of ESPRI setup

2.6 Recoiled proton detection - ESPRI Spectrometer

Table 6 ESPRI detector parameters.

RDC	Geometry	$436\times436\text{mm}^2$
	Planes configuration	XY'XY'X'YX'(7 total)
	Drift length	7 mm
	Anode spacing	14 mm
	Anode wire	$\phi = 30$ μm Au-W/Re
	Cathode wire	$\phi = 100$ μm Be-Cu
	Gas	Ar–C_2H_6 (50%)
Plastic	Dimension	$440\times440\times4\text{mm}^3$
NaI(Tl)	Dimension	$431.8\times45.72\times50.8\text{mm}^3$

The recoil proton spectrometer (RPS) was developed for the measurement of **E**lastic **S**cattering of **P**rotons by **RI** beams (ESPRI) [32]. As Figure 16 and Figure 71 show, two sets of ESPRI detectors were installed on the left and right exit windows of the SHT chamber. The two sets were placed 1m away from the target and perpendicular to 60° line refer to the beamline. ESPRI detectors mainly consist of 3 parts: multi-wire drift chamber (**R**ecoil **D**rift **C**hamber, called RDC in the following) for providing position measurement, a large area plastic scintillator made of BC-408 material for trigger signals and TOF measurement, and an array of seven NaI(Tl) scintillators for total energy measurement. In order to achieve good missing mass resolution and avoid the reaction loss of the protons in the atmosphere, a bag filled

with helium gas at a pressure of 1 atm was inserted between RDC and SHT to reduce multiple scattering processes. Table 6 shows detector parameters for ESPRI.

RDC has a 436×436 mm^2 effective area. The covered range of proton scattering angle at 1 m from the target is 50°λ70° in the laboratory frame, corresponding to about 40°-70° in center of mass (CM) for the free p+α elastic scattering. RDCs are composed of 7 planes with layer configuration XY'XY'X'YX'. There are 32 wires per plane with 7 mm drift length. The 1st X layer of both RDCs was not utilized in the tracking algorithm, due to the noise problem. The typical value of position resolution is 0.5 mm (rms) in both X and Y for recoil protons [32]. The tracking efficiency of RDCs deduced from the experimetal results is above 90%. Details of tracking efficiency determination are given in the Section 3.4.

The plastic detectors is 4 mm thick, wrapped by 25 μm Al foil and 200 μm polyethylene sheet. Trigger signals were generated by plastic detectors which were coupled to two PMTs in up and down direction. Figure 27 shows the electronic circuit chart of the ESPRI system. If either left or right plastic was fired, a trigger signal would be sent to the DAQ system with logic $L(U \times D)||R(U \times D)$. More details can be found in section 2.10.

An array of NaI(Tl) scintillator placed behind the plastic scintillators were used for identifying protons and reconstructing total energy. The NaI(Tl) scintillators are 431.8 mm long, 45.72 mm wide, and 50.8 mm thick and could be able to detect the full energy of protons up to 100 MeV. On the other hand, the energy range of interest for the recoil protons is up to 150 MeV. Therefore, a wedge-shape degrader was placed in front of the RDC frame for slowing down the protons at the forward angle. The degrader was made of copper material and was placed vertically with a width of 236.5 mm and a thickness ranging from 2 to 30 mm, covering an angular region of 55°-62.5°. The angular straggling caused by the degrader was less than 55 mrad in sigma. More details can be found in the Section 3.4 about the reconstruction of proton full energy.

2.7 Cluster detection - Telescopes

Knocked-out α-clusters from $(p, p\alpha)$ reaction were measured using two telescopes placed at forward angle in a dedicated chamber built for the present experiment. Figure 28a shows a top view of two telescopes in the chamber. Each telescope

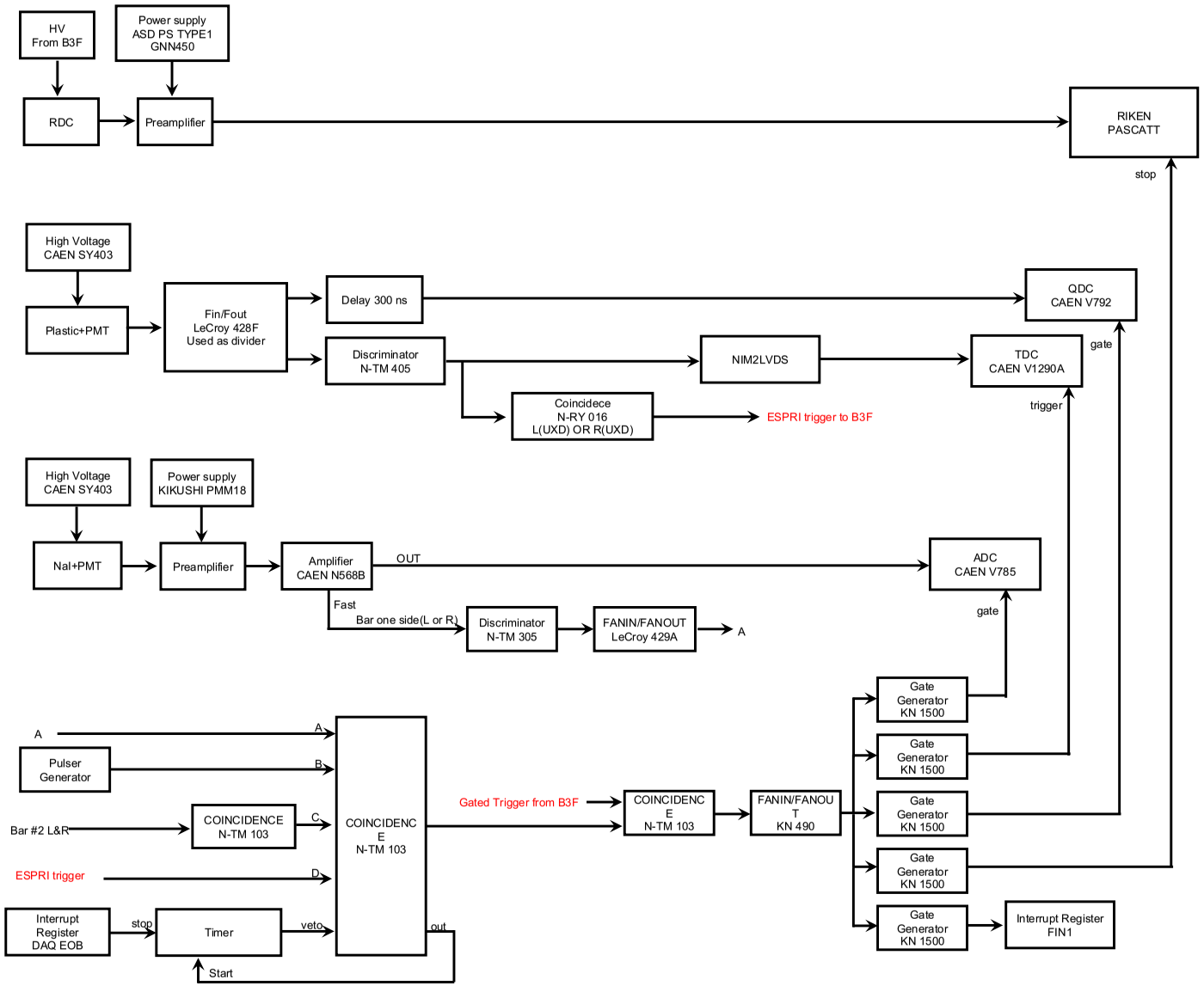

Figure 27 Circuit chart of ESPRI System

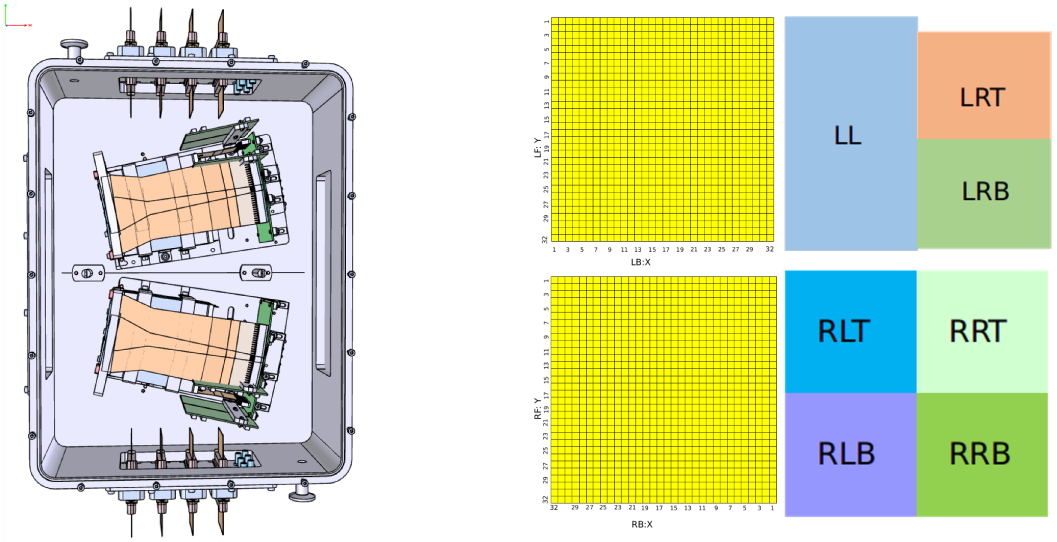

(a) Top view of chamber

(b) Detector configuration

Figure 28 Telescope setup and detector configuration in the chamber

Table 7 Telescope parameters

DSSD	Type	BB7 with kapton readout from Micron Semi. Ltd
	Pitch	2 mm
	Strips/Elements	32 × 32 (Junction + Ohmic Side)
	Active Area	64 × 64
	Thickness	1500 μm
CsI(Tl)	Left Array	2 (Type1) + 1 (Type2)
	Right Array	4 (Type1)
	Type1	32mm × 32 mm × 60 mm
	Type2	86.4mm × 61.2 mm × 50 mm

consists of a BB7 type **D**ouble-sided **S**trip **S**ilicon **D**etector (DSSD) from Micron Semiconductor Ltd [33] followed by CsI(Tl) scintillators for energy measurement of knocked-out clusters with projectile-like velocity. The DSSD has an active area of 64×64 mm^2 and 2 mm wide strips, covering an angular region of 4-14°. The front face of DSSD was about 35 cm away from the target. There were 2 types of CsI(Tl) modules (type1 is 60 mm long, type2 is 50 mm long). On the right side CsI(Tl) array consisted of 4 identical crystals of type1, while on the left side it consists of 2 crystals of type1 plus 1 large crystal of type2. Detectors of type 1 were from the FARCOS array [34] while the type 2 module came from the CHIMERA array [35]. Figure 28b shows the detector configurations in both telescopes. A 25 mm thick aluminum degrader was placed in front of DSSD so as to insure a sufficient energy range for the cluster detection. The calculated energy straggling of alpha with beam velocity in the degrader was about 0.4 MeV/nucleon, nearly three times smaller than the typical energy resolution of the modules.

Signals from the junction side of DSSD detectors were used to generate trigger for the telescope subsystem. Figure 29 shows the electronic circuits chart of the telescopes system. More details can be found in section 2.10

2.8 Residual particles detection

The ^{4,6,8}He residues produced in the $(p, p\alpha)$ reactions were measured by the SAMURAI spectrometer and its standard detectors, as Figure 15 shows. Forward drift Chamber 0(FDC0) mounted in front of the SAMURAI entrance window was used to measure the scattering angle of residues. Charged residues are deflected by the magnetic field after entering the SAMURAI magnet and subsequently go out through the exit window. Combined with FDC0, another forward drift Chamber 2(FDC2) placed right after the SAMURAI exit window was used to reconstruct the trajectories of the fragments for precise rigidity measurement. Particle identification of the residues was achieved by Hodoscope walls of plastic array placed perpendicular to the 60° line through ΔE-ToF technique.

2.8.1 Forward drift chamber:FDC0,FDC2

FDC0

FDC0 is located after the Telescopes chamber and before the entrance window of SAMURAI at a distance of about 80 cm from the target. FDC0 has a similar structure

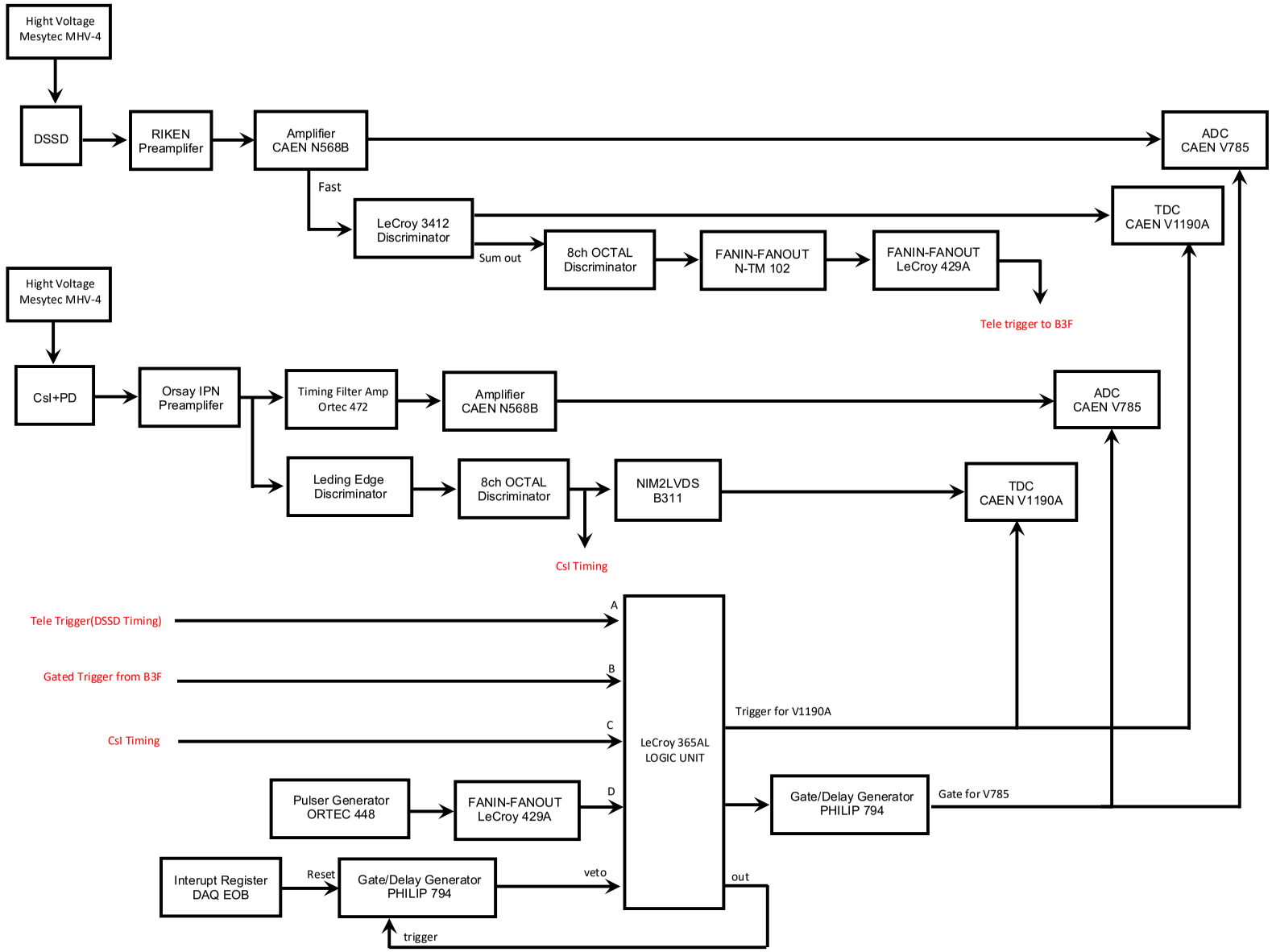

Figure 29 Circuit chart of Telescope System

and wire configuration of the planes as BDCs. The main difference is that FDC0 has an effective area of 160 × 160 mm^2(32 wires per layer) larger than that in the BDCs. High counting rate tolerance up to 500K has been achieved in FDC0 and BDCs with 5 mm wire spacing. The position is reconstructed with a resolution of 150 μm (rms) and an efficiency of 99% [29]. FDC0 gas pressure and voltage was set for optimized detection of He isotopes.

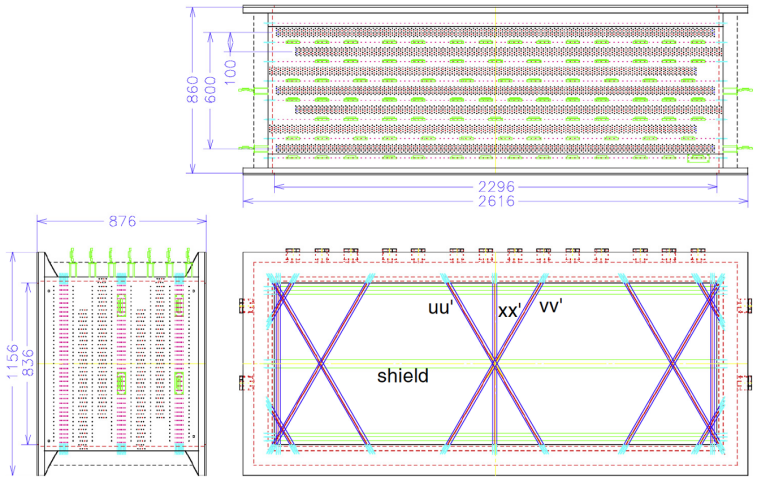

Figure 30 Schematic view of the FDC2 [29].

FDC2

Position information provided by FDC2 is the key factor for high precision rigidity analysis of the fragment. It is placed after the exit window of SAMURAI perpendicular to the 60° line refer to the beamline. The dimension of FDC2 is 2616(H)× 1156(V)× 876(T) mm^3 and is much larger compared to the previous BDCs or FDC0, in order to cover a large part of the SAMURAI downstream detection plane.

Figure 30 shows a schematic view of FDC2. It has 14 planes with 3 kinds of wire orientation xx'(0°),uu'(+30°),vv'(-30°) and each plane has 112 wires with 10 mm drift length. Two adjacent planes in the same orientation, such as xx', are assembled together and shifted by 5 mm, for the same purpose as in the case of the BDCs. The distance between two planes group, such as xx' and uu', is 100 mm with shield wires (**s** plane) in between. FDC2 parameters are presented in Table 8. FDC2 was turned off during ^{10}Be and ^{12}Be beam runs while turned on during ^{14}Be beam runs.

Table 8 FDC2 Parameters [29].

Drift length	10 mm (hexagonal)
Anode, field (shield) wire	ϕ40 μm Au-W/Re, ϕ80 μm/ Au-Al
Planes	14 sense planes and 8 shield planes
Layer angle	xx'(0°), uu'(+30°), vv'(-30°), s(90°)
Configuration	sxx'suu'svv'sxx'suu'svv'sxx's
Effective area	2.2m (H) × 0.8 m (V) × 0.8 m (D)
Readout	1568 ch (112 ch/plane × 14)
Field (shield) wires	4788(328)
Operating gas	He + 50%C_2H_6 at 1 atm
Gas, shield window	50 μm Mylar × 2, 12 μm Al-Mylar × 2
Thickness	L/Lr = 1.8×10^3

2.8.2 Hodoscopes - HODF,HODP

Hodoscopes for fragments(HODF) and for protons(HODP) are two sets of plastic scintillators array, placed vertically at around 5m downstream of SAMURAI magnet and parallel to its exit window. It was installed after FDC2 to measure the TOF and energy loss of fragments for particle identification. The position of the detectors has been optimized based on trajectory calculations as displayed in Figure 21 for the nucleus of interest.

Shown in Figure 31, the hodoscopes walls HODF and HODP consist of 24, 16 identical plastic scintillators, respectively. Each plastic scintillator has a size of 10(H) × 120(V) × 1(D) cm^3 with two PMTs(R7195 Assy) coupled at each end. In between HODF and HODP, there was a gap of about 20 cm. For ^{10,12}Be beam runs, most of the unreacted beam passed through this gap to avoid high counting rate in the hodoscopes.

2.9 Neutron detection - NEBULA

The neutron detector array NEBULA abbreviation for **Ne**utron-detection system for **B**reakup of **U**nstable Nuclei with **L**arge **A**cceptance consisted of two walls of plastic scintillators. NEBULA was designed to measure projectile-rapidity neutrons at 100–300 MeV with a large acceptance and high efficiency. It was placed downstream of the target in order to detect neutrons passing through the SAMURAI gap.

Figure 31 Hodoscopes in the experiment

Figure 32 shows a schematic view of NEBULA. There are 6 layers of plastic walls which are arranged into 2 groups. In each group, 2 layers(black) were for neutron detection(NEUT), and 1 layer(blue) is for rejection of charged particles(VETO). Each NEUT layer consisted of 30 modules of plastic scintillators for neutron detection; while each VETO layer consisted of 12 modules of plastic scintillators. The plastic scintillators standing vertically have two PMTs attached at both ends. Table 9 shows detailed parameters of NEBULA. It is placed around 11m from the target with an effective area 3.6(H) $\times$ 1.8(V) m^2, and then this makes the angular acceptance $\pm$8.8 ° horizontally and $\pm$4.4° vertically. The intrinsic detection efficiencies for 1 neutron and 2 neutrons are estimated to be 40%and 12% [29], For the purpose of the analysis presented in this thesis, data from NEBULA were not exploited.

2.10 Triggers and run summary

The RIBF Data Acquisition system(DAQ) [36] was implemented for the data acquisition of the present experiment. This DAQ system is based on a common trigger scheme. The logic signals received from different detector subsystems were combined as shown in Table 10. Beam trigger was defined by the coincidence of signals from SBT1 and SBT2 plastics, and used as time start. A downscaling factor of 1500 was used for DS Beam trigger events, recording total beam counts(cross-

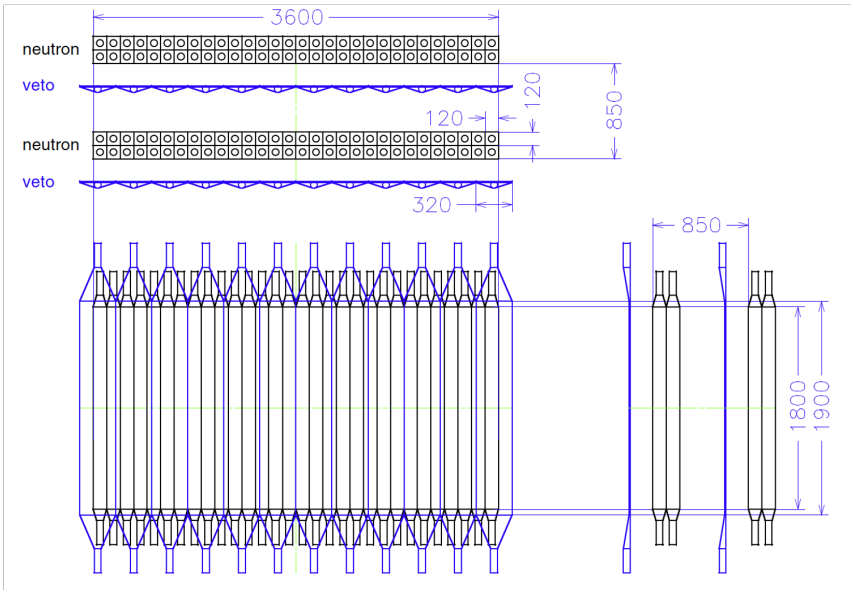

Figure 32 Schematic view of the NEBULA [29].The black and blue modules are for the neutron detectors and veto detectors, respectively

Table 9 NEBULA parameters [29]

Neutron detector	
Module BC408	12(H)×12(D)×180(V) cm^3
Configuration	30 modules/layer, 4 layers
Total thickness	48 cm
Efficiency	(1n)40%, (2n)12%
Veto detector	
Module BC408	32(H)×1(D)×190(V) cm^3
Configuration	12 modules/layer, 2 layers
Photomultiplier tubes	R7724 Assy×288

section normalization). The main physics trigger required SBTs(beam trigger), ESPRI(recoiled proton trigger), and Telescope(alpha trigger) in coincidence.

Table 10 Trigger list in the experiment

Subsystem	Signal	Trigger List
Beam	SBT	1. DS Beam(1500)
ESPRI	PMT L(U×D)||R(U×D)	2. Beam x ESPRI
Telescope	DSSD	3. Beam x Telescope
NEBULA	PMT U×D	4. Beam x NEBULA
Hodoscope	PMT U×D	5. Beam x Hodoscope
		6. Beam x ESPRI x Telescope

The exclusive measurement of the $(p, p\alpha)$ reaction on neutron-rich Beryllium isotopes at the energy of 150 MeV/u was carried out. Table 11 shows the run summary of the experiment. Three sets of data corresponding to 3 secondary beam setting, ^{10}Be,^{12}Be, and ^{14}Be beams were taken. The allocation of beam time was considered in order to achieve approximately the same amount of statistics. For ^{10}Be and ^{12}Be, the counting rate of the beam were restricted to 5×10^5 pps by reducing the momentum acceptance of BigRIPS, limited by the FDC0 which was tuned for the detection of Helium isotopes. FDC2 was turned off in these 2 settings. As for case of ^{14}Be beam, the maximum momentum acceptance of BigRIPS was applied and the SAMURAI magnetic field was tuned to avoid beam hitting on FDC2 and make sure to cover the region of interested alpha particles. The purity of the secondary beams was approximately 100% in all cases. A 6.5 hour empty target run with ^{14}Be beam was carried out for the estimation of the background events. Defocused alpha beams were used for energy calibration of telescopes. Details can be found in Section 3.6.

Table 11 Run Summary of S12 experiment

run type	Beam	Intensity (pps)	Duration (hr)	Conditions
Physics	^{10}Be	400k-500k	25	B = 2.1T, FDC2 off
Physics	^{12}Be	500k	25	B = 2.7T, FDC2 off
Physics	^{14}Be	200k-250k	76	B = 2.5T, FDC2 on
Empty Target	^{14}Be	200k-250k	6.5	B = 2.5T, FDC2 on
Calibration	^{4}He	500	1.8	Defocused beam,150 MeV/u
Calibration	^{4}He	500	1	Defocused beam,120 MeV/u

Chapter 3

Data analysis

This chapter describes the calibration process of the detectors used in the experiment. In order to extract the four-momentum vectors of both the secondary beam and fragments from the quasi-free $(p, p\alpha)$ reaction, channel numbers of raw-data will be calibrated into MeV for energy, ns for time, and mm for position. Section 3.1 gives beamline plastics analysis and provides the energy and PID of secondary beams. Section 3.2 presents the space-time conversion of drift chamber detectors and the tracking algorithm used for position reconstruction. The incident angle of the secondary beam and hit position on target is deduced based on the position information provided by drift chambers. Section 3.3 provides residue PID using ΔE-ToF method to distinguish and select different reaction channels. Section 3.4 is about the calibrations for recoil protons. Position calibration of RDC is similar to that of beamline drift chambers. The energy calibration of NaI(Tl) bars and time calibration of plastics is done with the energy information deduced from (p, p') scattering. Section 3.6 presents telescope calibration performed by using defocused alpha beams at two energies.

3.1 Beamline plastics analysis

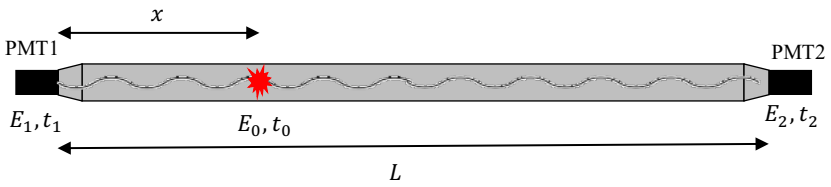

Figure 33 Scheme of a hit on plastic scintillator.

For plastic scintillators such as those used in the beam line, when a particle hits on detectors causing scintillation, as shown in Figure 33, the emitted light will travel and then be collected by PMTs coupled to both ends. The energy and timing information of the particle can be extracted from proper calibration. If we assume t_0 is the ToF of the particle at the hit position, then the time recorded by both PMT is t_0 plus the

travel time from hit position to PMT.

$$t_1 = t_0 + \frac{x}{v} \tag{10}$$

$$t_2 = t_0 + \frac{L-x}{v} \tag{11}$$

where v is the speed of light in the plastic materials. By combining Eq. 10 and Eq. 11, t_0 is solved as:

$$t_0 = \frac{t_1+t_2}{2} - \frac{L}{2v} \propto \frac{t_1+t_2}{2} \tag{12}$$

Since $\frac{L}{2v}$ is a constant, t_0 is proportional to the mean value of timing from both ends. The position dependency due to travel time of the light can be removed from such treatment.

Similarly, the charge signals of PMTs are also a position dependent function, which can be described as

$$E_1 = E_0 e^{-\lambda x} \tag{13}$$

$$E_2 = E_0 e^{-\lambda(L-x)} \tag{14}$$

where λ is the attenuation coefficient. E_0 can be solved by multiplying these formulae, given by

$$E_0 = \sqrt{\frac{E_1 E_2}{e^{-\lambda L}}} \tag{15}$$

Note that denominator $e^{-\lambda L}$ is also a constant. From Eq. 12 and Eq. 15, neither time nor energy loss from the measurement of plastic scintillator has position dependence.

On the other hand, position information of the hit can be deduced from the comparison of timing and energy signals. x position can be solved by combining t_1 and t_2 or E_1 divided by E_2,

$$x = \frac{v}{2}(t_1 - t_2) + \frac{L}{2} \tag{16}$$

$$x = -\frac{1}{2\lambda}(\lambda L - ln(\frac{E_1}{E_2})) \tag{17}$$

Based on the above considerations, plastic scintillators at F3, F7, and F13 are calibrated as described in the following. The time of each plastic refers to the average mean of calibrated time of PMTs at both ends. The energy loss ΔE deposited in plastics was used in the arbitrary unit using the geometric mean of ADCs from PMTs at both ends. The beam particles were identified by ToF-ΔE technique using plastic

scintillator at F7 and F13 described in Section 2.4.1. ToF of beam refers to the time difference between plastic scintillators placed at F7 and F13 focal plane. The offset value of absolute beam ToF was determined by the rigidity Bρ value of the dipole D6 in BigRIPS beamline shown in Figure 18.

3.1.1 Time calibration of plastic scintillators

The Time to Digital Converter (TDC) is an electronic module that digitalizes the time interval between two logic pulses as signals of time start and stop. As described in Chapter 2, the time start of DAQ system is the beam trigger generated from SBT1 and SBT2 at F13. Timing signals from PMTs of each plastic detector are used as time stop. The time in ns is obtained from TDC data by:

$$T_{cal} = \alpha T_{raw} + \beta \tag{18}$$

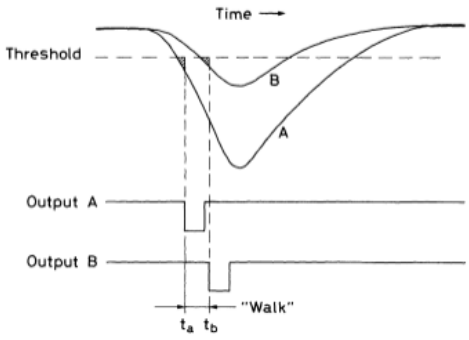

Figure 34 Time walk effect

Slew correction Due to the use of leading-edge discriminators, there is a magnitude-dependency of the timing signal, called slew effect or time walk effect. Figure 34 shows two simultaneous timing signals A and B. A walk of t_A and t_B determined by the threshold in the leading-edge discrimination is observed. To remove the time walk effect, a correction has been applied by using the following equation:

$$\Delta T_{walk} = p_0 + \frac{p_1}{\sqrt{Q}} \tag{19}$$

Figure 35 shows the dependency of time with respect to the charge signal of F7

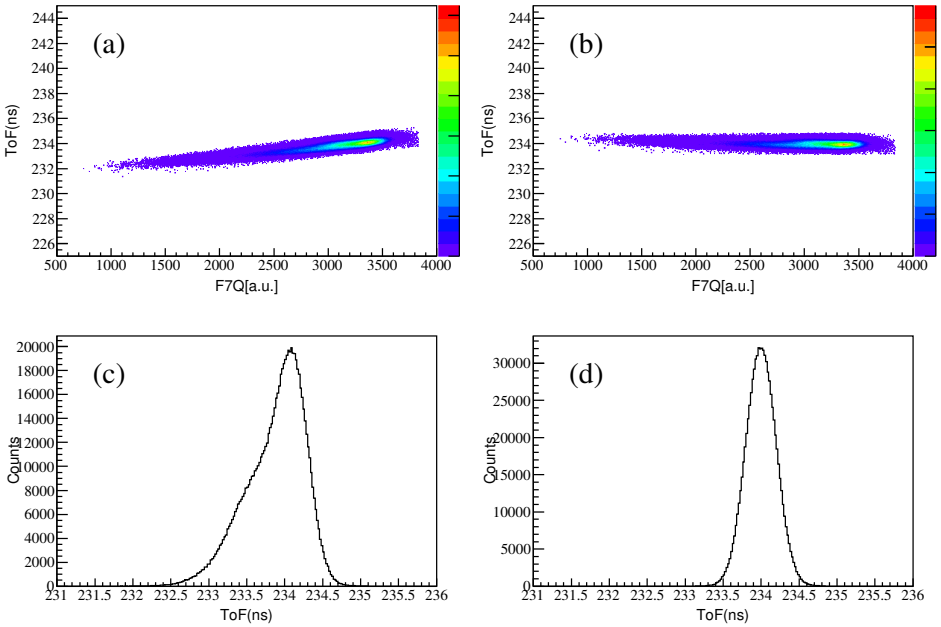

Figure 35 The dependency of ToF on the charge signal of F7 plastics (The data in the figure are from the case of ^{10}Be beam) (a) before correction; (b) after correction; (c) and (d) are the projected ToF distributions before and after correction, respectively.

plastics before and after time walk correction. An improvement of the resolution on ToF is clearly obtained.

Position dependency The timing signals of SBT1 and SBT2 were used for both time stop and beam trigger signals in the DAQ system. Referred to Eq. 16, the time difference ΔT is proportional to the hit position. A clear position dependency was found in the plastic detectors at F13 focal plane. Figure 36 shows the position dependence of SBT1 detector before and after the correction with linear equation. The time resolution of beamline plastics after the correction is estimated to be 165 ps in FWHM.

3.1.2 Time of flight(ToF) and Beam particle identification

The ToF of secondary beams is calculated by the time difference between the time signal of plastic at F7 and the average time signal of plastics(SBT1,SBT2) at F13, as described in the following equation.

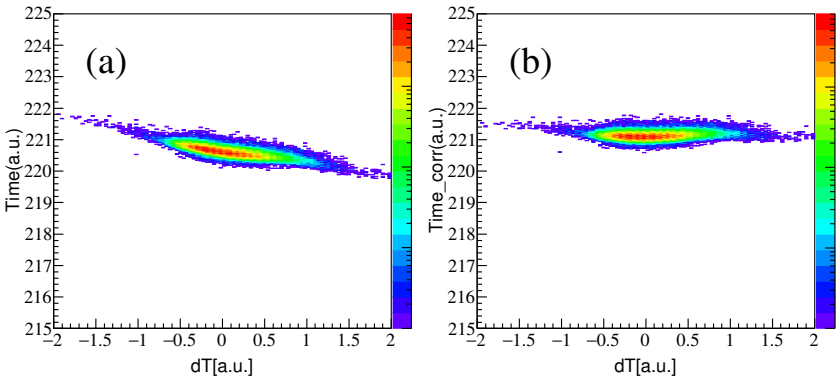

Figure 36 Position dependence of SBT1 detector before(a) and after(b) the correction

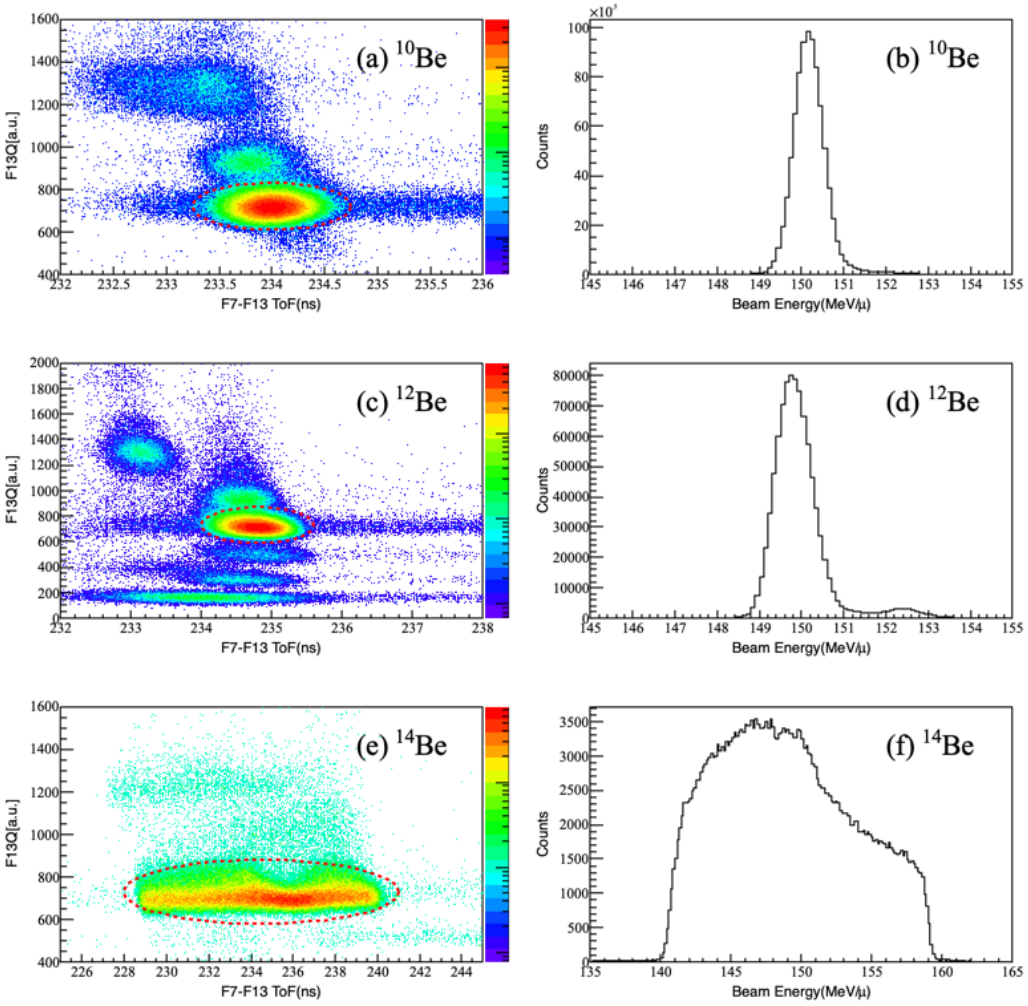

Figure 37 Particle identification and energy distribution of secondary beam

$$ToF_{F7-F13} = \frac{T_{SBT1} + T_{SBT2}}{2} - T_{F7} \tag{20}$$

The absolute offset of ToF is determined from the Bρ value of the last dipole D6 before plastic at F7. Beam energy can be derived from the calibrated ToF with the following equations:

$$B\rho = \frac{\gamma m v}{Z} \tag{21}$$

$$\beta = \frac{v}{c} = \frac{FL_{F7-F13}}{ToF_{F7-F13}c} \tag{22}$$

$$\gamma = \frac{1}{\sqrt{1-\beta^2}} \tag{23}$$

Figure 37 shows particle identification and energy distribution of the three secondary beams. Beryllium isotopes marked with red dashed circle in the PID plots are identified by ΔE-ToF method and well separated from other contaminants. The reason why the shape of ^{14}Be beam is so different is that momentum acceptance for ^{14}Be beam is wider. The purity of ^{10,12,14}Be secondary beam are all above 90% with the intensity of approximately 500 kHz for ^{10,12}Be, 200 kHz for ^{14}Be, respectively. The kinetic energy of beam particles at target is calculated taking into account the total energy loss in the materials from the D6 to the middle of SHT using the Lise++ code [37], assuming reactions take place in the middle of the target. The beam energies of the ^{10,12,14}Be beams are around 150 MeV/u with a momentum acceptance of ±0.5% for $^{10,12}Be$ and ±3% for ^{14}Be, respectively.

3.2 Drift chamber analysis

In this experiment, the trajectory of beam particles is reconstructed by drift chambers. The positions of beam particles passing through each drift chamber detector can be reconstructed by calibrating the drift time of ionized gas and using tracking algorithm. The trajectories and beam profile on target are calculated from the positions at the center of BDC1 and BDC2 by extrapolation. Similar process also has been applied to the calibration of FDC0 which was used to measure the scattering angle of residue particles. In this section, calibration of the drift chamber, trajectory reconstruction, and detection efficiency will be discussed.

3.2.1 DC calibration

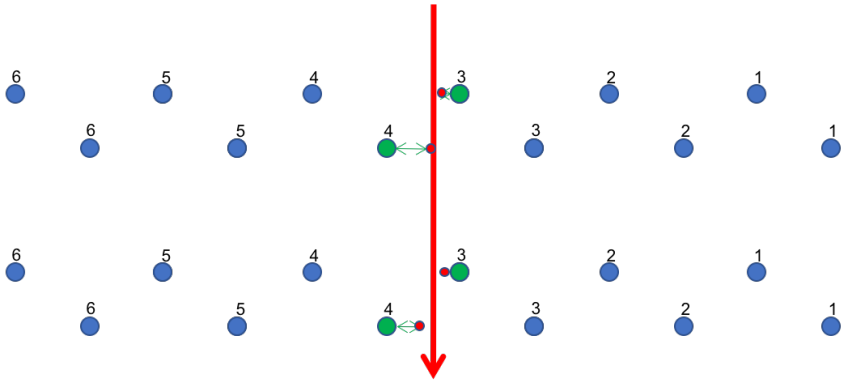

Figure 38 Scheme of tracking process

The hit position of charged particles passing through the gas filled in the DC is measured by the drift time of electrons caused by ionization. The calibration process is to convert drift time into drift length which is called Space-Time Conversion(STC). Figure 38 shows a simplified scheme of wire position in the DC. The pitch d is the maximum drift length. The spacing between 2 adjacent anode wires is 2d and the adjacent layers with the same orientation are shifted by 1d distance. Detailed description of the DC structure can be found in Section 2.4.2. For each DC along the beamline, a uniform distribution in the range of [0,d] is assumed for the possible hit position of the beam particles. Based on this assumption, an STC function[38] described below has been applied for converting drift time into drift length.

$$\frac{L(t)}{d} = \frac{\int_{t_{\min}}^{t} f(t)}{\int_{t_{\min}}^{t_{\max}} f(t)} \tag{24}$$

where t is the raw TDC of drift time and $f(t)$ is the TDC distribution. Figure 39(a) shows a typical example of TDC distribution from BDC1, from which the STC curve can be obtained by applying Eq. 24 to the TDC distribution, as shown in Figure 39(b).

3.2.2 Tracking analysis and position resolution

As noted in Chapter 2, BDC1, BDC2, and FDC0 have the same layer configuration, 4 layers in x and another 4 layers in y direction. The hit position $x_{hit}(x_i/y_i, z_i)$ in each layer can be obtained by combining the wire position and drift length calibrated

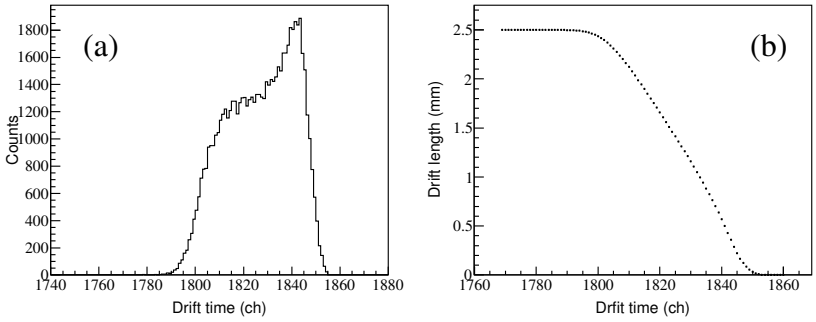

Figure 39 (a) TDC distribution of BDC1; (b) STC curve

by STC process. Ideally, only one wire is fired in each layer for a single event. Figure 38 shows an example of tracking. To obtain the trajectory of beam particle, the least-square fitting method has been utilized for fitting the hit positions from 4 layers in the *xoz* and *yoz* planes. The actual situation is that there are lots of multihit events with more than one wire fired at the same time. The most possible track is the one corresponding to the minimum χ^2 of the fitting. A position x_{track} in each layer can be deduced from each possible tracking fit. The difference $dx = x_{track} - x_{hit}$ is defined as fit residue. Assuming that particles passing through DC always go straight without angular straggling, the trajectory can be reconstructed with the χ^2 defined as follows. The quality of the reconstructed trajectory can be estimated from the following equation:

$$\chi^2 = \sum (\mathrm{d}x)^2 = \sum \left(x_{\mathrm{track}} - x_{\mathrm{hit}} \right)^2 \tag{25}$$

Figure 40 shows the residue distributions of BDC1, BDC2, and FDC0. Since these three DCs have the same pitch 5 mm and layer structures, the residue distributions are similar as expected. The typical σ of residue distribution is about 150 μm. The width of the residue distribution gives the quality of the least square fitting and can be used to estimate the position resolution. Section 3.2.5 presents another estimation of position resolution by using the relative position of the beamline DCs.

3.2.3 Detection efficiency

The definition of the detection efficiency of the drift chamber is

$$\eta_{\mathrm{dc}} = N_{\mathrm{dc}} / N_{\mathrm{ref}} \tag{26}$$

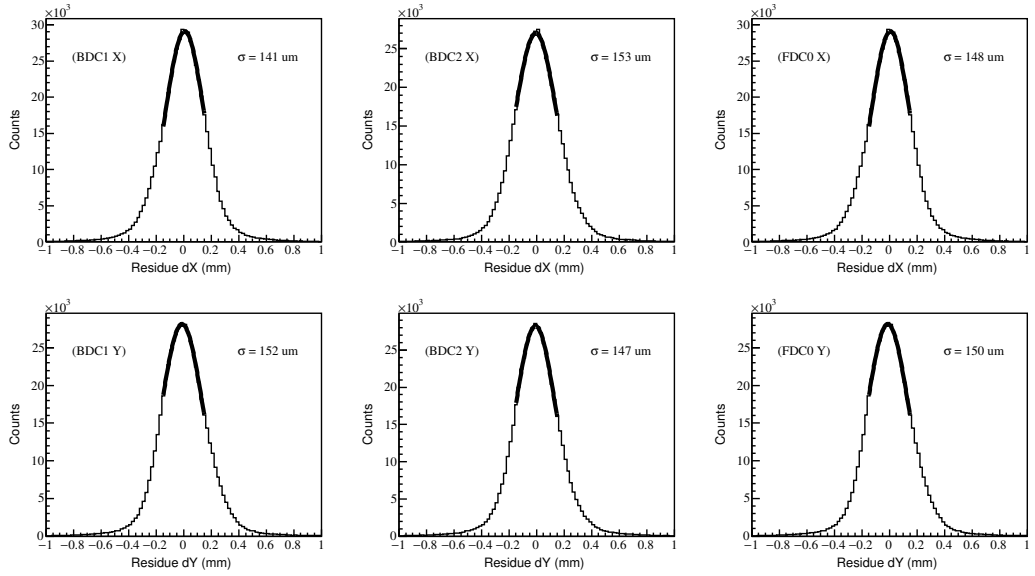

Figure 40 Residue distributions for BDC1, BDC2 and FDC0

where N_{ref} is the number of events selected from beam PID in a reference drift chamber. N_{dc} represents the number of effective events in the tested drift chamber. It was required that 3 or 4 layers at least are hit in either x or y direction in the tracking analysis. Table 12 gives a summary of detection efficiency for BDC1, BDC2, and FDC0. The detection efficiency is generally above 99%, even with a beam intensity up to 500k kHz, regardless of Z = 4 or Z = 2.

3.2.4 Beam profile and scattering angle of residue

Position detectors BDC1, BDC2, and FDC0 were placed before and after SHT to calculate the reaction vertex and scattering angle of fragments from the reaction. The beam profile composed of position (X_{tgt}, Y_{tgt}) and incident angle (θ_x, θ_y) in the middle of the target is obtained by linear extrapolation from the measured position in BDC1 and BDC2 with the following equation:

$$\tan\theta_{\mathrm{x}} = \frac{X_{\mathrm{BDC2}} - X_{\mathrm{BDC1}}}{Z_{\mathrm{BDC2}} - Z_{\mathrm{BDC1}}} \tag{27}$$

$$\tan\theta_{\mathrm{y}} = \frac{Y_{\mathrm{BDC2}} - Y_{\mathrm{BDCl}}}{Z_{\mathrm{BDC2}} - Z_{\mathrm{BDCl}}} \tag{28}$$

$$X_{\mathrm{tgt}} = X_{\mathrm{BDC2}} + \left(Z_{\mathrm{tgt}} - Z_{\mathrm{BDC2}}\right)\tan\theta_{\mathrm{x}} \tag{29}$$

$$Y_{\mathrm{tgt}} = Y_{\mathrm{BDC2}} + \left(Z_{\mathrm{tgt}} - Z_{\mathrm{BDC2}}\right)\tan\theta_{\mathrm{y}} \tag{30}$$

Table 12 Detection efficiency of drift chambers

Beam Run	Detector	Detection efficiency
^{10}Be	BDC1	99.9%
	BDC2	99.7%
	FDC0	99.4%
^{12}Be	BDC1	99.9%
	BDC2	99.8%
	FDC0	99.4%
^{14}Be	BDC1	99.9%
	BDC2	99.9%
	FDC0	99.5%
^{4}He	BDC1	99.8%
	BDC2	99.9%
	FDC0	99.5%

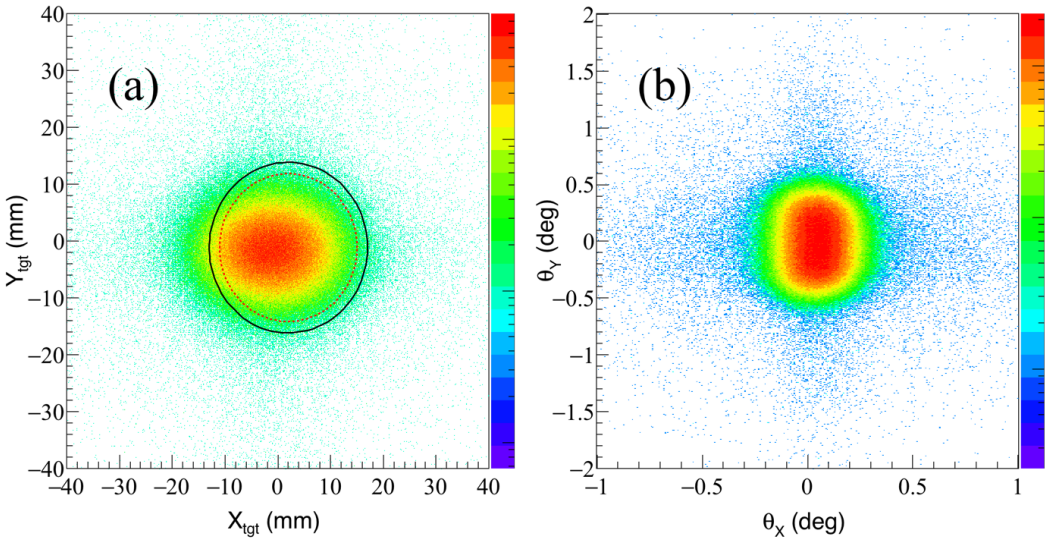

Figure 41 ^{10}Be beam profile in the middle of the target

Figure 41 shows the beam profile at the middle of the target. The black solid curve in Figure 41(a) indicates the edge of SHT with 15 mm radius. The size of the beam spot is smaller in the case of ^{10}Be and ^{12}Be beams, compared to ^{14}Be beam. The red dashed curve with 13 mm radius is used as the cut on target in the data analysis. Above 90% of effective events are inside the cut. The characteristics of three beam spots are listed in Table 13

Table 13 Characteristics of three beam spots

Beam	σ_x (mm)	σ_y (mm)	$\sigma(\theta_x)$ (deg)	$\sigma(\theta_y)$ (deg)
^{10}Be	6.8	5.1	0.10	0.25
^{12}Be	7.0	4.5	0.18	0.50
^{14}Be	8.0	10.5	0.24	0.31

Combining the positions provided by BDC1, BDC2 and FDC0, the scattering angle of the residues can be calculated from the following equation:

$$\vec{V}_{\text{beam}} = \vec{V}_{\text{BDC2}} - \vec{V}_{\text{BDC1}} \tag{31}$$

$$\vec{V}_{\text{res}} = \vec{V}_{\text{FDC0}} - \vec{V}_{\text{tgt}} \tag{32}$$

$$\cos\left(\theta_{\text{res}}\right) = \frac{\vec{V}_{\text{beam}} \cdot \vec{V}_{\text{res}}}{\left|\vec{V}_{\text{beam}}\right|\left|\vec{V}_{\text{res}}\right|} \tag{33}$$

3.2.5 Position resolution

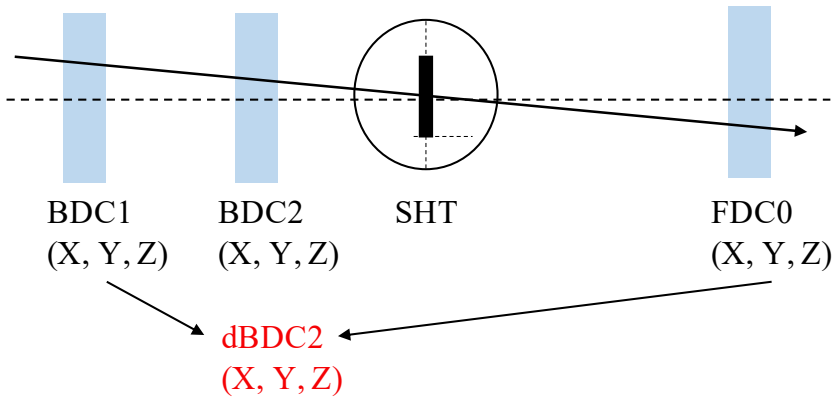

Figure 42 Scheme of relative positions of drift chambers

Figure 42 shows a schematic view of the relative positions of BDC1, BDC2 and FDC0. 3D positions (x,y,z) of two DCs can be used to deduce the third one,

for example, the position of BDC2 can be deduced from the interpolation between positions of BDC1 and FDC0. The unreacted beam particles can be selected by the downscaled beam trigger, and be assumed that particles pass through 3 DCs straight along the beamline with limited angular straggling. The difference between the calibrated position and deduced position of BDC2 can be used to estimate the position resolution. From Figure 40, position resolution σ_{dc} is assumed to the same for all the DCs. Let's take the x direction as an example.

$$X_{\mathrm{dBDC2}} = X_{BDC1} + \frac{Z_{dBDC2} - Z_{BDC1}}{Z_{FDC0} - Z_{BDC1}} \left(X_{FDC0} - X_{BDC1} \right) \tag{34}$$

If we define the constant $C_0 = \frac{Z_{dBDC2} - Z_{BDC1}}{Z_{FDC0} - Z_{BDC1}}$, then Eq. 34 can rewritten as:

$$\mathrm{X_{dBDC2}} - \mathrm{X_{BDC2}} = \left(1 - C_0\right) X_{BDC1} + C_0 X_{FDC0} - X_{BDC2} \tag{35}$$

Position resolution σ can be calculated from error propagation of Eq. 35:

$$\sigma^2 \left(dX_{\mathrm{BDC2}} \right) = \left(1 - C_0\right)^2 \sigma^2 \left(X_{BDC1} \right) + C_0^2 \sigma^2 \left(X_{FDC0} \right) + (-1)^2 \sigma^2 \left(X_{BDC2} \right) \tag{36}$$

Assuming BDC1, BDC2 and FDC0 have the same position resolution σ_{DC}, we have

$$\sigma_{DC} = \sigma \left(\mathrm{dX_{BDC2}} \right) / \sqrt{\left(1 - C_0\right)^2 + C_0^2} \tag{37}$$

Figure 43 shows the distribution of the difference between the BDC2 position from interpolation of BDC1 and FDC0 and the measured positions in BDC2. Applying the Eq. 37, the position resolution in σ is estimated below 400 um for all the DCs. Note that FDC0 was tuned for Z = 2 residues, unlike the BDCs which were tuned for Z = 4 beam particles. Another drawback of this estimation is that it doesn't take into account the angular straggling of materials between the DCs for the estimation of position resolution.

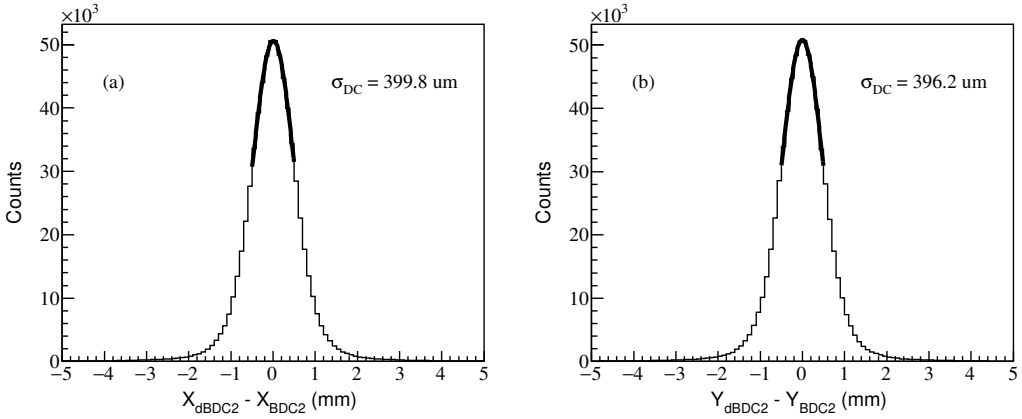

Figure 43 Difference distribution of the BDC2 position: (a) $X_{dBDC2} - X_{BDC2}$;(b) $Y_{dBDC2} - Y_{BDC2}$

3.3 Hodoscope analysis

The hodoscope wall consists of 2 arrays of plastic scintillators: HODF and HODP, placed downstream the exit window of the SAMURAI. The above time and energy deposit ΔE analysis procedures used for beamline plastic also applied for the plastics in Hodoscope. The PID from the hodoscope will be used for selecting $(p, p\alpha)$ reaction channels, and reduce background. In this section, the quality of fragments separation in the PID is checked.

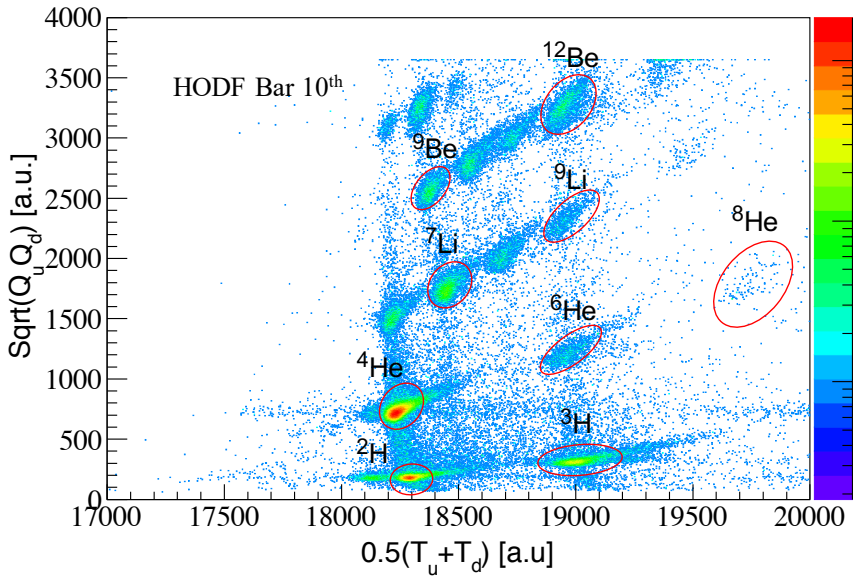

Figure 44 Particle identification on HODF plastic scintillator(Bar 10^{th})

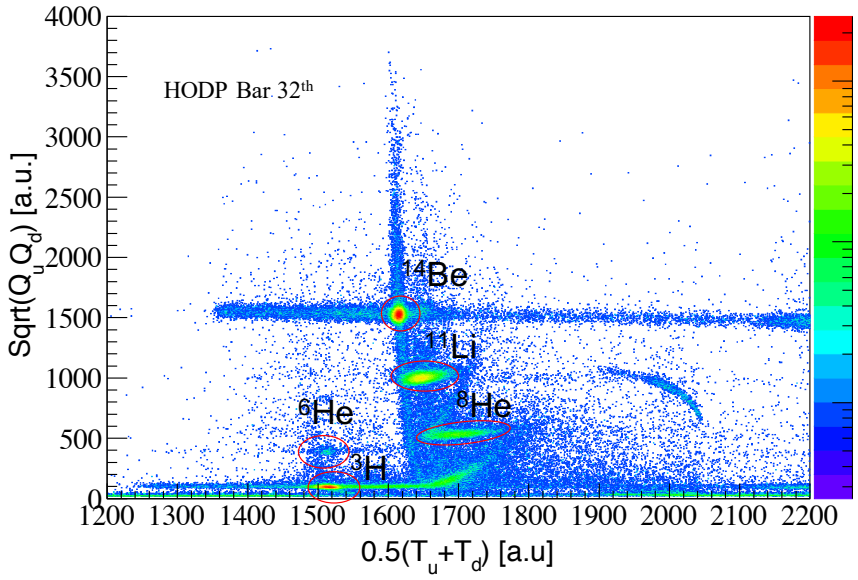

Figure 45 Particle identification on HODP plastic scintillator(Bar 32^{th})

3.3.1 Particle identification

Figure 44 and Figure 45 shows PID plots for bar 10^{th} in HODF and bar 32^{th} in HODP. T_u and T_d are the time signals, and Q_u and Q_d are the charge signals from the top and bottom PMT. The events used in the plots come from ^{14}Be beam setting. The Beryllium isotopes and Helium isotopes are well separated by the ΔE-ToF method The events from different reaction channels can be selected by setting the cut for different fragments like the red circles in the PID plot.

3.4 ESPRI analysis

The recoil protons are detected by the ESPRI setup, allowing to reconstruct their four-momentum vector. The scattering angle of protons is determined from the relative hit position of the target and RDCs. With the help of the PGS measurement, the 3D position and direction of protons can be calculated from the 2D position of the calibrated RDC. The energy of proton can be obtained in two ways: energy deposit in the NaI(Tl) bars and ToF measurement with the plastic detector. The punchthrough energy of protons in the 4 mm plastic is 24 MeV. In the present study, proton energies of interest are high enough so that a better energy resolution is obtained from the NaI bars (about 1.3%).

3.4.1 RDC position calibration

As with the beamline drift chambers, the position calibration of RDC is done by converting the drift time into drift length(STC). A major difference is that the uniform drift length distribution assumption in the drift cell doesn't hold for RDC, because the scattering angle of proton relates with physics of reaction channels. The space time conversion function used for RDC is a high order polynomial function determined in previous experiments.

$$\text{Drift Length} = p_1\sqrt{\text{TDC}} + p_2\text{TDC} + p_3\text{TDC}^2 + p_4\text{TDC}^3 + p_5\text{TDC}^4 \qquad (38)$$

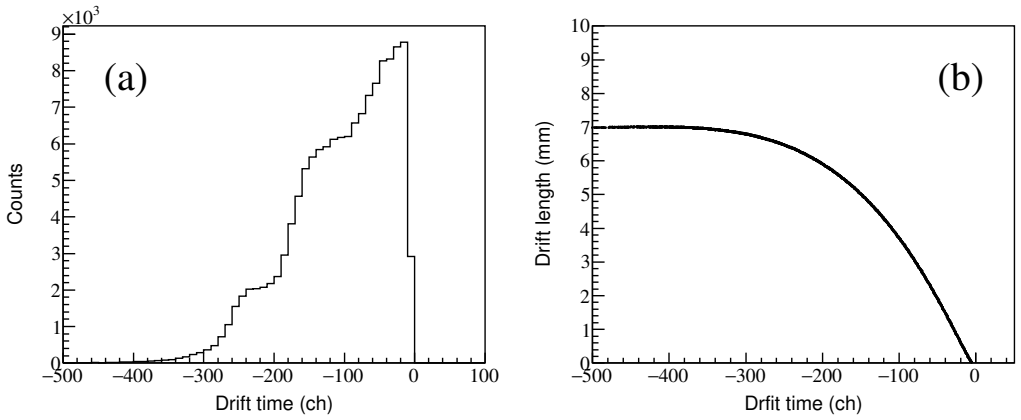

Figure 46 (a) TDC distribution of Recoil Drift Chamber(RDC); (b) Space time conversion for RDC

Figure 46 shows a typical TDC distribution of RDC and the curve for space time conversion. Note that the drift length is 7 mm. Tracking algorithm is the same as described in analysis for beamline DCs. The calibrated position of the best track with minimum χ^2 take the center of RDC as the reference. Based on the PGS measurement, the geometrical transformation of RDC is needed to calculate the direction and scattering angle of recoil protons.

Figure 47 shows the residue distribution of RDC in the x and y direction. The sigma of the residue distribution is around 100 um with longer tails for both direction. The detection efficiency of RDCs is derived by calculating the proportion of the effective RDC positions in the total number of protons from ΔE-E PID. Table 14 lists the estimated detection efficiency of both RDCs.

The trajectories of the recoil proton are derived from the positions of the RDC

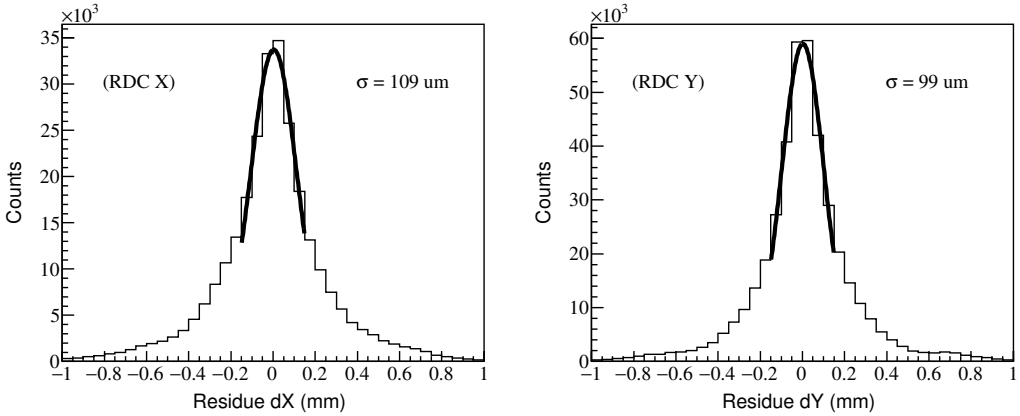

Figure 47 Residue distribution of RDC in (a) X and (b) Y direction

Table 14 Detection efficiency of RDCs

RDC	Detection efficiency(%)
Left	90.6
Right	96.1

and target. Combining Eq. 33, the scattering angle of the protons can be deduced from the following equation:

$$\vec{V}_{\mathrm{p}} = \vec{V}_{\mathrm{RDC}} - \vec{V}_{\mathrm{tgt}} \tag{39}$$

$$\cos\left(\theta_{\mathrm{p}}\right) = \frac{\vec{V}_{\mathrm{beam}} \cdot \vec{V}_{\mathrm{p}}}{\left|\vec{V}_{\mathrm{beam}}\right|\left|\vec{V}_{\mathrm{p}}\right|} \tag{40}$$

3.4.2 NaI(Tl) energy calibration and proton energy reconstruction

To calibrate the NaI(Tl) bars and extract recoil proton energies, events from (p, p') scattering have been used, taking advantage of two body kinematical correlations. Figure 48a shows the kinematic relation between energy and scattering angle of recoil protons in the $^{10}\mathrm{Be}(p, p')^{10}\mathrm{Be}$ reaction for several excitation energies. Figure 48b displays the energy sharing in the 4 mm plastic and NaI bars detectors based on the curve of elastic scattering.

The calibration procedures of NaI bars is divided into four steps:

1. Calculate energy deposit in the NaI for different scattering angles, as shown in

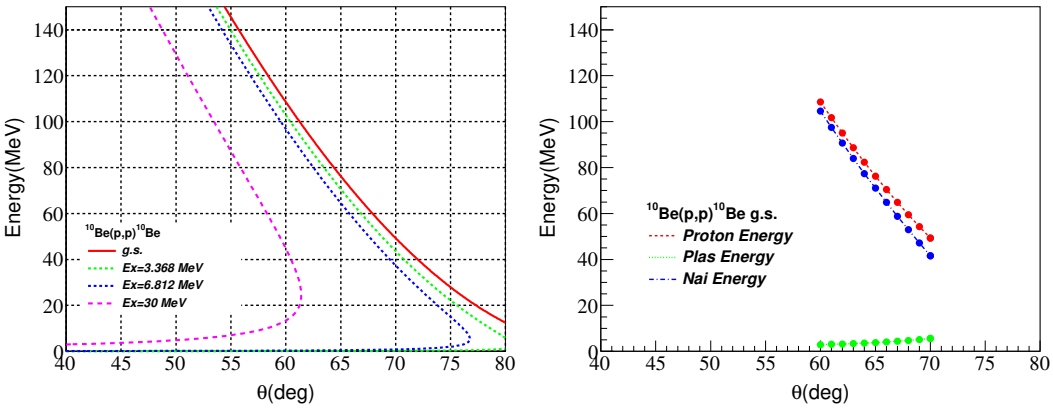

(a) Proton energy vs θ (b) Detectors energy vs proton θ

Figure 48 ^{10}Be$(p,p')^{10}$Be scattering theoretical curve

Figure 48b;

2. By selecting (p,p') scattering events, extract the ADC values of NaI under the corresponding scattering angles; Note that ADC discussed here have taken into account the pedestal subtraction.

3. Calibrate the ADC values into energy in unit of MeV with Eq. 41;

4. Reconstruct the energy of the recoil protons taking into account energy losses in the materials crossed by the protons;

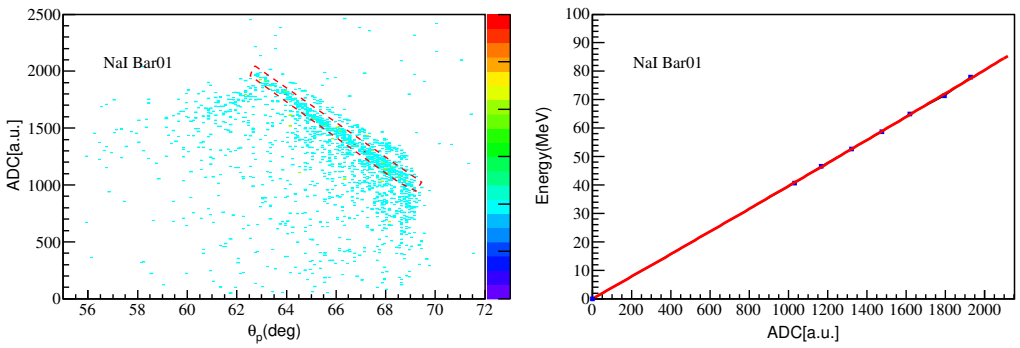

Figure 49 (a) ADC vs θ angle of NaI bar 01^{th}; (b) Fitting the relation between ADC and Energy

We now illustrate the procedure using ^{10}Be(p,p') data. Figure 49a shows a 2D plot of ADC vs θ_p from NaI bar 01^{st} by selecting events from (p,p') scattering. Two clear well separated lines are observed. The upper band comes from elastic scattering, corresponding to the ground state of ^{10}Be. The lower band comes from the inelastic

scattering to the first 2^+ excited state. Since the ESPRI detectors were placed at the large scattering angle, a higher count rate is observed for populating 2^+ state than for the ground state. In principle, there is no difference in choosing which state for the energy calibration of NaI(Tl) bars. Therefore, events from the first excited state have been selected to take advantage of the higher statistics.

The raw ADC values are extracted by considering seven bins in angles, corresponding to the seven points in Figure 49b. The Birks formula [39] is utilized to calibrate the energy of NaI bars:

$$E_{NaI} = \frac{\alpha ADC}{1 + \beta ADC} \tag{41}$$

where the parameters α and β are fitted from the process in Figure 49b. The 14 bars of NaI(Tl) have been calibrated, individually. Due to the influence of the magnetic field of SAMURAI on the PMT coupled to NaI(Tl) crystals, NaI(Tl) bars had to be calibrated independently for all three beam settings.

Finally, to reconstruct the total energy of protons, the measured energy loss in plastic were not considered, due to their resolution of about 10%. Energy loss calculated with the LISE++ code were used instead.

3.4.3 Plastic time calibration

The time calibration of plastic detector can take advantage of the energy calibration of NaI bars and position calibration of RDC. The proton energy reconstructed from the energy of NaI detectors can be used as reference energy for time calibration. The relation between ToF and total energy of proton is:

$$\beta = \frac{L}{cToF_p} \tag{42}$$

$$\gamma = \sqrt{\frac{1}{1-\beta^2}} \tag{43}$$

$$T_p = (\gamma - 1) M_p \tag{44}$$

where L refers to flight length of recoil proton between target and plastic detector. L can be calculated from the position of RDC and relative position between RDC and plastic. With the known kinetic energy of protons, ToF can be calculated as the reference time for calibration. The following equation is used for calibrating the ToF.

$$ToF_p = \alpha TDC + \beta + T_{pos} + T_{slew} \tag{45}$$

where $\alpha = 0.025$ ns/ch which is a constant obtained from the MultiHit TDC (CAEN1290A) documentation. β is the offset determined from the energy of proton. T_{pos} is the correction for position dependency, and T_{slew} is the correction for time walk effect.

Position correction The time of plastic has a strong position dependency on vertical positions. Because of a data acquisition problem, only raw time data of PMT from one end of plastic detector was recorded, position dependency is needed and corrected by the following equation:

$$\Delta T = ToF_p - (\alpha TDC + \beta + kY_{rdc} + b) \tag{46}$$

where ToF_p refers to the ToF deduced from the NaI calibration. $kY_{rdc} + b$ is the term for position correction. Figure 50a shows a linear position dependency between ΔT and Y_{rdc}. The segmentation in Figure 50a is caused by the gaps between NaI bars. Parameters of k and b are extracted from the linear fit of the 2D plot. Figure 50b illustrates the significant improvement of ΔT distribution after applying the position correction.

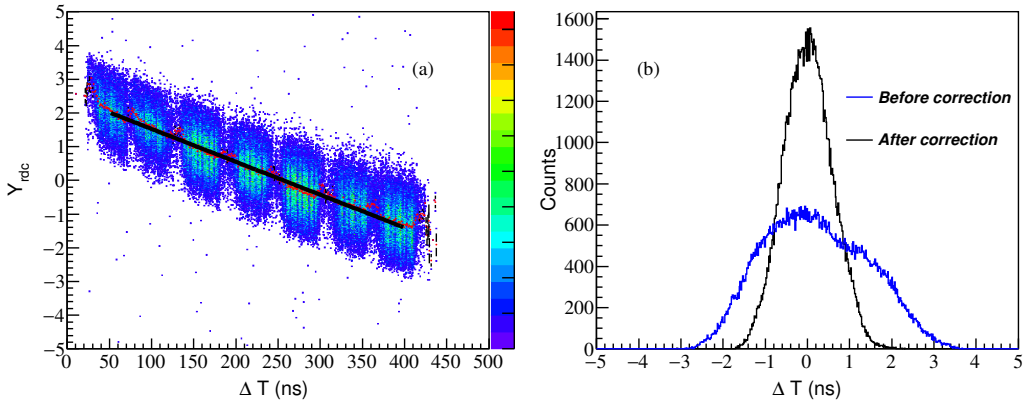

Figure 50 Position dependency correction of recoil particles' ToF

Time walk correction Figure 51a shows a time walk effect for protons with energy lower than 35 MeV. A similar correction procedure as in Section 3.2 has been taken for correcting this effect. This effect is less important compared to the position dependency in the proton energy range considered. Figure 51 shows the comparison before and after the correction.

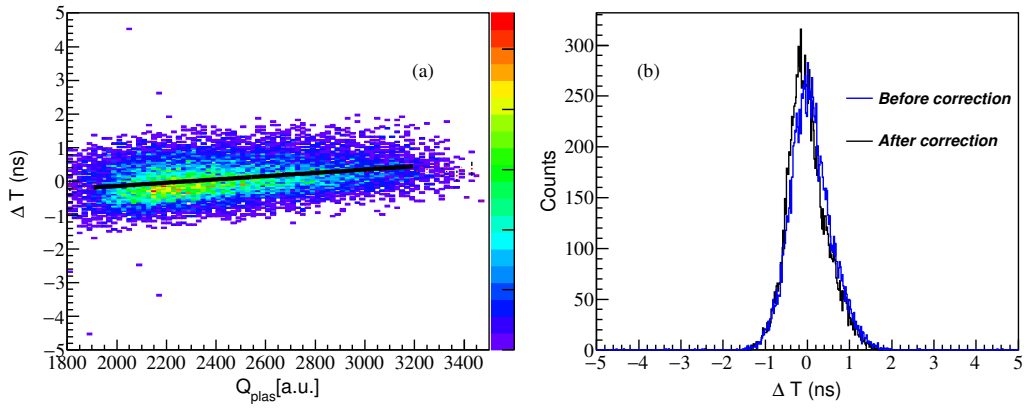

Figure 51 Slew effect correction of recoil particles' ToF

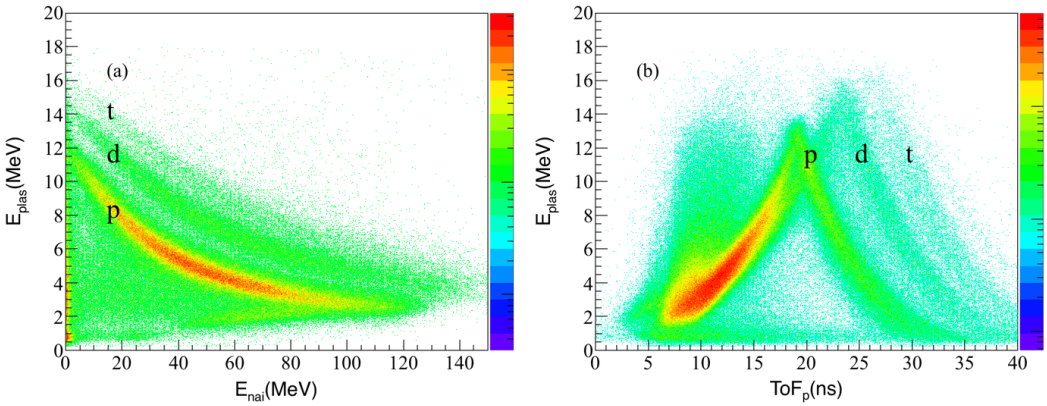

Figure 52 Particle identification of ESPRI setup (a) ΔE-E Method; (b) ΔE-ToF method

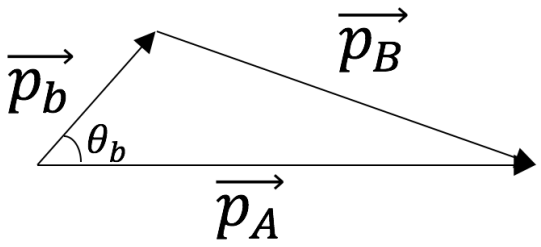

Figure 53 Momentum conservation between p_A,p_b and p_B

Particle identification Figure 52 shows particle identification of the ESPRI setup. Three locus corresponding to proton, deuteron, and triton, respectively, are observed in both plots. The bands of proton, deuteron, triton are well separated at the low proton energy region beyond the punchthrough ToF(about 20 ns). Therefore, the proton can be selected satisfactorily from these two PID plots over a broad energy range.

3.5 (p, p') scattering

In the present section, we make use of the elastic and inelastic reaction channel to check the calibrations of ESPRI described above (except for the ToF calibration). For the two-body reaction $A + a \rightarrow B + b$, where a and b are protons. The four-momentum vectors are written as:

$$P_A = \begin{pmatrix} T_A + m_A \\ \overrightarrow{p_A} \end{pmatrix}, P_a = \begin{pmatrix} m_a \\ 0 \end{pmatrix}, P_b = \begin{pmatrix} E_b \\ \overrightarrow{p_b} \end{pmatrix}, P_B = \begin{pmatrix} E_B \\ \overrightarrow{p_B} \end{pmatrix} \tag{47}$$

According to momentum conservation, $\overrightarrow{p_A} = \overrightarrow{p_b} + \overrightarrow{p_B}$, shown in Figures 53. The momentum of A, b, and B can be written as:

$$p_A = \sqrt{T_A^2 + 2T_A m_A} \tag{48}$$

$$p_b = \sqrt{T_b^2 + 2T_b m_b} \tag{49}$$

$$p_B = \sqrt{p_A^2 + p_b^2 - 2p_A p_b cos\theta_b} \tag{50}$$

The total energy and mass of B can be calculated from the law of energy conservation:

$$E_B = T_A + m_A + m_a - (T_b + m_b) \tag{51}$$

$$m_B = \sqrt{E_B^2 - p_B^2} \tag{52}$$

The excitation energy E_{Bex} of nucleus B is defined as follows:

$$E_{Bex} = m_B - m_{Bgs} \tag{53}$$

where m_{Bgs} is the rest mass of B.

From Eq. 50, the polar angle of protons is:

$$\theta_b = \arcsin(\frac{p_B}{p_b}\sin\theta_B) \tag{54}$$

Two-body reactions take place in a plane defined by momentum vectors before and after the reaction. In the following we also make use of this property.

3.5.1 Angular correlation

Several gates have been applied to filter events from (p, p') scattering channel: Trigger Beam×ESPRI, Beam PID, and target area selection, as well as a coplanarity gate and angle correlation gate.

Coplanarity gate The azimuthal angles φ_p and φ_{Be} are obtained from the reconstructed trajectories of particles detected by the RDCs and FDC0 in Section 3.2 and 3.4, using the horizontal plane as a reference. Figure 54 shows the correlation in ϕ azimuthal angles of proton and scattered ion B for the three beams. As expected, the $\Delta\varphi = \varphi_p - \varphi_{Be}$ distributions are centered at 180 ° with width σ = 2-3.5 °. Table 15 gives a coplanarity condition summary of $\Delta\varphi$ in the (p, p') scattering channels. Events from the left-side of ESPRI exhibit smaller distribution, possibly because the

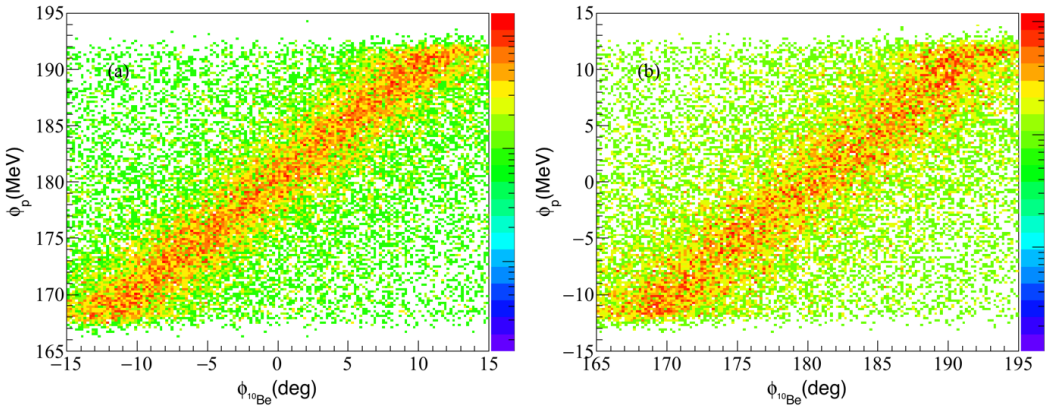

(a) ^{10}Be beam (a) Left ESPRI; (b) Right ESPRI

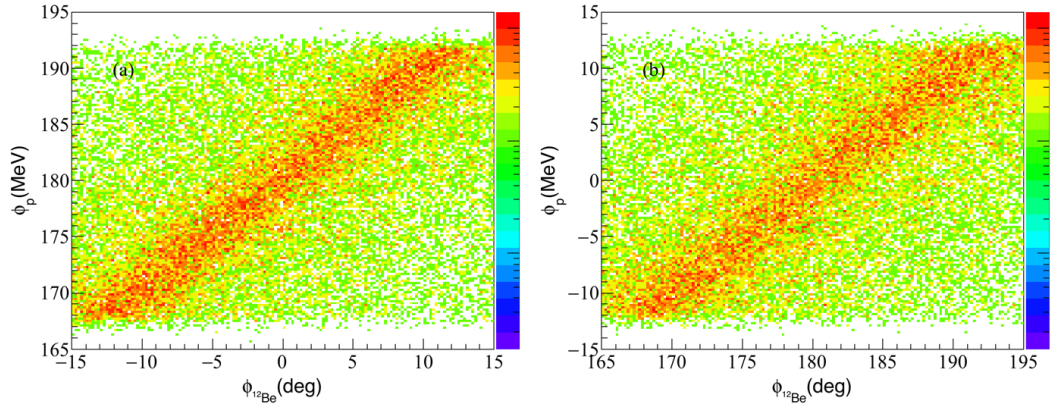

(b) ^{12}Be beam (a) Left ESPRI; (b) Right ESPRI

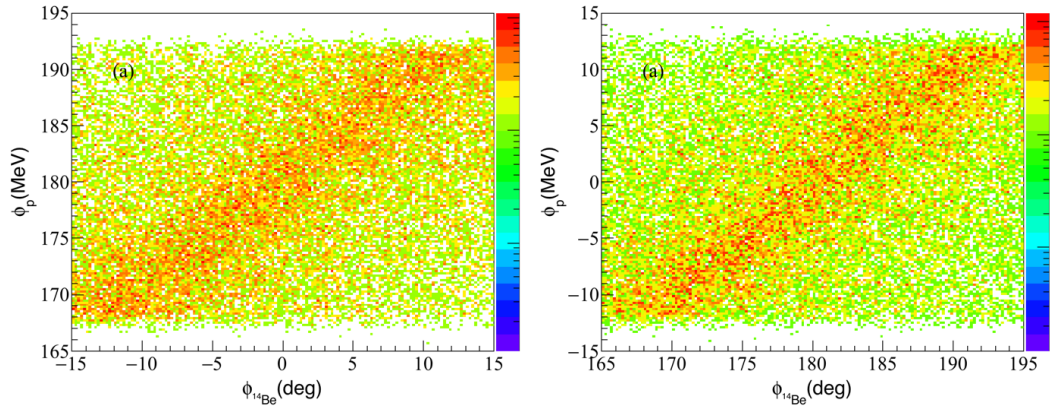

(c) ^{14}Be beam (a) Left ESPRI; (b) Right ESPRI

Figure 54 Coplanarity plots in the (p, p') scattering

magnetic field has a stronger influence on the right side of ESPRI. The coplanarity gate applied for selecting events is set $180 \pm 5\sigma$. This planarity study also validates the relative alignment of the left and right RDC.

Table 15 Coplanarity condition $\Delta\varphi$ in 3 beam setting

Channel	Side	$\Delta\phi$	σ
^{10}Be$(p,p')^{10}$Be	Left	180.3	2.3
	Right	179.8	3.0
^{12}Be$(p,p')^{12}$Be	Left	180.2	2.4
	Right	179.8	2.8
^{14}Be$(p,p')^{14}$Be	Left	180.2	3.3
	Right	179.8	3.3

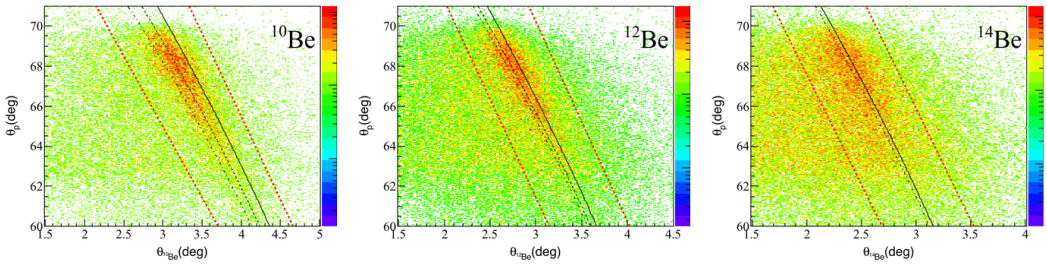

Figure 55 Angle correlation of proton and residue (a)^{10}Be; (b) ^{12}Be; (c) ^{14}Be

Polar angle gate Figure 55 shows the polar angle correlation between recoil proton and scattered Be isotopes. The black solid curves in the sub-figures indicate angle correlation for elastic scattering and the black dashed curves indicate angle correlation for the first 2^+ state of inelastic scattering. The polar angle correlation in Figure 55 were in good agreement with the calculated curves from two-body kinematics. The polar angle gates used for selecting events of (p,p') scattering are marked by red dashed lines. Scattering to excited stated is seen for the ^{10}Be and ^{12}Be beams, while the correlation corresponds to elastic scattering for ^{14}Be beam. As we will see below, this is due to the different selection of the residues.

3.5.2 Excitation energy spectrum

In order to select events of (p,p') scattering, 5 gates have been utilized: Trigger BeamxESPRI, beam PID, target area, coplanarity condition, and polar angle corre-

lation. In addition, hodoscope PID for the reaction residue was also considered. In the case of ^{10}Be and ^{12}Be beam, most of the beam particles were directed into the gap between HODF and HODP to reduce the counting rate, so that mainly inelastic events are measured. Conversely, the beam was stopped in HODP during the ^{14}Be run. Gating on ^{14}Be in the HODP bars allows to select the elastic channel only, as the ground-state is the only bound-state in ^{14}Be.

Figure 56 shows the energy angle correlation plot of recoil protons and the correlation excitation energy spectra for the three beams. The solid curves in the left figures are calculated from the two-body kinematics, upper and lower curves corresponding to the ground state and first excited 2^+ state. For ^{10}Be beam, two peaks in Figure 56ab centered at 0 and 3.37 MeV, corresponding to the ground-state and 2^+ state are observed, respectively. In the ^{12}Be(p,p') scattering, the spectrum of Figure 56b shows the first excited 2^+ state peaked at 2.11 MeV. The known resonance peak at around 4.6 MeV can be also observed.

2n separation energy in ^{14}Be is only 1.27 MeV which makes no bound state above the ground state. Figure 56c shows the excitation spectrum of events from elastic scattering and inelastic scattering for ^{14}Be beam, obtained by gating on ^{14}Be and ^{12}Be in hodoscope, respectively. For the ground state of ^{14}Be, the width of excitation energy is σ= 0.9 MeV. Unlike the previous two cases of ^{10}Be and ^{12}Be beam, the yields of the first 2^+ state of ^{14}Be are comparable to the ground state at large scattering angles. The position and width of the 2^+ state extracted from the missing mass spectrum is (1.56 $\pm$ 0.06) MeV and 0.9 MeV, respectively. This result is consistent with [40]. The excitation energy and energy resolution obtained in this missing mass measurement are summarized in Table 16.

Table 16 Excitation energies and resolution obtained for the three beams.

Channel	State	Peak Position(MeV)	σ(MeV)
^{10}Be$(p,p)^{10}$Be	0^+(0.0 MeV)	-0.04 $\pm$ 0.02	0.7
	2^+(3.37 MeV)	3.36 $\pm$ 0.01	0.7
^{12}Be$(p,p')^{12}$Be	2^+(2.11 MeV)	2.12 $\pm$ 0.02	0.7
^{14}Be$(p,p)^{14}$Be	0^+(0.0 MeV)	0.10 $\pm$ 0.05	0.9
	2^+(1.54 MeV)	1.56 $\pm$ 0.06	0.9

The ground-state and 2^+ state are observed at energies very close to the expected values. This validates the calibrations in energy and scattering angles performed in

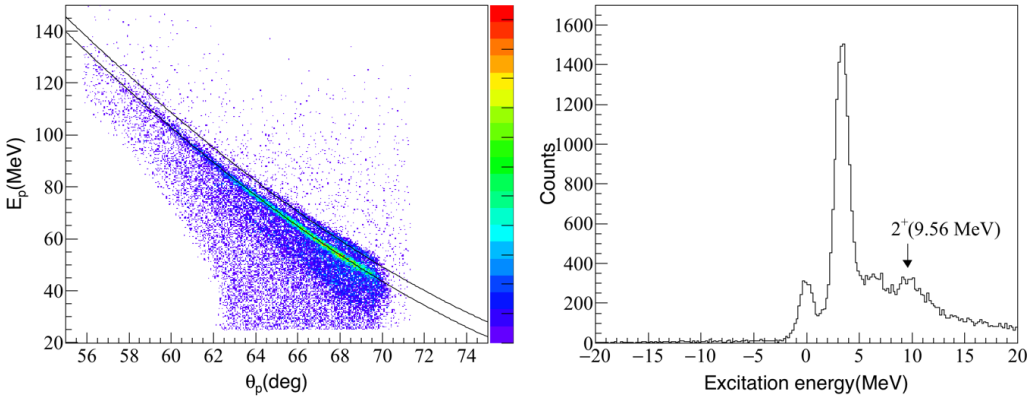

(a) ^{10}Be$(p,p')^{10}$Be scattering

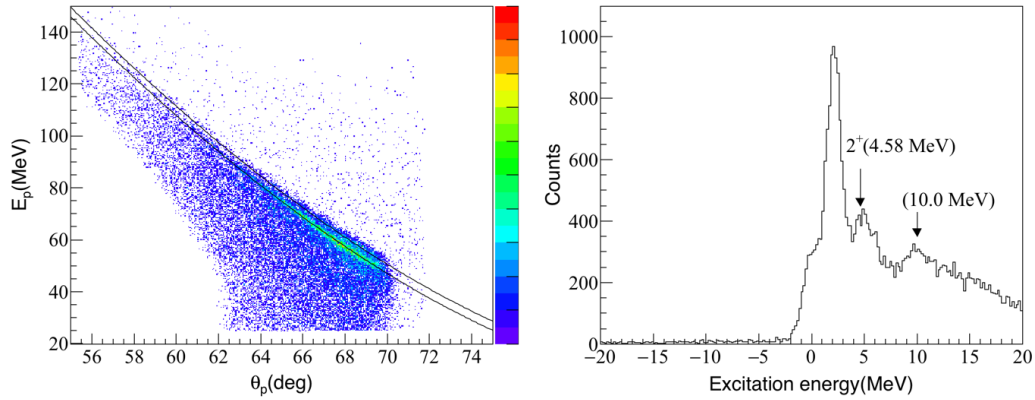

(b) ^{12}Be$(p,p')^{12}$Be scattering

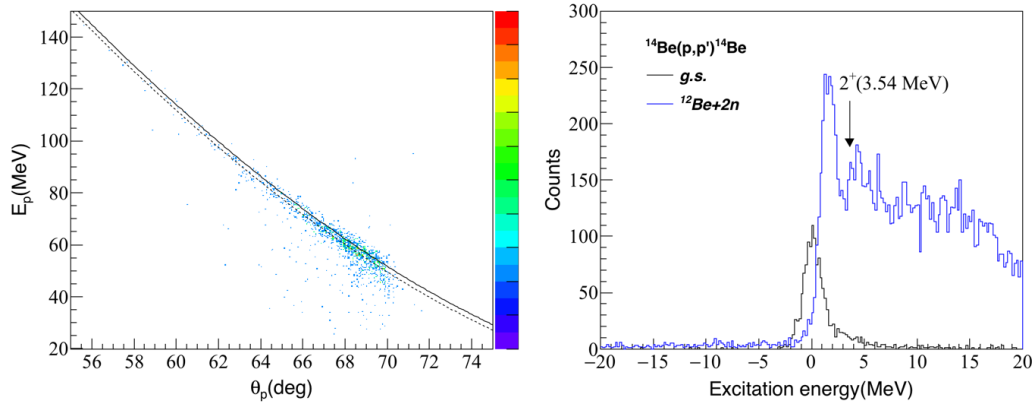

(c) ^{14}Be$(p,p')^{14}$Be scattering

Figure 56 Left: Proton energy vs scattering angle; Right: Missing mass energy spectrum

this work. We note that the resolution is nearly 20% worse for the ^{14}Be beam than the results for other two beams. The reason of this difference is unclear at the present stage.

3.6 Telescope analysis

The four-momentum of the α-cluster from the $(p, p\alpha)$ reaction is reconstructed from the energy and position information provided by telescope analysis. The fired pixel in the DSSD detector provides the alpha particles' 2D position in the plane. As for the ESPRI RDC, DSSD positions are obtained from the PGS measurement. The array of CsI(Tl) detector placed behind the DSSD as the E detector of ΔE-E method provides the energy to reconstruct the total alpha energy. Two defocused alpha beams about 150 MeV/u and 120 MeV/u with narrow energy spread of 0.5 MeV/u were produced for the energy calibration of telescopes. During the calibration runs, each telescope was moved from its original position directly in the beam axis. Beams were defocused in order to cover a large part of the DSSD surface. Table 17 shows the energy loss in DSSD and CsI(Tl) under 2 alpha beam settings.

Table 17 Energy loss in DSSD and CsI(Tl)

Beam	ΔE_{DSSD}(MeV)	E_{CsI}
α@157.52 MeV/u	7.02	495.04
α@121.06 MeV/u	9.79	311.02

3.6.1 DSSD energy calibration

The DSSD detector is calibrated in two steps: 1. align the raw ADC of all the strips; 2. calibrate the aligned ADC into energy. The method is due to the characteristics of DSSD which makes it possible. The active area of DSSD is 64x64 mm^2, much larger than the target cell. Less than half of the detectors could be illuminated even with the help of the defocused beam.

The unique characteristics of the DSSD detector allow a method called self calibration method(SCM) [41] to be applied to solve this problem. When a charged particle hits on the DSSD, front and rear strips both fired at the same time and the electrons and holes after ionization would drift to the corresponding electrodes and

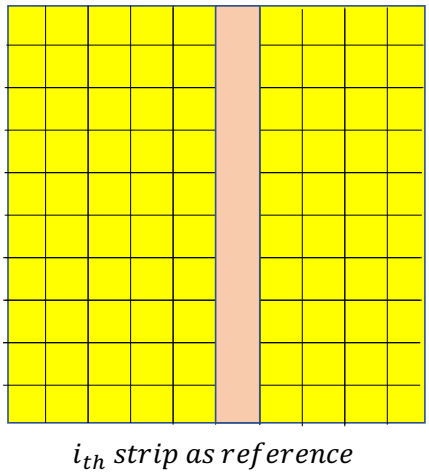

Figure 57 Schematic view of SCM for DSSD

are collected by the strips on both sides. All front strips can be aligned to a particular rear strip, and vice versa. Figure 57 shows a schematic view of SCM taking the i_{th} strip as the reference strip, the strips on the other side are perpendicular to it and have an overlapping area. With the SCM method, 64 strips on the entire DSSD can be normalized to a unified gain. Figure 58 shows an example of ADC correlation between 13th front strip and 15th rear strip before and after SCM treatment.

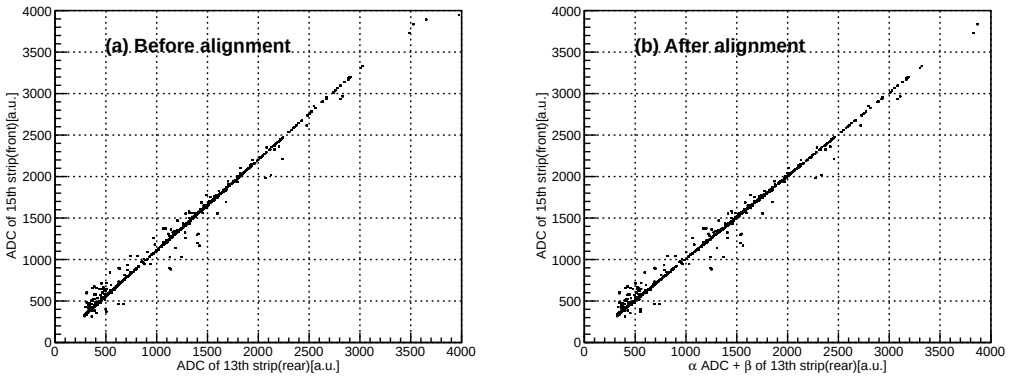

Figure 58 ADC correlation between 13th strip on the front side and 15th strip on the rear side (a) before alignment; (b) after alignment

Figure 59a shows 2 peaks in the energy spectrum, corresponding to the ΔE deposit for the two alpha beam settings, as shown in Table 17. Figure 59 gives energy calibration based on the 2 peaks. The standard deviation in the energy spectrum is around 450 keV in sigma which is much larger than the energy resolution of DSSD. During the experiment preparation, an alpha source test has been conducted for

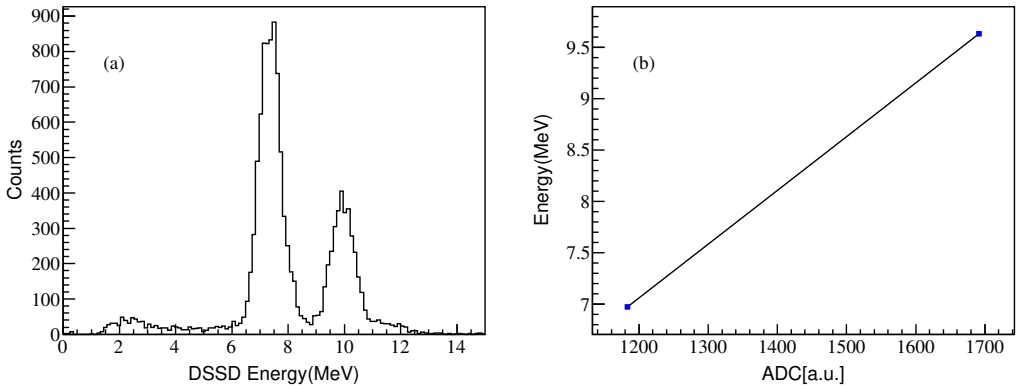

Figure 59 (a) Energy spectrum of DSSD ; (b) calibration of 2 energy points

DSSD and the energy resolution was achieved around 80 keV. The broadening of the peak is mainly due to the energy straggling induced by high energy alpha particles impinging on 1.5 mm thin DSSD detector. According to Lise++ calculation, when the incident energy of alpha particles reaches 500 MeV, the energy straggling of the DSSD detector is around 370 keV in sigma.

3.6.2 CsI(Tl) energy calibration

Alpha particles deposit most their of energy in the CsI detectors, so the energy calibration of CsI(Tl) detectors is the most important step in reconstructing alpha energy. Figure 60 shows the raw ADC distribution under 2 alpha beam settings. 5 peaks can be seen in Figure 60a and merged peaks can be seen in Figure 60b. These extra peaks is due to the different materials crossed around the target area.

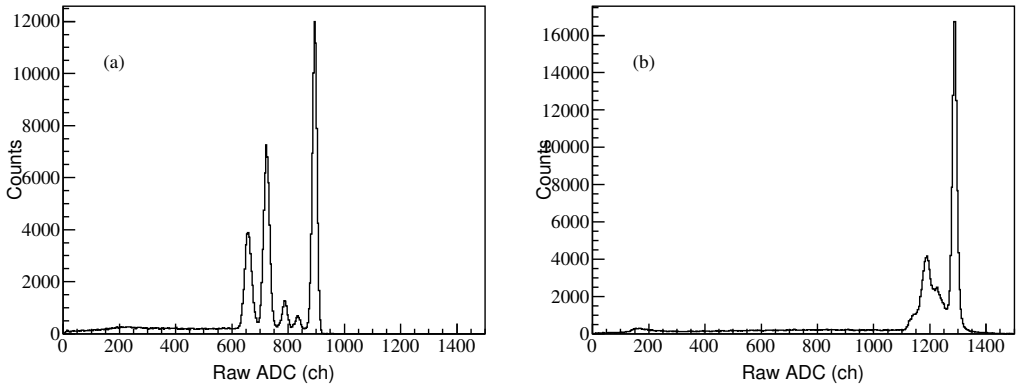

Figure 60 Raw ADC distribution of CsI detectors (a) α@121.06 MeV; (b) α@157.52 MeV

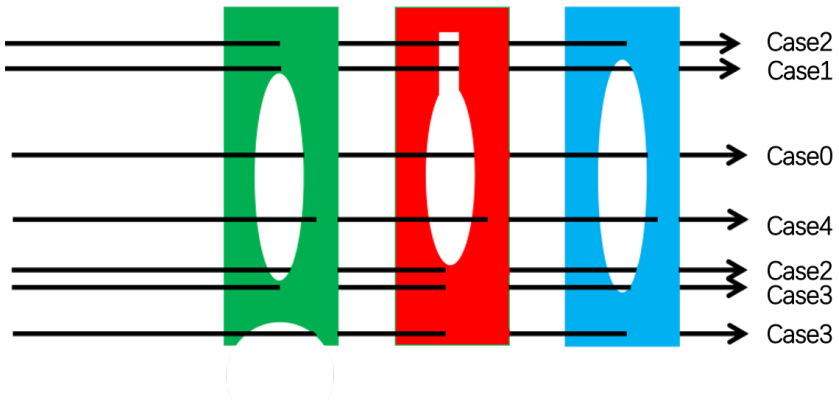

Figure 61 Cooper frames of SHT

Figure 61 shows 5 possible cases when the beam particles pass through the target area, due to the radius and shape difference of the frames. There are 3 frames in the target area: 1mm, 2mm, 1 mm copper, respectively. Table 18 summarizes the energy deposit in CsI(Tl) detector under different cases. By carefully considering these energy losses due to the frames, one can obtain several calibration points.

Table 18 CsI energy deposit calculated by Lise++

Beam	case	Front	Target	Back	E_{CsI}(MeV)
	0	✗	✗	✗	500.21
	1	✓	✗	✗	485.27
α@157.52 MeV	2	✗	✓	✗	469.97
	3	✗	✓	✓	454.34
	4	✓	✓	✓	438.29
	0	✗	✗	✗	318.27
	1	✓	✗	✗	297.24
α@121.06 MeV	2	✗	✓	✗	275.03
	3	✗	✓	✓	251.38
	4	✓	✓	✓	225.87

Figure 62a shows the fitting for energy calibration of each CsI crystal whose name is listed in Figure 28b. The Birks formula has been applied for energy calibration for CsI detectors, similar to the procedures of NaI calibration. Figure 62b shows the calibrated energy spectrum. The high energy peak around 500 MeV seems broader than the low energy peaks. This is due to the fact that alpha particles at 500 MeV has about 4.5 cm range in CsI(Tl) detector which is almost at the end of each crystal, especially for the Type2 LL crystal with 5 cm length.

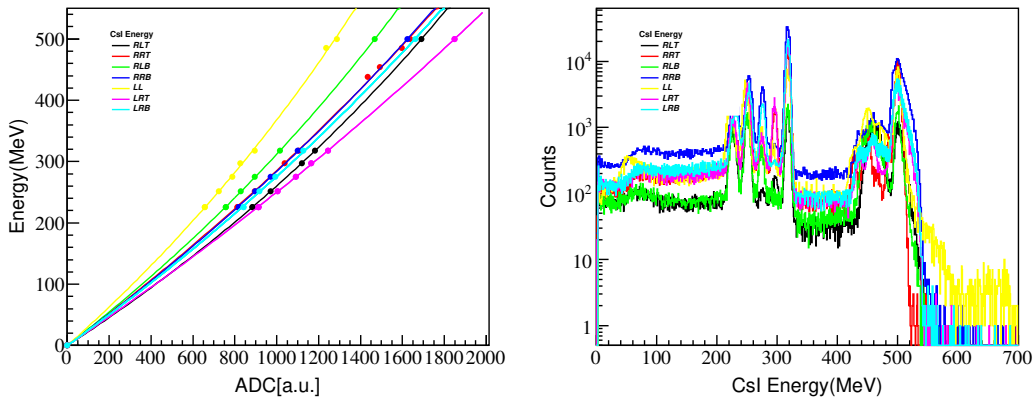

Figure 62 (a) CsI calibration; (b) Energy spectrum of CsI crystals (Names of CsI crystals are defined in Figure 28b)

3.6.3 Alpha energy reconstruction

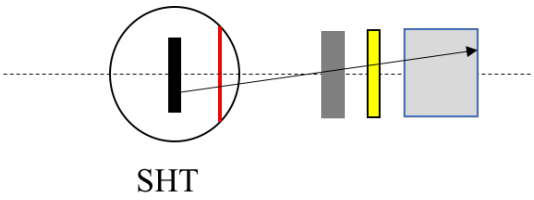

Figure 63 Scheme of alpha-beam run setup

Figure 63 shows the scheme of the experimental setup for the alpha-beam runs. The incident energy of alpha-beam in the middle of target can be reconstructed by energy losses in detectors and materials by back-propagating layer by layer. The DSSD and CsI detectors in the telescopes are well calibrated and described in the previous sections. The energy loss in the 25 mm Al degrader considering the incident angle, and energy loss in the atmospheric environment and window materials have been taken into account for reconstructing alpha energy. Ideally, defocused beam energy equals to the reconstructed alpha energy from telescope analysis.

Table 19 gives the reconstructed alpha energy in the calibration runs. The four calibration runs 596, 597, 598 and 599 correspond to the combination of two defocused alpha-beams and two sets of telescopes on the left and right sides. Comparing the alpha energy distribution, the width of alpha particles reconstructing from the telescope is 2.1 MeV, while the width of the alpha beams is 1.5 MeV. As can be seen from the table, the energies of alpha are well reconstructed, despite the energy distribution is 1-2 times larger than the original beam, due to the energy straggling in

the materials. Figure 64 shows the comparison of alpha energy distribution between defocused beams and reconstruction. The flat tail of events with energy ranging from zero to the maximum energy is mainly due to reactions in the detector. In addition, due to the large events loss arising from the nuclear reaction in Al degrader, a Geant4 simulation has been performed to study the efficiency loss in Al (Section 3.7).

Table 19 Alpha energy reconstructed from the calibrated telescopes

Run(α-beams, Side)	E_{beam} (MeV)	σ_{beam} (MeV)	E_{tele} (MeV)	σ_{tele} (MeV)
596 (150 MeV/u, Left)	627.64	1.98	627.75	4.44
597 (150 MeV/u, Right)	627.61	1.98	627.69	4.10
598 (120 MeV/u, Right)	481.21	1.57	481.39	2.13
599 (120 MeV/u, Left)	481.16	1.57	481.46	2.09

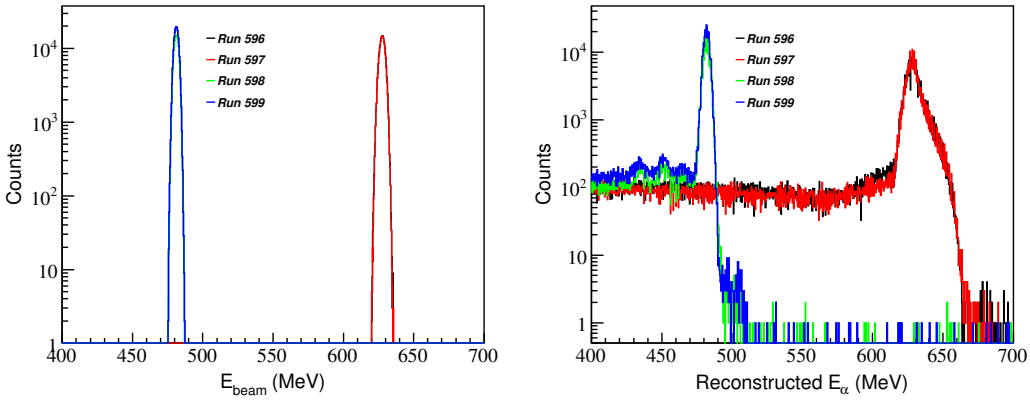

Figure 64 (a) Alpha-beam energy distribution; (b) reconstructed alpha energy distribution

Figure 65 shows a particle identification of the telescopes using ΔE-E method. H and He isotopes are well separated and alpha band in the figure can be clearly identified. Gate of Alpha PID in Figure 65 is applied later for the extraction of physics spectra.

3.6.4 CsI Non-uniformity

During alpha calibration runs, telescopes were placed facing the beam directly. CsI(Tl) crystals can be pixelized using the DSSD information which makes a non-

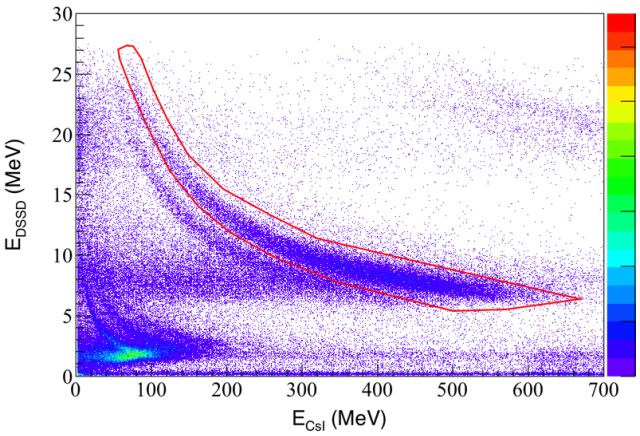

Figure 65 Particle identification of telescope using ΔE-E method

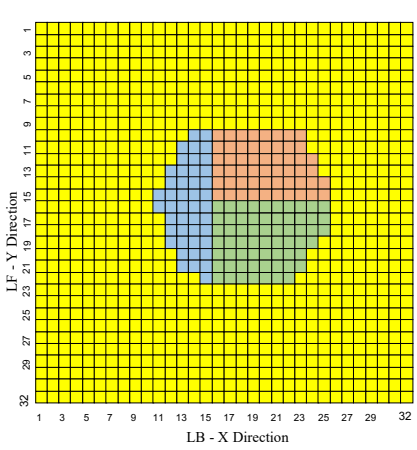

(a) Left telescope, color code: blue-LL; green-LRB; orange-LRT

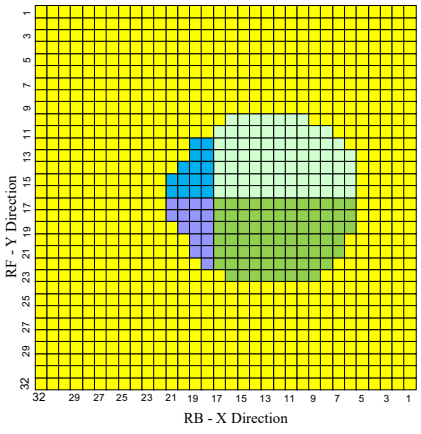

(b) Right telescope, color code: blue-RLT; purple-RLB; light green-RRT; green-RRB;

Figure 66 Selected pixels on CsI crystals for studying non-uniformity

uniformity analysis possible. Figure 66 presents the relative position between DSSDs and CsI(Tl) detectors marked with color code. Selected pixels restricted by the target surface have been used to estimate the non-uniformity of the CsI(Tl) crystals.

Gating on i_{th} front strip and j_{th} rear strip, the energy amplitude E_{ij} of CsI(Tl) detector with position dependency can be extracted and applied for calculating the non-uniformity. The non-uniformity is defined as follows:

$$S_{ij} = \frac{E_{ij} - \langle E \rangle}{E_{beam}} \tag{55}$$

$$\eta = \frac{\sum \left| S_{ij} \right|}{N} \tag{56}$$

where S_{ij} is the percentage of energy deviation of the pixel(i, j), $\langle E \rangle$ is the average E_{ij} of all the selected pixels in one crystal. E_{beam} is the incident energy of alpha particles. The average of the absolute deviation η is used for estimating the non-uniformity of the CsI(Tl) crystals.

Table 20 The non-uniformity of CsI crystals under the defocused alpha beams

Non-uniformity	Alpha Beam(120 MeV/u)	Alpha Beam(150 MeV/u)
LL(5 cm)	0.51%	0.50%
LRT	0.08%	1.13%
LRB	0.22%	1.40%
RLT	0.24%	0.81%
RLB	0.33%	0.52%
RRT	0.45%	0.44%
RRB	0.11%	1.41%

Table 20 shows the non-uniformity summary of all the crystals. For the case of alpha beam with 120 MeV/u, the non-uniformity is below 1 %. For the case of alpha beam with 150 MeV/u, the non-uniformity increased a little in general.The non-uniformity of crystals has a strong correlation with energy loss of the incident particles [42], because of the variation of thallium doping which is the major influence factor of lightning output. Note that lots of pixels selected were in the intersection area of crystals, where the higher possibility of partial energy loss may occur due to multiple scattering. For the case of alpha beam with 150 MeV/u, the Brag peak of energy loss is located at a range of 4.5 cm closed to the end of the crystal. Generally speaking, the non-uniformity of CsI crystals meets the needs of the experiment and the reconstructed alpha energy isn't affected much.

3.7 Simulations for efficiency of detectors

To extract the absolute cross section of $(p, p\alpha)$ reaction, estimating the geometrical acceptance of the experimental setup is crucial. At a given scattering angle θ, the efficiency depends on the converage of detectors in azimuthal angle φ. The geometrical efficiency is defined as the ratio of events detected by detectors and total events emitted from the reaction.

$$\eta(\theta) = \frac{N_{det}}{N_{emit}} \tag{57}$$

Simulations have been performed using the Nuclear Physics Tool (NPTool) software [43] developed by A. Matta et al. NPTool is a Monte Carlo simulation framework based on Geant4 [44] specially developed for nuclear physics experiments. It offers the flexibility and effectiveness on building different detectors systems and now has been successfully applied for the analysis and simulation of complex experiments at GANIL, RIKEN and TRIUMF using both stable and radioactive beams. NPTool allows to input the detailed geometric detector configuration of the setup, hence to determine the efficiency of each component. In the case of alpha cluster detection, it includes the losses due to space between the CsI chrystals, as well as those due to nuclear reactions in the Al degrader and the Csi chrystals.

3.7.1 Event generator

The isotropic source has been used as event generator for the geometrical efficiency simulations: proton source for the ESPRI setup, and alpha source for the telescopes. The beam profile from the experiment was used for generating the initial position and angle of the isotropic source. Figure 67 shows spectra from event generator of alpha particles with ^{10}Be beam profile. The incident energy is uniformly distributed from 400 - 700 MeV, as Figure 67(a) shown. Figure 67(b) shows the polar angle distribution of alpha particles ranging from 0° to 20 °, enough to cover the entire telescopes. The 2D correlation of X vs Y, and θ_X vs θ_Y distribution in Figure 67(c) and (d) presents the “source" profile based on which the event generator can shoot particles randomly. To maintain consistency with extracting the cross-sections, the same gate on impact position on target was applied.

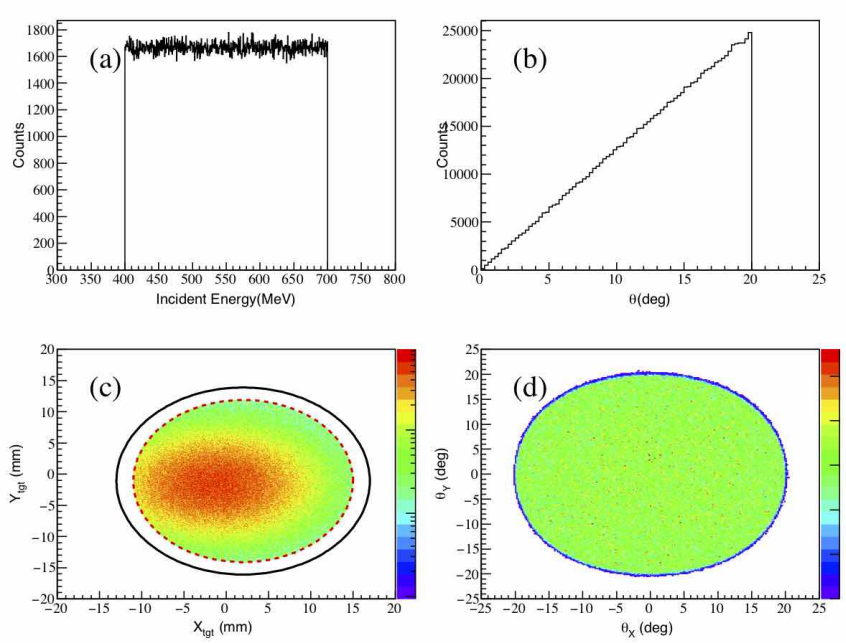

Figure 67 Event generator of alpha source integrated with ^{10}Be beam profile

3.7.2 Efficiency for alpha cluster detection

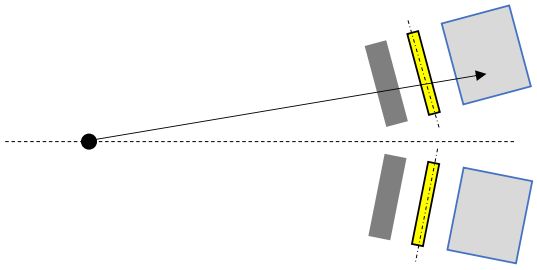

Figure 68 Top view of the telescopes setup

In the NPTool simulation, the material, position, and dimensions of the detectors in the telescopes are set exactly to match the measurements taken in the experiment. Also included are the 25mm-thick Al degrader and air between target and DSSD. Figure 68 shows a schematic top view of the telescopes relative to the target. The energy resolution(FWHM) of CsI detectors is set to 200 keV; The energy resolution(FWHM) of DSSD detectors is set to 80 keV;

Figure 69 shows the simulations of particle identification plots using ΔE-E method. In Figure 69(a) the horizontal band at $E_{DSSD} \approx 7$ MeV is caused by α particles that have escaped the CsI crystals, e.g. in the inter-crystals region. In the following, only events with Csi multiplicity equal to one will be retained (in both

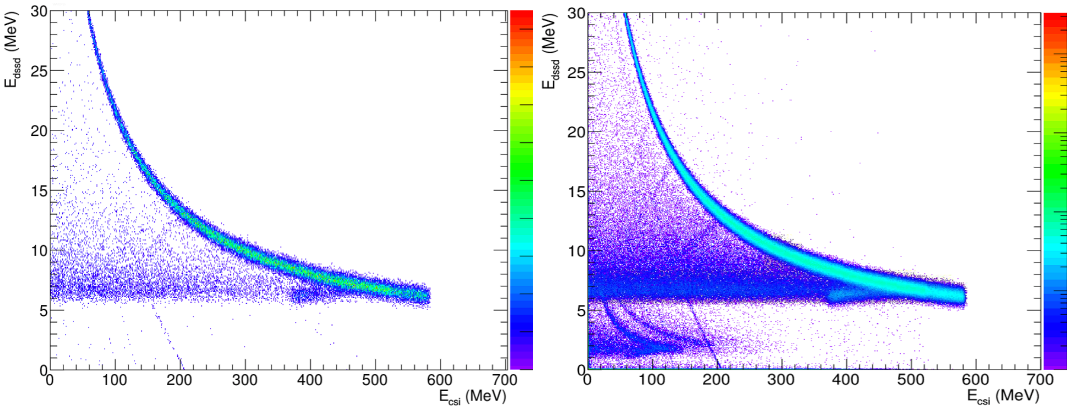

(a) Reaction off

(b) Reaction on

Figure 69 Simulation on particle identification of the telescopes using ΔE-E method

simulations and experimental spectra). Figure 69(b) presents the comparison between same simulated plot obtained when activating the nuclear reactions occurring in the Al degrader, the CsI crystals, and air. In the code the reaction cross-sections were derived by Tripathi [45], and Shen [46] parametrizations which come from empirical and parametrized formula based on theoretical models [47]. A sizeable amount of reacted events is observed, increasing strongly the counts in the horizontal band at about 7 MeV. Lighter particles like hydrogen isotopes are generated by reactions in the degrader and identified in the plot. Both effects are clearly observed in the experimental plot (Figure 65)

To calculate the geometrical efficiency, α band events in the PID plot are considered the effective events. Figure 70 shows the geometrical efficiency plotted as a function of polar angle of α particles. The range of polar angle θ is 2-16 °. Almost half of the total events emitted at $\theta = 6.5$ ° can be captured by the telescopes. There are 80.6% events left in the simulation after activating the reactions in the Al degrader and CsI.

3.7.3 Efficiency for proton detection

The detectors of the ESPRI setup were input in the NPTool simulation. 3D position of RDC were obtained from PGS measurement. Figure 68 shows a top view of the ESPRI setup in the simulation.

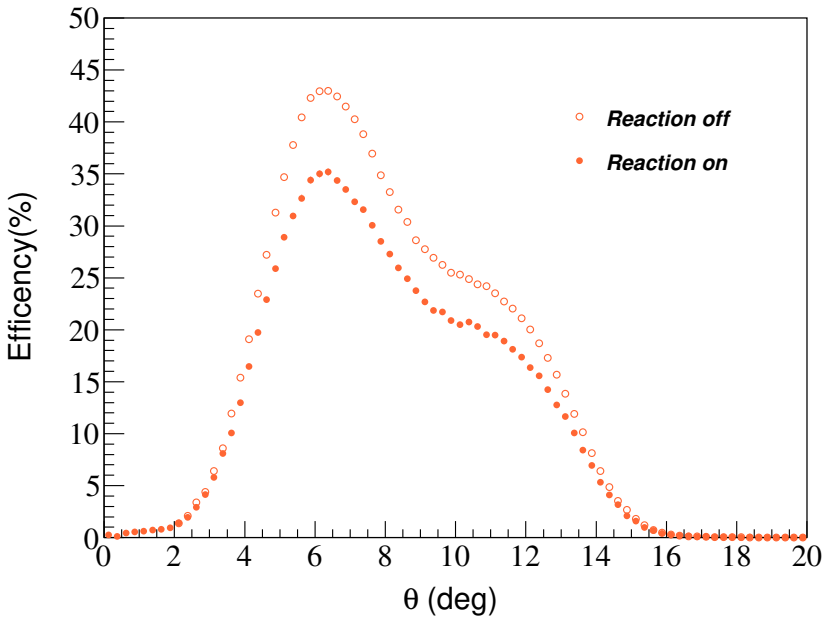

Figure 70 Efficiency of telescopes in the laboratory frame as a function of polar angle

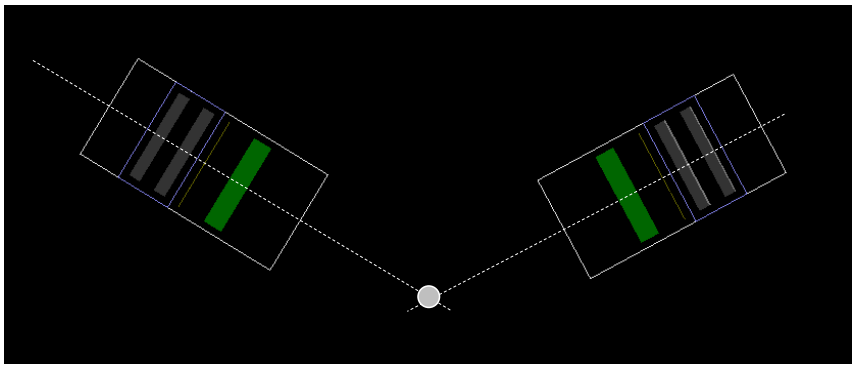

Figure 71 Top view of ESPRI setup in the simulation

The isotropic proton source was set with energy range 30-100 MeV and polar angle from 40-80 ° which covers the entire ESPRI acceptance. The Energy resolution(FWHM) of NaI detectors was set to 1%. The timing resolution(FWHM) of plastic was set to 500 ps. Figure 72(a) and (b) show the particle identification using the ΔE-E method and ΔE-ToF method, respectively.

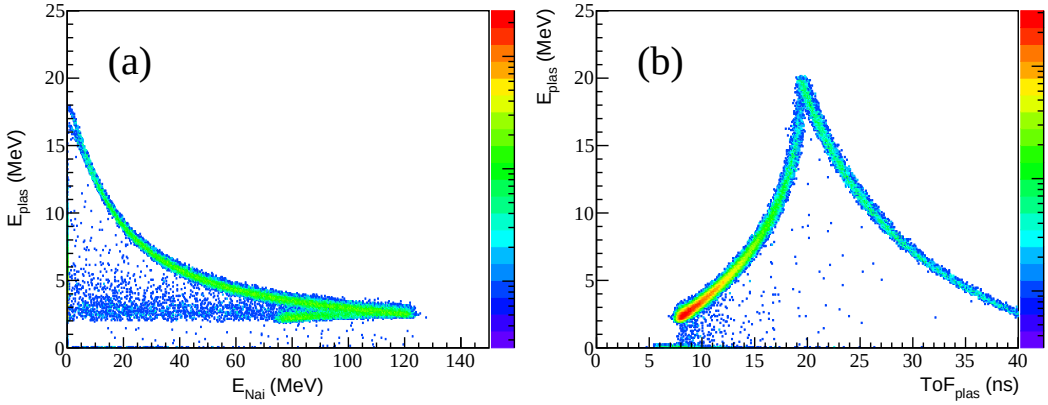

Figure 72 Proton identification in the simulation (a) ΔE-E; (b) ΔE-ToF

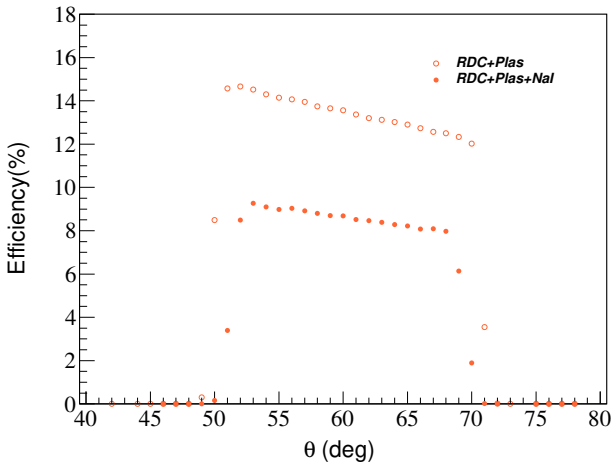

Figure 73 Efficiency of the ESPRI setup in the laboratory frame

Depending on the method for reconstructing the proton energy, two types of geometrical efficiencies are extracted. The geometrical efficiency only consider the acceptance of RDC and plastic detectors, if the proton energy is reconstructed from ToF measurement; while it also needs to take into account the acceptance of NaI bars if the proton energy is reconstructed from the energy deposit in NaI detectors. Figure 73 shows the geometrical efficiency curve of the ESPRI setup, the former marked by open circle, the latter marked by filled circle. Since the ESPRI setup is

placed far from the target, less than one-fifth of the emitted protons can be detected. As can be seen from the figure, there is one-third of the remaining events loss due to the acceptance of NaI bars. In the later work of extracting absolute cross sections, the geometrical efficiency in filled circles is applied, since the NaI bars gives better energy resolution.

3.7.4 Efficiency for the relative azimuthal angle φ_{12}

In the QFS $(p, p\alpha)$ reaction, proton and α in pairs and have approximately coplanar characteristics. From the above two sections, the limitation of geometrical efficiency comes from the proton detection. In other words, as long as protons from the reaction are detected by the ESPRI setup, then the corresponding α ideally are captured by the telescopes. In the following, geometrical efficiency simulation for the alpha detection has been performed, assuming the proton is detected.

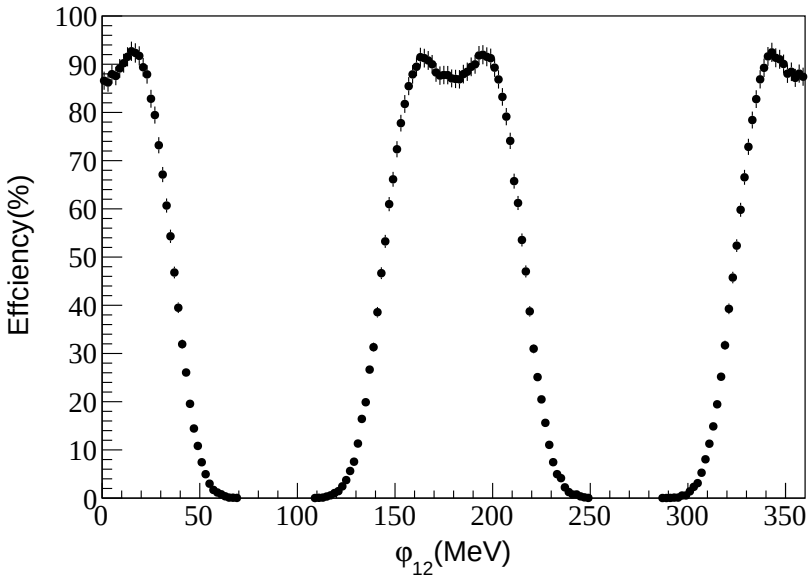

Figure 74 geometrical efficiency of φ_{12}

We define φ_1, and φ_2 as the azimuth angle of proton and α using the horizontal plane as a reference, respectively. The φ_{12} angle is defined as

$$\varphi_{12} = \varphi_2 - \varphi_1 \tag{58}$$

If the proton and α come from independent sources, then the φ_{12} is uniformly distributed in [0,2π]. It is known that QFS reactions are essentially plannar, and our setup is designed to take this correlation into account.

Figure 74 shows the geometrical efficiency of φ_{12}. The efficiency curve of φ_{12} in range of [110, 250] of interest represents the geometrical efficiency for the α detection, assuming the proton is detected.

The efficiency of φ_{12} is around 90% in the range [160,200]. The efficiency loss is mainly caused by the events where the alpha particles have escaped the CsI crystals. Note that these events are removed when selecting the alpha particle locus in the telescope PID plot so that the efficiency in this range is actually 100%.

Chapter 4

Results and discussion

In this chapter, physical observables for the quasifree α-knockout reactions studied will be extracted and compared with theoretical model predictions. Section 4.1 presents the excitation energy spectra for the $(p, p\alpha)$ reactions. Section 4.2 details the extraction of the experimental differential cross-sections for the ground-state transition in the case of ^{10}Be and ^{12}Be beams. and provides the comparison with DWIA calculation using the THSR wave functions. Section 4.3 extracts the cross-sections for the ground-state and first 2^+ state transition and discusses the population ratio of these two states in the case of ^{10}Be and ^{12}Be beams.

4.1 Excitation energy spectra

Let us consider the following three-body reaction:

$$\mathrm{A} + 0 \rightarrow 1 + 2 + \mathrm{B} \tag{59}$$

where A is the beam ion, particle 0 the target proton, particle 1 and 2 the outgoing proton and alpha cluster, and B the residual nucleus. The physical quantities of particle i are defined as follows: the total energy E_i, the momentum $\mathbf{p_i}$, the rest mass m_i, the kinetic energy T_i, the polar angle θ_i and the azimuthal angle φ_i. The conservation of energy and momentum before and after the reaction are expressed as

$$E_A + E_0 = E_1 + E_2 + E_B \tag{60}$$

$$\mathbf{p_A} = \mathbf{p_1} + \mathbf{p_2} + \mathbf{p_B} \tag{61}$$

The physical quantities of particle B which usually is not measured in the experiment can be deduced from Eq. 60 and Eq. 61 [48]:

$$E_B = E_A + E_0 - E_1 - E_2 \tag{62}$$

$$p_B = \left(p_A^2 + p_1^2 + p_2^2 - 2p_A p_1 \cos\theta_1 - 2p_A p_2 \cos\theta_2 + 2p_1 p_2 \cos\theta_{1-2}\right)^{1/2} \tag{63}$$

where θ_{1-2} is the angle between $\mathbf{p_1}$ and $\mathbf{p_2}$ which can be calculated with known angles

$$\cos\theta_{1-2} = \cos\theta_1\cos\theta_2 + \sin\theta_1\sin\theta_2\cos\left(\varphi_2 - \varphi_1\right) \tag{64}$$

The mass m_B^* and excitation energy Ex^* of residue are derived as follow:

$$m_B^* = \sqrt{E_B^2 - p_B^2} \tag{65}$$

$$Ex^* = m_B^* - m_B(g.s.) \tag{66}$$

where $m_B(g.s.)$ is the rest mass of residue B.

4.1.1 ^{10}Be$(p, p\alpha)$

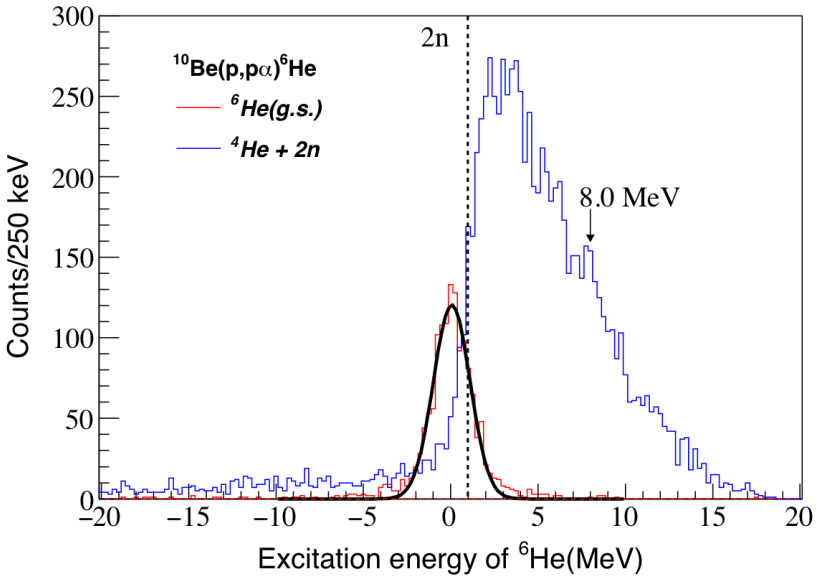

Figure 75 Excitation energy spectra for ^{10}Be$(p, p\alpha)^6$He reaction

Figure 75 shows the excitation energy spectra for ^{10}Be$(p, p\alpha)^6$He reaction. Since the two-neutron separation energy of ^{6}He marked by the dashed line is only 0.975 MeV, and the excited states above have a lifetime less than femtosecond order, the ground state of ^{6}He is the only bound state and can be separated from the excited state by particle identification of the Hodoscopes. The excitation energy spectrum from the ground-state transition is drawn with the red curve in Figure 75. The spectrum is well reproduced by a Gaussian curve centered at $Ex = 0.15 \pm 0.06$ MeV, which validates the calibrations of detectors of protons and clusters. The width $\sigma = 1.07$

MeV is the resolution obtained in the present missing-mass measurement.

The vertical dashed line in Figure 75 shows the threshold of 2-neutron separation. The green curve in Figure 75 represents the excitation energy spectrum for the reaction channel $^{10}\mathrm{Be}(p,p\alpha)^{6}\mathrm{He}^{*} \rightarrow {}^{4}\mathrm{He}+2n$ by selecting ^{4}He in the Hodoscopes PID plot. The first excited state is a 2^{+} state located at 1.8 MeV [49]. Other resonances located at 2.6 ± 0.3 MeV and 5.3 ± 0.3 MeV as reported in the literature [50]. The present spectrum indicates a resonance at around 8 MeV, not mentioned in earlier works. The decomposition of this spectrum for selected angular bins will be presented in the following.

4.1.2 ^{12}Be$(p,p\alpha)$

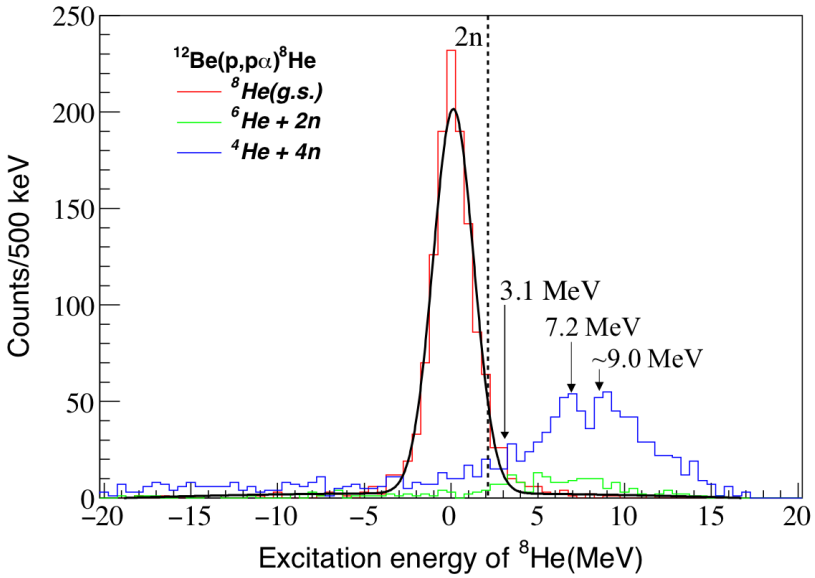

Figure 76 Excitation energy spectra for $^{12}\mathrm{Be}(p,p\alpha)$ reaction

Figure 76 shows the excitation energy spectra for $^{12}\mathrm{Be}(p,p\alpha)^{8}\mathrm{He}$ reaction. The vertical dashed line in the figure shows the threshold of two-neutron separation at 2.13 MeV. As in the previous case, the ground state is the only bound state. By selecting ^{8}He, ^{6}He, and ^{4}He in the PID of hodoscopes, the excitation energy spectra for the three reaction channels are drawn with the red, green, and blue curves in

Figure 76, respectively.

$$^{12}\mathrm{Be}(p,p\alpha)^{8}\mathrm{He}^{*} \rightarrow {}^{8}\mathrm{He(g.s.)} \tag{67}$$

$$\rightarrow {}^{6}\mathrm{He} + 2n \tag{68}$$

$$\rightarrow {}^{4}\mathrm{He} + 4n \tag{69}$$

The width of the ground-state peak is $\sigma = 1.13 \pm 0.03$ MeV. Peak positioned at 7.2 MeV [51] is observed and marked in Figure 76. A new resonant-like located around 9.0 MeV not mentioned in the literature is observed.

The energy values of 2^{+} state in the literature are discrepant, ranging from 2.7 MeV to 3.6 MeV [52, 53, 54, 55, 56] The value E = 3.1 MeV is obtained from the average of the measured values [51]. There is an indication of the population of the 2^{+} state. The population of the 2^{+} and other excited states in the residue is radically different between $^{10}\mathrm{Be}(p,p\alpha)$ and $^{12}\mathrm{Be}(p,p\alpha)$ reactions. The ground-state transition is a minor part for the latter, while it strongly dominates over the 2^{+} and other states transitions for the former. This new experimental finding shows that the contribution of He core-excited states in the ground state is very different between ^{10}Be and ^{12}Be. It indicates that the cluster structures in the ground state are actually quite different from each other. In the next section, we will extract the ratio between ground-state and 2^{+} state cross-sections in the α-cluster knockout reaction.

4.1.3 $^{14}\mathrm{Be}(p,p\alpha)$

This reaction allows to populate states in the "superheavy" (unbound) Helium isotope ^{10}He with extreme value of N/Z = 4, the largest ratio value known to date. Figure 77 shows the excitation energy spectra for $^{14}\mathrm{Be}(p,p\alpha)$. The horizontal axis corresponds to the energy with respect to the 8He+2n threshold. The possible decay modes of the residue ^{10}He are as follows:

$$^{10}\mathrm{He} \longrightarrow {}^{8}\mathrm{He} + 2n \tag{70}$$

$$^{10}\mathrm{He} \longrightarrow {}^{6}\mathrm{He} + 4n \tag{71}$$

$$^{10}\mathrm{He} \longrightarrow {}^{4}\mathrm{He} + 6n \tag{72}$$

From the figure we can see that the decay channel $^{10}\mathrm{He} \rightarrow {}^{8}\mathrm{He} + 2n$ dominates in the $^{14}\mathrm{Be}(p,p\alpha)$ reaction. The other two channels have lower statistics, and larger background. The ground-state mass of ^{10}He is still a matter of interest [57]. The ground state of ^{10}He is a resonant state that cannot be simply fitted with a Gaussian,

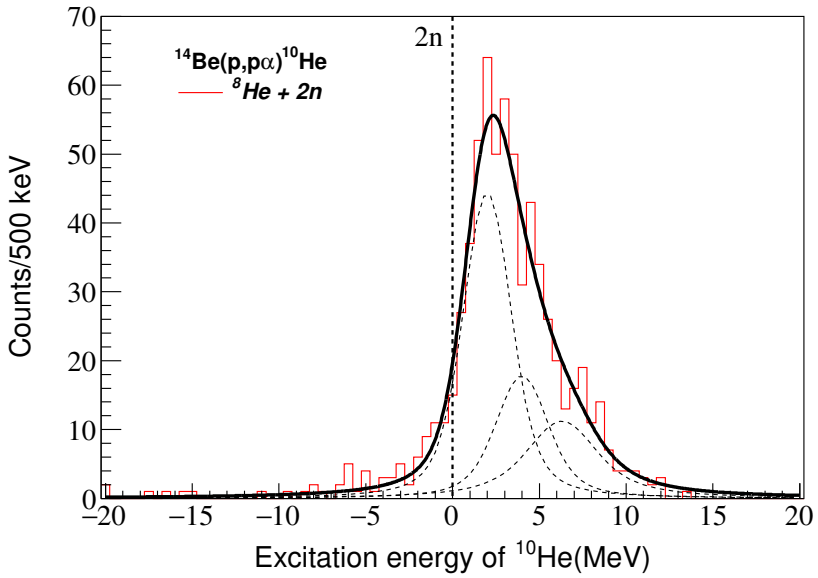

Figure 77 Excitation energy spectra for ^{14}Be$(p, p\alpha)$ reaction

and it can be seen from the figure that there are contributions from other excited states.

In the context of relativistic kinematics, the Breit-Wigner distribution is introduced to describe resonance with the energy E_R and intrinsic width Γ_R. The Breit-Wigner function is defined as

$$f(E) = \frac{1}{\pi} \frac{\Gamma_R/2}{\left(\mathrm{E} - \mathrm{E}_R\right)^2 + \left(\Gamma_R/2\right)^2} \tag{73}$$

The Breit-Wigner distribution is also called the Lorentzian distribution, or referred to as the Cauchy distribution in mathematics. In contrast to the Gaussian distribution, it is characterized by a long-range tail.

The resonance is modeled as the convolution of Breit–Wigner shapes with a Gaussian function, taking into account the experimental resolution. This function is called the Voigtian function [58], defined as:

$$F_{\mathrm{Voigt}}\left(E;\mathrm{E_R},\Gamma,\sigma\right) = \int_{-\infty}^{+\infty} dE' F_{\mathrm{Gauss}}\left(E';0,\sigma\right) F_{\mathrm{BW}}\left(E - E';\mathrm{E_R},\Gamma_R\right) \tag{74}$$

The excitation energy spectrum of ^{10}He is decomposed with the ground state and another two known resonances at 4.0 MeV [59] and 6.3 MeV [57]. The parameter σ of the Gaussian representing the experimental resolution is fixed at 1.1 MeV, The

ground-state energy E and width Γ are left as free parameters. The fitting result of ground-state from the decomposition is at $E = 2.0 \pm 0.1$ MeV, $\Gamma = 1.3$ MeV. 2.0 MeV is higher than the value 1.6 MeV reported in [59, 60] and 1.4 MeV reported in [57], possibly due to the calibration.

4.2 Triple differential cross section(TDX)

The triple differential cross-sections (TDX) is the main quantity measured in QFS studies. In the case of the present $(p, p\alpha)$ study, information on the clustering properties in Be isotopes can be obtained by comparing experimental TDX with DWIA calculations of this quantity. For all beam cases, the $(p, p\alpha)$ reaction yields leading to the ground state and low-lying excited states of the residue nuclei were measured. In this section, cross sections for the QFS $(p, p\alpha)$ reaction are extracted at the coplanar angle pairs $(\theta_p, \theta_\alpha)$ which were chosen to include zero recoil momentum condition of the residual nucleus and compared to DWIA calculation from [26].

4.2.1 Extracting TDX in the experimental acceptance

The experimental TDX usually is given in the unit of μb/sr^2·MeV in the laboratory system. For a given angle pair $\left(\theta_1, \theta_2\right)$, the TDX can be written as:

$$\frac{d^3\sigma^{exp}}{dT_1 d\Omega_1 d\Omega_2} = \frac{\Delta N(T_1)}{N_{tgt} N_{beam} \varepsilon_{det} \Delta T_1 \cdot PV(T_1) \Delta\varphi_1\left(\theta_1\right) \cdot \varepsilon_{\varphi_{12}}} \tag{75}$$

where index 1 and 2 stand for the proton and alpha, respectively in the final state of the $(p, p\alpha)$ reaction.

- $\Delta N(T_1)$ = Number of counts in an energy bin ΔT_1
- N_{tgt} = Number of proton per unit area in the SHT
- N_{beam} = Number of incident beam particles on the target
- ε_{det} = “Intrinsic" efficiency of proton and alpha detectors
- $PV(T_1)$ = the phase volume restriction due to three-body kinematics
- $\Delta\varphi_1\left(\theta_1\right)$ = the φ_1 acceptance from the NPTool simulation
- $\varepsilon_{\varphi_{12}}$ = the φ_{12} efficiency from the NPTool simulation

The number of incident beam particles N_{Beam} on the target is estimated from the downscaled beam trigger and given by:

$$N_{beam} = c \cdot N_{DSB} \tag{76}$$

where the $c = 1500$ is the downscaling factor of beam-trigger, N_{DSB} is the beam counts gated by the downscaled beam-trigger, beam PID, and the selected target area discussed in Chapter 2.

The number of proton per unit area in the SHT is an constant given by:

$$N_{target} = \frac{\rho_H N_A}{M_H} \times d \tag{77}$$

where the thickness of target $d = 2$ mm, N_A is the Avogadro constant. the mass density of solid hydrogen is $\rho_H = 0.086$ g/cm^3, $M_H = 1.00794$ g/mol;

Intrinsic efficiencies ε_p and ε_α of proton and alpha detectors have been discussed in Chapter 3. For protons, it is determined by the RDC detection and reconstruction efficiency, which is about 90%. For alphas, it corresponds to losses due to nuclear reaction of alpha particles in the 25mm Al degrader and CsI crystals, as well as to alphas escaping from the crystals. The corresponding loss in efficiency is about 20%.

The phase volume term $PV(T_1)$ is to express the restriction of $d\Omega_1 \cdot d\Omega_2$, due to the three-body kinematics.

$$PV(T_1) = \sum_{\theta_1} \sum_{\theta_2} \sum_{\varphi_2} \left[\cos\theta_1\right]_{\theta_1+d\theta_1}^{\theta_1} \left[\cos\theta_2\right]_{\theta_2+d\theta_2}^{\theta_2} \left[\varphi_2\right]_{\varphi_2}^{\varphi_2+d\varphi_2}(T_1) \tag{78}$$

where the summation range of θ_1, θ_2, and φ_{12} is restricted to satisfy the energy-momentum conservation.

The p-α pairs from the quasi-free processes have coplanar properties. Therefore, the simulation of experimental acceptance should be considered for detecting the p-α pairs, not separately. Since the telescopes were placed at forward angle with high angular acceptance, the total efficiency for detecting p-alpha pairs with relative experimental acceptance is largely determined by the detection of protons. The NPTool simulation of $\Delta\varphi_1(\theta_1)$ and φ_{12} have be discussed in the Chapter 3. φ_{12} is nearly constant over the range of $[160°, 200°]$, which was taken here. It is larger than the range of experiments in forward kinematics. The wide range of φ_{12} angle also provides us the opportunity to study the φ_{12} angle distribution in the $(p, p\alpha)$ reaction.

4.2.2 The THSR model calculation

The TDXs with DWIA formalism have been calculated with α-cluster wave function deduced from extended version of the THSR model [26] for the ^{10}Be$(p, p\alpha)^6$He(g.s.)

and ^{12}Be$(p, p\alpha)^{8}$He(g.s.) reactions. All the wave functions used in the calculation of the transition amplitude can be microscopically obtained from the THSR model. The optical potential for each system is given by folding density distributions of A and B, which are predicted by the THSR wave function with an effective nucleon-nucleon (NN) interaction. The distorted wave functions $\chi_i (i = 0, 1, 2)$ are then obtained by solving the corresponding Schrödinger equations. The α-cluster wave function is extracted from the THSR wave function of A by approximating the reduced width amplitude (RWA).

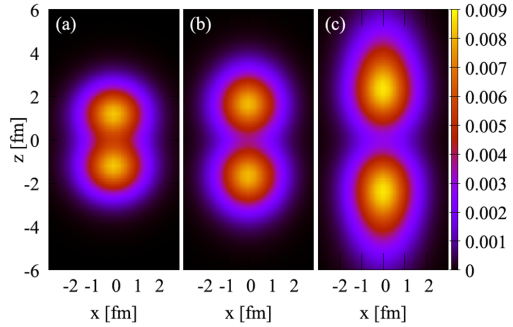

Figure 78 Charge distribution of ^{10}Be nucleus for the (a) artificial shell-model-like state, (b) the physical ground state, and (c) artificial gas-like cluster state. [13]

The ground state of ^{10}Be has only one molecular configuration in the description of THSR model: $2\alpha + 2n(\pi)$. Figure 78(b) shows the charge distribution of the ^{10}Be using the THSR model [13]. The molecule-like cluster structure with two α center can be clearly observed. In ref. [13], using the flexible model space of the THSR wave function, the physical ground state of ^{10}Be was evolved into artificial states in Figure 78(a) and (c), which are constructed by manually changing the size of the α-cluster distribution β in the THSR wave function.

By using cluster wave function corresponding to the three configuration of Figure 78, it was shown that the TDX are very sensitive to the cluster structures in the ground state of ^{10}Be. The direct manifestation of the molecular cluster structure in the ground state of ^{10}Be can be obtained by comparing the experimental results with the theoretical calculations.

For ^{12}Be, three kinds of cluster configurations were considered in [18]: the binary cluster configuration

$$\alpha + {}^{8}\mathrm{He} \tag{79}$$

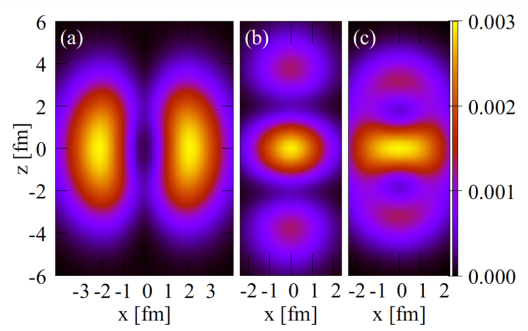

Figure 79 The density distribution of valance neutron of ^{12}Be nucleus in configuration: (a) π-orbit, (b) σ-orbit, and (c) α+^{8}He [18].

and the other two molecular orbit configurations

$$2\alpha + 2n(\pi) + 2n(\pi *)(\pi - \text{orbit}) \tag{80}$$

$$2\alpha + 2n(\pi) + 2n(\sigma)(\sigma - \text{orbit}) \tag{81}$$

The four valence neutrons surrounding two α center in three configurations correspond to occupying: the vertical p-orbit state in ^{8}He; the molecular π-orbits; two in the π-orbit and the other two in the σ-orbit. Figure 79 show the density distribution of valence neutrons of the ^{12}Be for three different configurations, The sensitivity of the TDX magnitude to different components shows the TDX is also a good experimental observables for investigating the cluster structure of ^{12}Be.

It should be noted that the three configurations are not orthogonal to each other. The total cluster wave function is obtained by superposing the basis states of the three configurations described by THSR model. Due to the coexistence of binary clustering and molecular orbit configurations, the experimental TDX will bring constraints to quantify the mixing ratio in the ground state of ^{12}Be.

4.2.3 Comparison of experimental TDX with the theoretical calculation

DWIA calculations of TDX were performed using steps of 1MeV for T_1, 0.1° for θ_1 and θ_2, and 1° in φ_2 within the experimental acceptance, with $\varphi_1 = 0°$. The calculated TDX in the experimental acceptance were obtained as follows:

$$\frac{d^3\sigma^{th}}{dT_1 d\Omega_1 d\Omega_2}(T_1) = \frac{\sum_{\theta_1}\sum_{\theta_2}\sum_{\varphi_2} TDX\left(T_1,\theta_1,\theta_2,\varphi_2\right)\left[\cos\theta_1\right]_{\theta_1+d\theta_1}^{\theta_1}\left[\cos\theta_2\right]_{\theta_2+d\theta_2}^{\theta_2}\left[\varphi_2\right]_{\varphi_2}^{\varphi_2+d\varphi_2}}{\sum_{\theta_1}\sum_{\theta_2}\sum_{\varphi_2}\left[\cos\theta_1\right]_{\theta_1+d\theta_1}^{\theta_1}\left[\cos\theta_2\right]_{\theta_2+d\theta_2}^{\theta_2}\left[\varphi_2\right]_{\varphi_2}^{\varphi_2+d\varphi_2}} \tag{82}$$

where $\varphi_1 = 0$ in the calculation, $\varphi_2 = \varphi_{12}$ which is the difference between φ_1 and φ_2 in the experimental results. The integration range of (θ_1, θ_2, φ_2) is limited by the phase volume as for the experimental TDX.

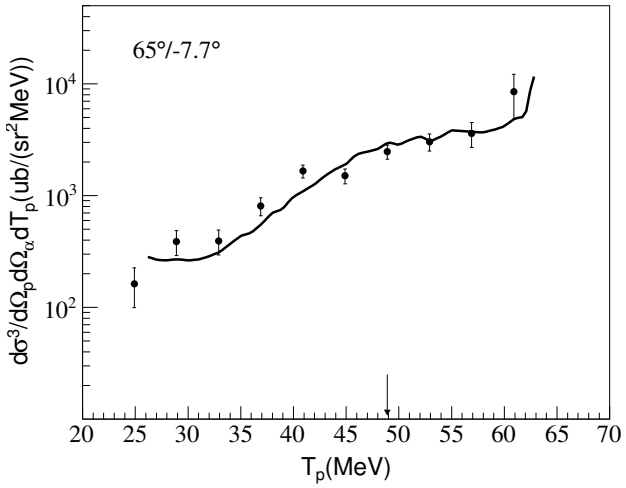

Figure 80 Triple differential cross sections for the ^{10}Be$(p, p\alpha)^6$He(g.s.) reaction at 150 MeV. The arrow indicate T_1 at QFS condition. The solid line represent DWIA calculations.

Figure 80 and Figure 81 show the extracted experimental TDX for transitions to the ground state of the residual nuclei. The arrows in the plots indicate the T_1 corresponding to the recoilless condition. The solid line represent DWIA calculations using THSR. The error bars on each data point represent statistical uncertainties only. The extracted TDXs for the recoilless conditions for both reactions are very close to each other, as shown in Table 21.

Table 21 Angle pairs, two-body centre-of-mass scattering angle, T_1, and TDX at quasifree peaks

channel	θ_p/θ_α (deg)	$\theta_{p-\alpha}$ (deg c.m.)	T_p (MeV)	$d^3\sigma/d\Omega_p d\Omega_\alpha dT_p$ (μb sr^{-2}MeV^{-1})
^{10}Be$(p, p\alpha)^6$He	65/7.7	41.9	48.9	(2479.2 $\pm$ 355.5)
^{12}Be$(p, p\alpha)^8$He	65/7.4	40.7	46.2	(2200.1 $\pm$ 292.5)

For the ^{10}Be$(p, p\alpha)^6$He reaction, we find that both the shape and the magnitude of the TDX are very well reproduced by the DWIA calculation using the THSR wave function in [13]. The TDX has a sudden increase at the maximum T_1 which is

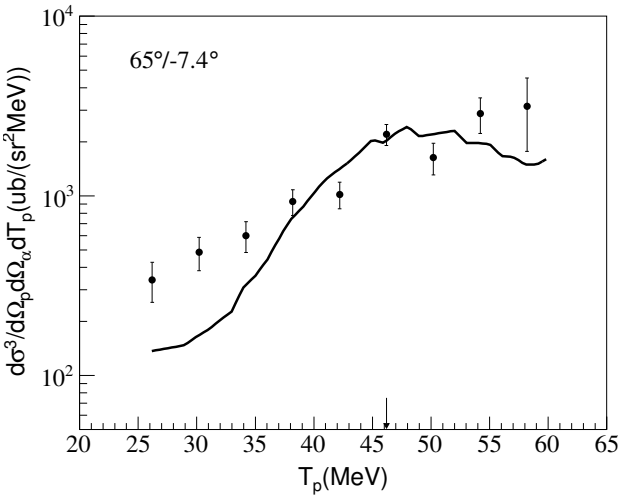

Figure 81 Triple differential cross sections for the ^{12}Be$(p,p\alpha)^8$He(g.s.) reaction at 150 MeV. The arrow indicate T_1 at QFS condition. The solid line represent DWIA calculations.

expected behavior induced by the phase volume [26]. The DWIA calculations are normalized to the experimental results and the normalization factor is 1.09 obtained by fitting. This result directly validates the description of the molecular structure: $2\alpha + 2n(\pi)$ of ^{10}Be described by the THSR cluster wave function.

In Figure 81, the shape of the experimental result is in moderate agreement with the DWIA calculation and the normalization factor is only 0.11, showing great overestimation of the TDX coming from the theoretical prediction. Unlike the ground state of ^{10}Be, which has only one configuration, the ground state of ^{12}Be has three different configurations: α+^{8}He, π-orbit, and σ-orbit. The total cluster wave function is obtained by superposing the basis states in the three configurations. The disagreement between theoretical prediction and experimental result indicates a more compact structure exist in the ground state of ^{12}Be than the theoretical prediction. The origin of the disagreement and the relative weight of three cluster configurations in ^{12}Be need to be further investigated.

4.3 Cross-sections for the ground-state and first 2^+ state transitions

As shown in the Section 4.1, the population of the ground-state residues in the case of ^{10}Be and ^{12}Be beams is comparable, while the population of the 2^+ and other excited states are observed to be considerably different in these two cases.

In this section, we will extract the cross-section for the population of the ground-state and 2^+ excited-state in the residues for angle pairs including the recoilless condition. Due to the slight change in the mass of the residual nucleus, the corresponding angle pairs based on the zero momentum transfer also slightly changes(Table 22). The angle pairs variation between ground-state and 2^+ state is small and it was checked that the experimental acceptance is the same for both cases

Table 22 Angle pairs for different residue states in QFS $(p, p\alpha)$ reaction

Beam	Residue State	$(\theta_p = 62, \theta_\alpha)$	$(\theta_p = 65, \theta_\alpha)$
^{10}Be	^{6}He(0^+), g.s.	(62.0°, 8.7°)	(65.0°, 7.7°)
	^{6}He(2^+), 1.8 MeV	(62.0°, 8.6°)	(65.0°, 7.5°)
^{12}Be	^{8}He(0^+), g.s.	(62.0°, 8.5°)	(65.0°, 7.4°)
	^{8}He(2^+), 3.1 MeV	(62.0°, 8.1°)	(65.0°, 7.0°)

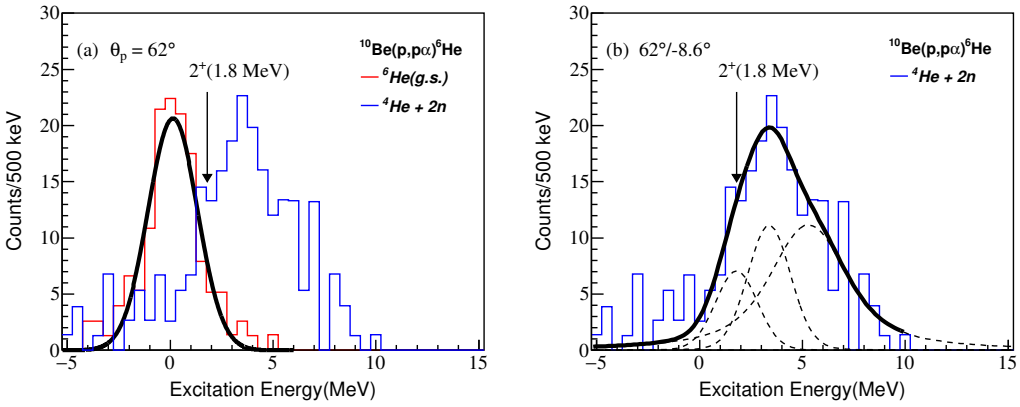

Figure 82 (a) The excitation energy spectra of ^{6}He obtained for the angle bins with θ_p =62 °. (b) Decomposition of the excitation energy spectrum for the excited states

Figure 82 and 83 show the excitation energy spectra of ^{6}He obtained for the angle bins with θ_p =62 °, θ_p =65 °, respectively. The number of counts for the ground states were extracted straightforwardly as only the ground state of the ^{6}He and ^{8}He residues are bound, and then easy to separate from the other channels by gating with Hodoscope PID. The number of counts for the 2^+ excited state have to be obtained by decomposing the components from the measured broad bump, since other excited states also have strong contributions. In Figure 83(right), three resonant states are included: 2^+(1.8 MeV, $\Gamma = 0.113$ MeV) [49], the resonance previously observed at 5.3 MeV [50] and a new resonance needed to reproduce the data(not mentioned in the

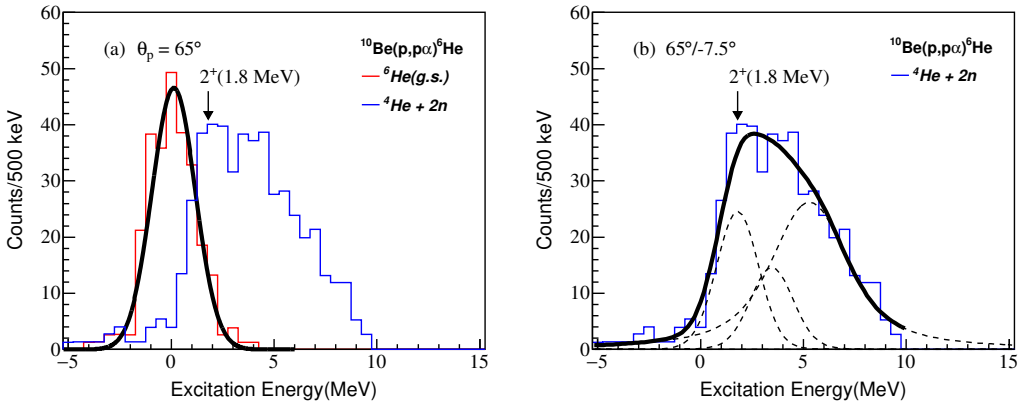

Figure 83 (a) The excitation energy spectra of ^{6}He obtained for the angle bins with θ_p =65 °. (b) Decomposition of the excitation energy spectrum for the excited states

literature). The normalization of three states is set free parameters. The energy and angle of the p-α pairs from first 2^+ state transition are very close to the ground-state transition case, it is reasonable to use the 1.1 MeV resolution in the decomposition. The widths of the 2^+ and the 5.3 MeV state are known from the literature, and the width of the intermediate states is set as free parameter. The counts and cross-sections obtained from the decomposition analysis are listed in Table 23 and 24.

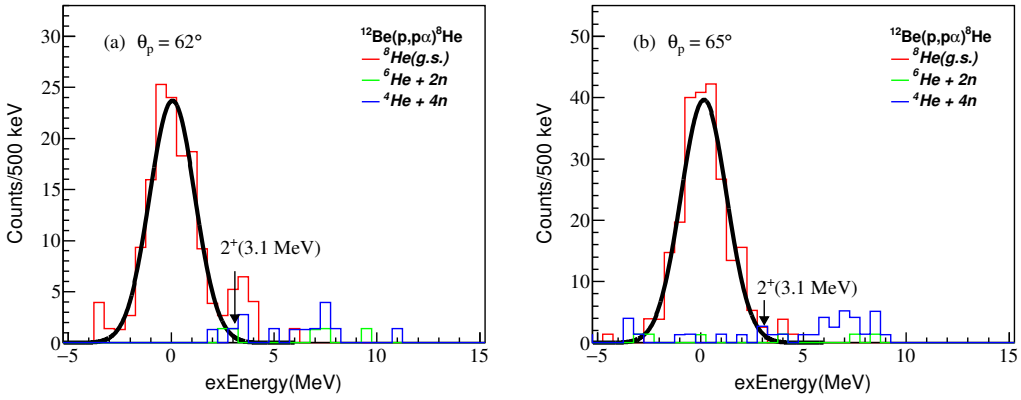

Figure 84 The excitation energy spectra of ^{8}He obtained for the angle bins. (a) θ_p =62 °; (b) θ_p =65 °;

Figure 84 shows the excitation energy spectra of ^{8}He obtained for the angle bins with θ_p =62 °, θ_p =65 °, respectively. Within our statistics and given the background, we extract only an upper limit of the cross-sections. The count of the 2^+ state is set to 1 for extracting cross sections.

Table 23 Cross-sections for the population of the ground state and 2^+ excited state of residues ($\theta_p = 62°$)

Beam	Final state	Counts	cross-section (μb)	2^+/(g.s.) (%)
^{10}Be	^{6}He(g.s.)	149	0.69 ± 0.06	24.8
	^{6}He(2^+)	37	0.17 ± 0.03	
^{12}Be	^{8}He(g.s.)	156	0.61 ± 0.05	0.7
	^{8}He(2^+)	<=1	0.004 ± 0.004	

Table 24 Cross-sections for the population of the ground state and 2^+ excited state of residues ($\theta_p = 65°$)

Beam	Final state	Counts	cross-section (μb)	2^+/(g.s.) (%)
^{10}Be	^{6}He(g.s.)	268	1.25 ± 0.08	47.8
	^{6}He(2^+)	128	0.60 ± 0.05	
^{12}Be	^{8}He(g.s.)	241	0.94 ± 0.06	0.4
	^{8}He(2^+)	<=1	0.004 ± 0.004	

Cross-sections for the angle bins are calculated by

$$\sigma = \frac{N(Ex)}{N_{tgt} N_{beam} \varepsilon_{det}} \tag{83}$$

The ratio between the population of the ground-state and 2^+ excited-state in the residues have been extracted. This ratio is changes from 24.8% to 47.8% for the proton scattering angles from 62 to 65 degrees in ^{10}Be$(p, p\alpha)$ reaction. In strong contrast, the ratio is less than 1% in the ^{12}Be$(p, p\alpha)$ reactions for both angles From Table 23 and 24, one can already conclude that the contribution of 2^+ state component of ^{6}He (^{8}He) core in the ground state of ^{10}Be (^{12}Be) is very different. Further steps need to be taken to draw more definite conclusions. Calculations of DWIA cross-sections for the population of the 2^+ states in the helium residues are foreseen in a near future.

Chapter 5

Conclusion

Cluster structures of neutron-rich Beryllium isotopes have been investigated via $(p, p\alpha)$ reaction in inverse kinematics at RIKEN. The measurement aims at triple differential cross sections (TDX) which provide direct and quantitative information of alpha cluster structure. The reactions of interest were induced by radioactive beams of ^{10,12,14}Be at 150 MeV/u impinging on a 2 mm thick solid hydrogen target. The measurement of incident beam particles and outgoing Helium reaction residues near zero degrees was performed by using the SAMURAI spectrometer and its standard detectors. The ESPRI setup consisting of drift chamber and scintillators was implemented for recoil proton detection at angular range of 50°-70°. For detection of alpha clusters, two telescopes composed of Silicon and CsI(Tl) detectors were placed at angular range of 4°-12°. The angular coverage for p-α pair measurement was chosen to fulfill the kinematics of quasi-free condition in the $(p, p\alpha)$ reaction. Missing mass method was used to reconstruct the kinematics for populations to the unbound states of He residues. Desirable missing mass resolution of σ=1.1 MeV was achieved allowing clear separation of the ground and excited-state transitions.

The TDX for the QFS $(p, p\alpha)$ reactions are extracted at the coplanar angle pairs (θ_p,θ_α) which were chosen to include zero recoil momentum condition of the residual nucleus. The extracted TDXs = 2479.2 $\pm$ 355.5 μb/(MeV sr^2) for the ^{10}Be$(p, p\alpha)^6$He(g.s.), and 2200.1 $\pm$ 292.5 μb/(MeV sr^2) for the ^{12}Be$(p, p\alpha)^8$He(g.s.) at the recoilless conditions($\theta_p = 65°$), respectively. The TDXs of ground-state transition for both reactions are very close to each other. Both the shape and the magnitude of the TDX for ^{10}Be$(p, p\alpha)^6$He(g.s.) reaction are very well reproduced by the DWIA reaction calculation. The normalization factor between the experimental result and the theoretical calculation is 1.09, directly validating the molecular-like cluster structure with two α centering in the ground state of ^{10}Be nucleus described by the THSR structure model.

^{12}Be is considered as four valence neutrons surrounding the α-α core with three different cluster structures of α+^{8}He, π-orbit, and σ-orbit. For ^{12}Be$(p, p\alpha)^8$He(g.s.), preliminary TDX calculation is in moderate agreement with the shape and overestimates the magnitude of the experimental distribution, indicating a more compact

structure in ^{12}Be than the theoretical prediction. The result therefore suggests the relative weighting of these three components in the cluster wave function needs to be further improved.

Cross-sections for the $^{10}\mathrm{Be}(p,p\alpha)^{6}\mathrm{He}(2^{+})$ and $^{12}\mathrm{Be}(p,p\alpha)^{8}\mathrm{He}(2^{+})$ have been extracted and compared to the results in ground-state transition. The cross-section ratio of 2^{+} excited-state transition to ground-state transition for $^{10}\mathrm{Be}(p,p\alpha)$ reaction is nearly a half at proton scattering angle 65°. In strong contrast, the cross-section ratio of 2^{+} excited state transition to ground-state transition for $^{12}\mathrm{Be}(p,p\alpha)$ reaction is less than 1%. Such a large difference in the contribution of He core-excited states in the ground state of ^{10}Be and ^{12}Be indicates that the cluster structure in both cases are significantly distinct. DWIA cross section calculations of the 2^{+} state population in He residues are being performed for more definite conclusions.

The experimental data analysis of $^{14}\mathrm{Be}(p,p\alpha)$ has been completed and the theoretical calculation is in preparation. Together with ^{10}Be ad ^{12}Be, we would achieve the first systematic and quantitative studies of alpha clustering in exotic nuclei close to the nuclear dripline, guiding towards comprehensive and even beyond the traditional understanding of nuclear forces.

Appendix I

Three-body kinematics

Once the detectors are mounted at certain position, the angular coverage is fixed. The polar and azimuthal angle (θ_1, φ_1) and (θ_2, φ_2) can be easily determined by the position measurement for the detection setup of particle 1 and 2. There are usually two kinematic solution allowed by the three-body kinematics[48].

If the T_1 and (θ_1, φ_1) of particle 1 are known in the lab frame, the combined system of particle 2 and B can be uniquely calculated from the conservation of energy and momentum. Let's name the system of particle 2 and B as R2B.

$$E_{2B} = E_{CM} - E_1 \tag{84}$$

$$p_{2B} = \left|\mathbf{p}_{CM} - \mathbf{p}_1\right| = \left(p_{CM}^2 + p_1^2 - 2p_{CM}p_1\cos\theta_1\right)^{1/2} \tag{85}$$

The angle θ_{2B} of the R2B system with respect to the z-axis in the lab frame is expressed as follows:

$$\sin\theta_{2B} = p_1\sin\theta_1/p_{2B} \tag{86}$$

$$\cos\theta_{2B} = \left(p_{CM} - p_1\cos\theta_1\right)/p_{2B} \tag{87}$$

Since the quantities of the R2B system can be determined, then the problem can be simplified to solve p_2 in the two body kinematics. The energy and momentum of particle 2 in the R2B can be expressed in terms of the invariant mass M_{2B}.

$$p_2^{\mathrm{R2B}} = \lambda^{1/2}\left(M_{2B}^2, m_2^2, m_3^2\right)/\left(2M_{2B}\right) \tag{88}$$

$$E_2^{\mathrm{R2B}} = \left(M_{2B}^2 + m_2^2 - m_3^2\right)/\left(2M_{2B}\right) \tag{89}$$

where

$$M_{2B}^2 = \left(E_2 + E_B\right)^2 - \left(\mathbf{p}_2 + \mathbf{p}_B\right)^2 \tag{90}$$

$$= \left(E_{CM} - E_1\right)^2 - \left(\mathbf{p}_{CM} - \mathbf{p}_1\right)^2 \tag{91}$$

$$= M_{CM}^2 + m_1^2 - 2E_{CM}E_1 + 2p_{CM}p_1\cos\theta_1 \tag{92}$$

and the function of $\lambda(x, y, z)$ is defined as $\lambda(x, y, z) = x^2 + y^2 + z^2 - 2xy - 2yz - 2zx$.

The quantities of particle 2 in the lab frame can be calculated from the quantities in the R2B system through Lorentz transformation between these frames. The Lorentz transformation equation for E_2^{R2B} is written as

$$E_2^{\mathrm{R2B}} = -\gamma\beta p_2 \cos\theta_2' + \gamma E_2 \tag{93}$$

$$= -\gamma\beta p_2 \cos\theta_2' + \gamma \left(p_2^2 + m_2^2\right)^{1/2} \tag{94}$$

where $\beta = p_{2B}/E_{2B}$ and $\gamma = p_{2B}/M_{2B}$. The angle θ_2' is measured with respect to the z-axis of the R2B system and $\cos\theta_2'$ is given by

$$\cos\theta_2' = \left(P_0 \cos\theta_2 - P_1 \cos\theta_{1-2}\right)/P_{23} \tag{95}$$

$$\cos\theta_{1-2} = \cos\theta_1 \cos\theta_2 + \sin\theta_1 \sin\theta_2 \cos\left(\varphi_2 - \varphi_1\right) \tag{96}$$

Finally, the solution of p_2 is expressed by

$$p_2 = (-B \pm \sqrt{B^2 - 4AC})/2A \tag{97}$$

with

$$A = \gamma^2\left(1 - \beta^2 \cos^2\theta_2'\right) \tag{98}$$

$$B = -2E_2^{R2B}\gamma\beta\cos\theta_2' \tag{99}$$

$$C = \gamma^2 m_2^2 - \left(E_2^{R2B}\right)^2 \tag{100}$$

Both solutions are allowed physically when the discriminant of the quadratic equations is satisfied. The discriminant can be simplified into

$$\beta^2\gamma^2 \sin^2\theta_2^{R2B} = \left(\gamma_2^{R_{2B}}\right)^2 - 1 \tag{101}$$

where $\gamma_2^{R2B} = E_2^{R2B}/M_2^{R2B}$.

Appendix II

QFS Condition

Table 25 QFS condition in ^{10}Be$(p, p\alpha)^{6}$He(g.s.) reaction at 150.091 MeV/u

θ_p/θ_α (deg)	T_p (MeV)	$\theta_{p-\alpha}$ (deg c.m.)	θ'_p/θ'_α (deg b.s.)	T'_p (MeV b.s.)
60.0/-9.3	74.1	52.1	41.2/-61.7	125.1
61.0/-9.0	68.8	50.1	39.5/-62.7	126.4
62.0/-8.7	63.6	48.0	37.8/-63.6	127.7
63.0/-8.4	58.6	46.0	36.1/-64.5	129.0
64.0/-8.0	53.7	43.9	34.5/-65.4	130.2
65.0/-7.7	48.9	41.8	32.8/-66.4	131.4
66.0/-7.3	44.3	39.7	31.1/-67.3	132.6
67.0/-6.9	39.8	37.5	29.4/-68.2	133.7
68.0/-6.6	35.5	35.4	27.6/-69.1	134.8
69.0/-6.2	31.3	33.2	25.9/-70.0	135.9
70.0/-5.8	27.3	30.9	24.1/-70.8	136.9

Table 26 QFS condition in ^{12}Be$(p, p\alpha)^{8}$He(g.s.) reaction at 149.775 MeV/u

θ_p/θ_α (deg)	T_p (MeV)	$\theta_{p-\alpha}$ (deg c.m.)	θ'_p/θ'_α (deg b.s.)	T'_p (MeV b.s.)
60.0/-9.2	71.5	51.4	40.5/-61.6	123.9
61.0/-8.8	66.1	49.3	38.8/-62.6	125.2
62.0/-8.5	60.9	47.2	37.1/-63.5	126.5
63.0/-8.2	55.9	45.0	35.3/-64.4	127.8
64.0/-7.8	51.0	42.9	33.6/-65.3	129.0
65.0/-7.4	46.2	40.7	31.9/-66.2	130.2
66.0/-7.1	41.5	38.6	30.1/-67.1	131.4
67.0/-6.7	37.1	36.3	28.4/-68.0	132.5
68.0/-6.3	32.7	34.0	26.5/-68.9	133.6
69.0/-5.9	28.5	31.7	24.7/-69.8	134.7
70.0/-5.5	24.3	29.2	22.8/-70.6	135.8

Table 27 QFS condition in ^{14}Be$(p, p\alpha)^{10}$He(g.s.) reaction at 150.021 MeV/u

θ_p/θ_α (deg)	T_p (MeV)	$\theta_{p-\alpha}$ (deg c.m.)	θ'_p/θ'_α (deg b.s.)	T'_p (MeV b.s.)
60.0/-8.8	67.1	49.9	39.2/-61.5	122.5
61.0/-8.5	61.7	47.7	37.4/-62.4	123.8
62.0/-8.1	56.5	45.5	35.6/-63.3	125.2
63.0/-7.8	51.3	43.3	33.8/-64.2	126.5
64.0/-7.4	46.4	41.0	32.0/-65.1	127.7
65.0/-7.0	41.5	38.7	30.2/-66.0	128.9
66.0/-6.6	36.7	36.3	28.3/-66.9	130.1
67.0/-6.2	32.1	33.9	26.3/-67.7	131.3
68.0/-5.8	27.5	31.3	24.3/-68.6	132.5
69.0/-5.3	23.0	28.5	22.1/-69.4	133.6
70.0/-4.7	18.3	25.4	19.7/-70.2	134.8

Appendix III

Neutron and cluster decay threshold

Table 28 Neutron removal threshold

Mother nuclei	1n	2n	3n	4n	5n	6n
^{14}Be	1.78	1.27	4.44	4.94	11.75	13.42
^{12}Be	3.17	3.67	10.48	12.15		
^{10}Be	6.81	8.48				
^{8}He	2.53	2.13		3.10		
^{6}He	1.71	0.975				

Table 29 Helium cluster breakup threshold

Mother nuclei	breakup channel	Threshold (MeV)
^{10}Be	^{4}He + ^{6}He	7.41
^{12}Be	^{4}He + ^{8}He	8.96
^{12}Be	^{6}He + ^{6}He	10.11
^{14}Be	^{4}He + ^{10}He(^{8}He+2n)	11.67

References

[1] T. A. Carey et al. “Alpha-particle spectroscopic strengths using the $(p, p\alpha)$ reaction at 101.5 MeV”. *Phys. Rev. C* (1984), 16.

[2] W. von Oertzen, M. Freer, and Y. Kanada-En’yo. “Nuclear clusters and nuclear molecules”. *Physics Reports* **432** (2006), 43–113.

[3] L. R. Hafstad and E. Teller. “The Alpha-Particle Model of the Nucleus”. *Phys. Rev.* **54** (1938), 681–692.

[4] Martin Freer. “The clustered nucleus—cluster structures in stable and unstable nuclei”. *Reports on Progress in Physics* **70** (2007), 2149–2210.

[5] Y. Kanada-En’yo and H. Horiuchi. “Structure of Light Unstable Nuclei Studied with Antisymmetrized Molecular Dynamics”. *Prog. Theor. Phys.* **142** (2001), 205–263.

[6] Hisashi Horiuchi, Kiyomi Ikeda, and Kiyoshi Katō. “Recent Developments in Nuclear Cluster Physics”. *Prog. Theor. Phys.* **192** (2012), 1–238.

[7] Hisashi Horiuchi, Kiyomi Ikeda, and Kiyoshi Katō. “Recent Developments in Nuclear Cluster Physics”. *Prog. Theor. Phys.* **192** (2012), 1–238.

[8] Kiyomi Ikeda, Noboru Takigawa, and Hisashi Horiuchi. “The Systematic Structure-Change into the Molecule-like Structures in the Self-Conjugate 4n Nuclei”. *Prog. Theor. Phys.* **E68** (1968), 464–475.

[9] R. B. Wiringa et al. “Quantum Monte Carlo calculations of $A = 8$ nuclei”. *Phys. Rev. C* **62** (2000), 014001.

[10] S. D. Pain et al. “Structure of ^{12}Be: Intruder d-Wave Strength at $N = 8$”. *Phys. Rev. Lett.* **96** (2006), 032502.

[11] M. Ito et al. “Coexistence of Covalent Superdeformation and Molecular Resonances in an Unbound Region of ^{12}Be”. *Phys. Rev. Lett.* **100** (2008), 182502.

[12] M. Ito, N. Itagaki, and K. Ikeda. “Cluster correlations for low-lying intruder states of ^{12}Be”. *Phys. Rev. C* **85** (2012), 014302.

[13] Mengjiao Lyu et al. “Manifestation of α clustering in ^{10}Be via α-knockout reaction”. *Phys. Rev. C* **97** (2018), 044612.

[14] N. I. Ashwood et al. “Helium clustering in neutron-rich Be isotopes”. *Phys. Lett. B* **580** (2004), 129–136.

[15] N. I. Ashwood et al. “Neutron removal and cluster breakup of ^{14}B and ^{14}Be”. *Phys. Rev. C* **70** (2004), 024608.

[16] Kazuki Yoshida, Kosho Minomo, and Kazuyuki Ogata. “Investigating alpha clustering on the surface of ^{120}Sn via the $(p, p\alpha)$ reaction, and the validity of the factorization approximation”. *Phys. Rev. C* **94** (2016), 044604.

[17] N. S. Chant and P. G. Roos. “Distorted-wave impulse-approximation calculations for quasifree cluster knockout reactions”. *Phys. Rev. C* **15** (1977), 57–68.

[18] Mengjiao Lyu et al. “Direct probing of the cluster structure in ^{12}Be via the α-knockout reaction”. *Phys. Rev. C* **99** (2019), 064610.

[19] Kazuki Yoshida, Kazuyuki Ogata, and Yoshiko Kanada-En’yo. “Investigation of α clustering with knockout reactions”. *Phys. Rev. C* **98** (2018), 024614.

[20] A. Tohsaki et al. “Alpha Cluster Condensation in ^{12}C and ^{16}O”. *Phys. Rev. Lett.* **87** (2001), 192501.

[21] P. G. Roos et al. “Absolute spectroscopic factors from the $(p, p\alpha)$ reaction at 100 MeV on 1p-shell nuclei” (1977), 15.

[22] C. W. Wang et al. “^{9}Be$(p, p\alpha)^{5}$He cluster knockout reaction with 150 MeV polarized protons”. *Phys. Rev. C* (1985), 11.

[23] A. Nadasen et al. “$(p, p\alpha)$ cluster-knockout reaction on ^{9}Be at 200 MeV”. *Phys. Rev. C* **40** (1989), 1130–1135.

[24] L. V. Chulkov et al. “Quasi-free scattering with ^{6,8}He beams”. *Nucl. Phys. A* **759** (2005), 43–63.

[25] Z. X. Cao et al. “Recoil proton tagged knockout reaction for ^{8}He”. *Phys. Lett. B* **707** (2012), 46–51.

[26] K. Ogata. *Private communication*.

[27] Yasushige Yano. “The RIKEN RI Beam Factory Project: A status report”. *Nucl. Instr. and Meth. B* **261** (2007), 1009–1013.

[28] Toshiyuki Kubo. “In-flight RI beam separator BigRIPS at RIKEN and elsewhere in Japan”. *Nucl. Instr. and Meth. B* **204** (2003), 97–113.

[29] T. Kobayashi et al. “SAMURAI spectrometer for RI beam experiments”. *Nucl. Instr. and Meth. B* **317** (2013), 294–304.

[30] Y. Matsuda et al. “Large, thin solid hydrogen target using para-H2”. *Nucl. Instr. and Meth. A* **643** (2011), 6–10.

[31] A. Obertelli and T. Uesaka. “Hydrogen targets for exotic-nuclei studies developed over the past 10 years”. *Eur. Phys. J. A* **47** (2011), 105.

[32] Y. Matsuda et al. “Elastic scattering of protons from ^{9}C with a 290 MeV/nucleon ^{9}C beam”. *Phys. Rev. C* **87** (2013), 034614.

[33] *Micron Semiconductor Ltd*. URL: `http://www.micronsemiconductor.co.uk`.

[34] G. Verde et al. “The Farcos project: Femtoscope Array for Correlations and Femtoscopy”. *J. Phys. Conf. Ser.* **420** (2013), 012158.

[35] A. Pagano et al. “Fragmentation studies with the CHIMERA detector at LNS in Catania: recent progress”. *Nucl. Phys. A* **734** (2004), 504–511.

[36] H. Baba et al. “New data acquisition system for the RIKEN Radioactive Isotope Beam Factory”. *Nucl. Instr. and Meth. A* **616** (2010), 65–68.

[37] O. B. Tarasov and D. Bazin. “LISE++: Radioactive beam production with in-flight separators”. *Nucl. Instr. and Meth. B* **266** (2008), 4657–4664.

[38] Hwang Jongwon. “Study of ^{19}C by One-Neutron Knockout Reaction with a Carbon Target”. *Ph.D. Thesis* (2015), p43.

[39] William R. Leo. *Techniques for Nuclear and Particle Physics Experiments: A How-to Approach*. 2nd ed. Berlin Heidelberg: Springer-Verlag, 1994. ISBN: 978-3-540-57280-0.

[40] T. Sugimoto et al. “The first 2^{+} state of ^{14}Be”. *Phys. Lett. B* **654** (2007), 160–164.

[41] R. Qiao et al. “A New Uniform Calibration Method for Double-Sided Silicon Strip Detectors”. *IEEE Trans. Nucl. Sci.* **61** (2014), 596–601.

[42] M. J van Goethem et al. “Investigations and corrections of the light output uniformity of CsI(Tl) crystals”. *Nucl. Instr. and Meth. A* **526** (2004), 455–476.

[43] A. Matta et al. “NPTool: a simulation and analysis framework for low-energy nuclear physics experiments”. *J. Phys. G* **43** (2016), 045113.

[44] S. Agostinelli et al. “Geant4—a simulation toolkit”. *Nucl. Instr. and Meth. A* **506** (2003), 250–303.

[45] R. K. Tripathi, F. A. Cucinotta, and J. W. Wilson. “Accurate universal parameterization of absorption cross sections III – light systems”. *Nucl. Instr. and Meth. B* **155** (1999), 349–356.

[46] Wen-qing Shen et al. “Total reaction cross section for heavy-ion collisions and its relation to the neutron excess degree of freedom”. *Nucl. Phys. A* **491** (1989), 130–146.

[47] L. Sihver et al. “A comparison of total reaction cross section models used in FLUKA, GEANT4 and PHITS”. *2012 IEEE Aerospace Conference*. 2012, 1–10.

[48] Shigeru Kakigi et al. “Three-Particle Relativistic Kinematics”. *Bulletin of the Institute for Chemical Research, Kyoto University* **57(1)** (1979), 83–91.

[49] D. R. Tilley et al. “Energy levels of light nuclei A=5, 6, 7”. *Nucl. Phys. A* **708** (2002), 3–163.

[50] X. Mougeot et al. “New excited states in the halo nucleus ^{6}He”. *Phys. Lett. B* **718** (2012), 441–446.

[51] *National Nuclear Data Center*. URL: `https://www.nndc.bnl.gov`.

[52] A. A. Korsheninnikov et al. “Experimental studies of light neutron rich nuclei”. *Nucl. Phys. A* **588** (1995), c23–c28.

[53] D. V. Aleksandrov et al. “Search for Excited States of Neutron-Excess Nuclei ^{8}He and ^{7}He”. *Izvestiya Akademii Nauk* **49** (1985), 2115.

[54] A. V. Belozerov et al. “Heavy-Ion Reaction Helium-Isotope Features”. *Izvestiya Akademii Nauk* **52** (1988), 100.

[55] W. von Oertzen et al. “Nuclear structure studies of very neutron-rich isotopes of $^{7}\lambda^{10}$He, $^{9}\lambda^{11}$Li and $^{12}\lambda^{14}$Be via two-body reactions”. *Nucl. Phys. A* **588** (1995), c129–c134.

[56] K. Markenroth et al. “^{8}Heλ^{6}He: a comparative study of nuclear fragmentation reactions”. *Nucl. Phys. A* **679** (2001), 462–480.

[57] A. Matta et al. “New findings on structure and production of ^{10}He from ^{11}Li with the (d,^{3}He) reaction”. *Phys. Rev. C* **92** (2015), 041302.

[58] *Voigt profile from Wikipedia*. URL: `http://en.wikipedia.org/wiki/Voigt_profile`.

[59] H. T. Johansson et al. “The unbound isotopes ^{9,10}He”. *Nucl. Phys. A* **842** (2010), 15–32.

[60] Z. Kohley et al. “Unresolved Question of the ^{10}He Ground State Resonance”. *Phys. Rev. Lett.* **109** (2012), 232501.